

Jet Blast Energy Harvester

A Major Qualifying Project
Submitted to the faculty of
WORCESTER POLYTECHNIC INSTITUTE
in partial fulfillment for the
Bachelor of Science Degree
in Mechanical Engineering

By:

Constantine “Tino” Christelis, ME

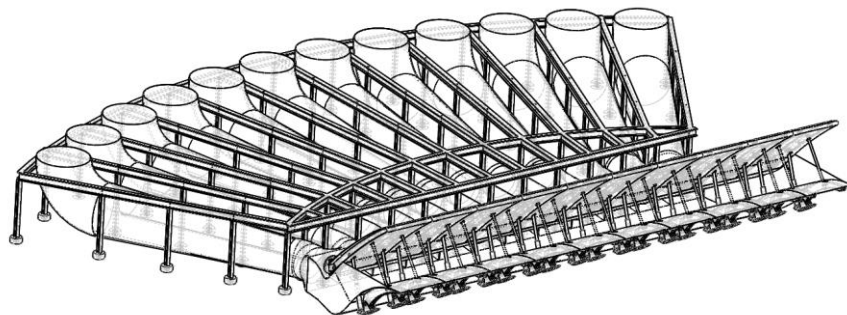
William “Will” Dziuban, ME

Jessica “Jess” Norman, ME

Advised By:

Professor Fiona Levey, ME

Date of Submission:
April 25, 2018



Abstract

The transportation sector is one of the largest energy consumers in the US. Reducing airport energy consumption would benefit the environment. This MQP designed a system to effectively and efficiently harvest energy from jet blast at commercial airports. The system consists of a hydraulically actuated flap to redirect airflow, a funneled duct that leads to a turbine bank, and a diffuser to allow air to exit the system. Positioned at the end of a runway, it is designed to be stowed under the runway surface in order to have minimal impact on regular air traffic operations. Both the mechanical system and the flow were modeled, and testing was performed on prototypes for comparison with some aspects of the modeled behavior. According to our models, if jet blast was captured from all of Logan Airport's flights, our system could produce enough energy to power the equivalent of 720 homes year-round.

Acknowledgments

We would like to extend our sincerest gratitude to the following individuals for their assistance in helping us accomplish our project:

- Professor Fiona Levey for her constant support and assistance throughout our project. We would not have been able to succeed without you.
- Barbara Fuhrman for her assistance with the purchase and acquisition of everything needed for the project.
- Adriana Hera, Ermal Toto and the ARC for their guidance with ANSYS and simulation software.
- Professor David Olinger for his assistance in aerodynamics and allowing us to use the wind and water tunnels for testing.
- Professor Robert Daniello for his assistance in fluids analysis.
- Peter Hefti for providing resources and guidance within the MQP lab space.
- Jacqui Goodwin and Spencer Austin for their assistance in 3D printing.
- Professor John Orr, Professor Paul Mathisen and the Green Forum for being our sounding board throughout the academic year and providing feedback on our design.
- Natalie Fox for her help with modifying a print job during the project.

Table of Contents

Harnessing Energy From Jet Blast.....	0
Abstract	1
Acknowledgments.....	2
Table of Contents.....	3
Table of Tables.....	4
Table of Figures.....	4
1.0 - Introduction.....	7
2.0 - Background.....	7
2.1 - Energy Needs.....	7
2.1.1 - Climate change	7
2.1.2 - United States current energy demand.....	7
2.1.3 - Airport energy demand	8
2.2 - Jet Blast Potential.....	9
2.2.1 - Jet Blast Velocity	9
2.2.3 - Dangers of Jet Blast.....	11
2.3 - Current Technology	12
2.3.1 - Wind Energy	12
2.3.2 - Noteworthy Patents	15
2.4 - Runway Layout.....	16
3.0 - Project Definition.....	16
4.0 - Design.....	17
4.1 - Overall System Design	17
4.2 - Design Considerations.....	22
4.3 - Duct Entrance Region	23
4.4- Primary and Secondary Flaps.....	28
4.5 - Closing Mechanism	33
4.6 - Duct Exit Region.....	35
5.0 - Analysis.....	37
5.1 - Power Estimates	37
5.2 - Fluids Analysis	40
5.3 - Aerodynamic Analysis	47
5.4 - Structural Analysis.....	51
5.4.1 - Mechanism Analysis.....	51

5.4.2 - Support Structure Analysis	60
6.0 - Prototyping and Testing	61
6.1 - Mechanism Prototype	61
6.2 - Wind Tunnel Testing	65
6.3 - Water Tunnel Testing	68
7.0 - Conclusion & Recommendations	73
References	77
Appendix A	79

Table of Tables

Table 1: Flap iteration definitions	30
Table 2: Material properties	31
Table 3: Mechanism design table	33

Table of Figures

Figure 1: Electrical generation of various renewable energy sources [7]	8
Figure 2: Simulated jet blast velocity profile for a Boeing 747-400 [12]	10
Figure 3: Simulated jet blast temperature profile for a Boeing 747-400 [12]	11
Figure 4: Aircraft Carrier [15]	11
Figure 5: Typhoon Turbine [22]	14
Figure 6: Experimental data for a 2.5 meter diameter wind turbine with and without ducting [24]	15
Figure 7: Patent illustration of the “Jetair Recovery Generator” [26]	15
Figure 8: Runway layout with notes [27, 28, 29]	16
Figure 9: System interfaces	17
Figure 10: Jet Blast Deflector turbine concept	18
Figure 11: Underground flap concept	18
Figure 12: Venturi effect	19
Figure 13: Mechanism location assessment	19
Figure 14: Overall system diagram	20
Figure 15: Shutter mechanism, showing closed position (a), opening movement (b), and open (c)	21
Figure 16: Support structure beam locations	21
Figure 17: Support structure layout (top) and model (bottom)	22
Figure 18: Dependence of turbine characteristics as functions of power	24
Figure 19: Duct entrance cross sections	25
Figure 20: Duct entrance constraining dimensions	26
Figure 21: Constraint relation to model	27
Figure 22: Splitting duct entrance flow to individual turbines	28
Figure 23: CFD steady state scenario inputs	28
Figure 24: Flap geometry for Table 1	29
Figure 25: Flap characteristic key for Table 1	29
Figure 26: ANSYS simulation results for Flap 5 Steady State Velocity	31
Figure 27: Flap section with labels	32

Figure 28: Cross-section of primary flap rib pair	32
Figure 29: Mechanism deployed and stowed positions	35
Figure 30: Graph of stall transition based on length and area ratio [31].....	36
Figure 31: Conical Diffuser Outline	37
Figure 32: Graph of jet blast velocity relative to the aircraft.....	38
Figure 33: Graph of aircraft and jet blast velocities over time	38
Figure 34: Estimated power and energy generation.....	39
Figure 35: Jet blast velocity derivation [12]	40
Figure 36: Jet blast velocity parabolic contours	41
Figure 37: ANSYS Fluent transient velocity model	42
Figure 38: ANSYS Fluent transient pressure model.....	42
Figure 39: ANSYS velocity profile at flap intake (time = 2s)	43
Figure 40: Velocity efficiency based on Venturi effect	43
Figure 41: Effective height over time	44
Figure 42: Speed at inlet versus capture efficiency	45
Figure 43: Transient diffuser set up.....	45
Figure 44: ANSYS Fluent transient model, full system	46
Figure 45: ANSYS Fluent diffuser inlet.....	46
Figure 46: ANSYS Fluent diffuser outlet	47
Figure 47: Flat plate assumption flow redirection	48
Figure 48: Aerodynamic modeling with the flat plate assumption	48
Figure 49: ANSYS Fluent pressure contours around flap	49
Figure 50: Lift and drag coefficient for 1/74 scale wind tunnel ANSYS simulation.....	50
Figure 51: Lift and drag coefficient curves for full-scale flap ANSYS simulation	50
Figure 52: Mechanism 4-bar approximation and geometry	52
Figure 53: Free Body Diagrams of the primary flap (left) and secondary flap (right).....	53
Figure 54: Values of unknown forces as function of hydraulic cylinder angle	55
Figure 55: Shear force, normal force, moment, and deflection across length of the primary flap (no jet blast)	56
Figure 56: Cross section of rib and relevant stress cubes	57
Figure 57: Magnitude of the largest stress at any given length across the rib	57
Figure 58: SolidWorks FEA setup.....	58
Figure 59: SolidWorks FEA Stress Analysis - Case 2.....	59
Figure 60: SolidWorks reaction forces for Case 2 (left) and Case 1 (right) and comparison to Mathcad solutions	60
Figure 61: SolidWorks FEA of support structure deformation.....	61
Figure 62: Mechanical prototype CAD	62
Figure 63: Pneumatic plumbing diagram.....	62
Figure 64: Mechanical prototype annotated view.....	63
Figure 65: Mechanical prototype open state	64
Figure 66: Mechanical prototype closed state	64
Figure 67: Flap Prototype model	65
Figure 68: Flap in wind tunnel.....	66
Figure 69: Lift coefficient vs. Angle of Attack for ANSYS and wind tunnel testing.....	66
Figure 70: Drag coefficients vs. angle of attack for ANSYS and wind tunnel testing	67
Figure 71: Cross section of full system	68
Figure 72: Side Geometry Prototype design.....	68
Figure 73: Full Geometry Prototype model.....	69
Figure 74: SGP lower velocity	70
Figure 75: Comparison to Fluent model	70
Figure 76: SGP higher velocity	70

Figure 77: FGP vortex by weight	71
Figure 78: FGP, flow from diffuser	71
Figure 79: Flap in water tunnel.....	72
Figure 80: Flap, back dye release	72
Figure 81: Overall system dimensions.....	73
Figure 82: Research on ducting and diffuser design for turbine optimization [20]	74
Figure 83: Finished mechanical prototype and MQP team (left to right: Tino, Will, and Jess)	76

1.0 - Introduction

Greenhouse gas emissions are forecast to increase, affecting weather patterns and leading to the endangerment of the world population [1]. Unless the United States and the rest of the world make large commitments to innovation in renewable energy production and energy consumption, climate change will be irreversible. By addressing consumption in current high carbon emitting sources, the transition from high-carbon emission technology to low-carbon emission could be pursued more smoothly.

As airports are a location of elevated energy usage and carbon emissions, the team decided to design, prototype, test, and assess the feasibility of a system to generate usable clean energy for the airport to use to offset its carbon footprint without impacting air traffic. This device directs air flow from the exhaust of commercial aircraft taking off to an underground duct system with a turbine and generator. The project focuses on the intake design leading up to the turbines, the mechanisms involved, the analysis of flow through and around the system, power generation estimates, and diffuser design.

2.0 - Background

2.1 - Energy Needs

2.1.1 - Climate change

Climate change is defined as the negative and potentially disastrous effects on global temperatures caused by human-generated carbon emissions. By switching to more renewable sources of energy, concerns over scarcity and global climate modifications would decrease [2]. Climate change effects include rising temperatures such that ice caps would melt, and sea levels would rise, drastically affecting coastal and island communities. It has been estimated that if societies do not halt a 2°C increase in temperature by 2050, the planet will reach the point of no return where damage to the ecosystem would be irreversible. This drastic climate change would affect crop production and agriculture severely as well as threaten human life through an increase in droughts, floods, and storms [2].

2.1.2 - United States current energy demand

The United States is one of the largest energy consumers in the world. In 2016, the US consumed approximately 97 quadrillion BTUs of energy.³ Approximately 81% of that energy came from non-renewable energy sources such as natural gas, petroleum, and coal [3]. Natural gas accounts for nearly 30% of US energy consumption and has been hailed as a “bridge fuel” to a “more renewable future” [4]. Hydraulic fracturing, or more commonly known as “fracking”, is the main method for retrieving natural gas and petroleum. During this process methane leaks into

the atmosphere. Methane is significantly more potent than carbon dioxide as a greenhouse gas. Research suggests that fracking will have a greater carbon footprint than coal [5].

With the increasing pressure to reduce the carbon footprint and the subsequent effects of climate change, there has been a move towards using non-fossil fuel energy sources. Though the United States government has chosen not to follow the 2017 Paris Accords as a nation, many states and individual cities have pledged to follow the goals of the accords [6]. The most common sources of renewable energy are hydro, wind, and solar power. These sources combined accounted for 4.7% of energy production in 2014 and 5.3% in 2016 [3]. While this is not a large amount of growth, it does indicate a positive trend toward renewable sources. Figure 1 details the significant growth for wind power as a source for US electricity generation [7]. This increase is largely due to government incentives for renewable energy as well as better understanding of siting and building wind farms [8].

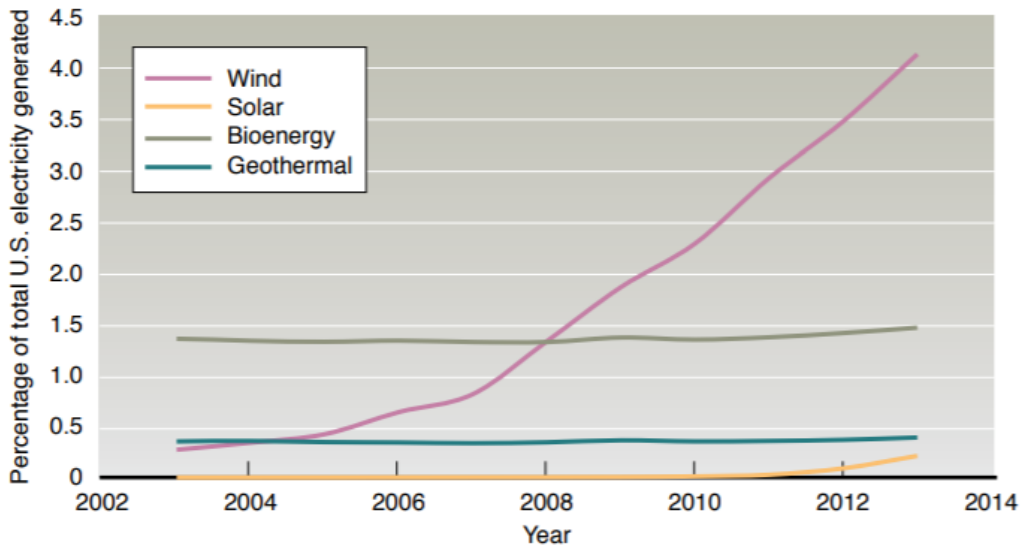


Figure 1: Electrical generation of various renewable energy sources [7]

2.1.3 - Airport energy demand

Airports use a significant amount of energy. For example, Logan Airport in Boston, Massachusetts used nearly 1.6 trillion BTUs in 2016 [9]. This is equivalent to the yearly energy consumption of 65,240 Massachusetts households [10]. While the energy use per passenger in the airport has decreased since 2004, with the continuous increase in passengers since that time, the overall energy has increased by approximately 500 billion BTUs [9]. Airports like Logan as well as many airports in Europe are focused on utilizing renewable energy resources to offset their carbon footprints. A study of energy consumption in European airports investigated various possibilities to include renewable energy into current infrastructure. It found that while solar and wind energy could be useful in those areas, there were several issues that would arise with their implementation. With solar panels, large and costly energy storage would need to be utilized as most of the electricity use is during the night. Traditional turbines would be limited on their proximity to the airport as not to interfere with air traffic and communications [11].

Logan Airport has increased its renewable energy use dramatically with wind and solar power. In 2015, Logan's renewable electricity sources produced 3.16×10^9 BTU (924,874 kW-hr) over the year, approximately 0.2% of its energy use for that year [9]. While other initiatives have focused on implementing typical renewable energy plans, a non-traditional energy harnessing device could provide additional energy to offset carbon emissions of a rapidly growing part of the transportation industry.

2.2 - Jet Blast Potential

2.2.1 - Jet Blast Velocity

To reach the speeds required for takeoff, jet aircraft need to produce a significant amount of thrust. This is achieved by expelling high-speed air from the air breathing jet engines mounted on the wings of aircraft. These engines vary widely among different aircraft, and therefore so do the magnitudes of thrust and wind speed produced. For research purposes, the simulated exhaust velocity profile of a Boeing 747-400 was examined. This line of aircraft was chosen for the large amount of simulated data published by Boeing.

Exhaust from the engines of a 747-400 can reach 250 mph during the takeoff procedure; however, speeds like this are only present up to 10 feet from the end of the aircraft. Speeds of 150 mph extend up to 150 feet away from the plane, and 100 mph up to 470 feet away (see Figure 2 below). The furthest simulated winds were 1,560 feet away, at 35 mph [12]. The simulation treats the plane as stationary to simplify the model [13].

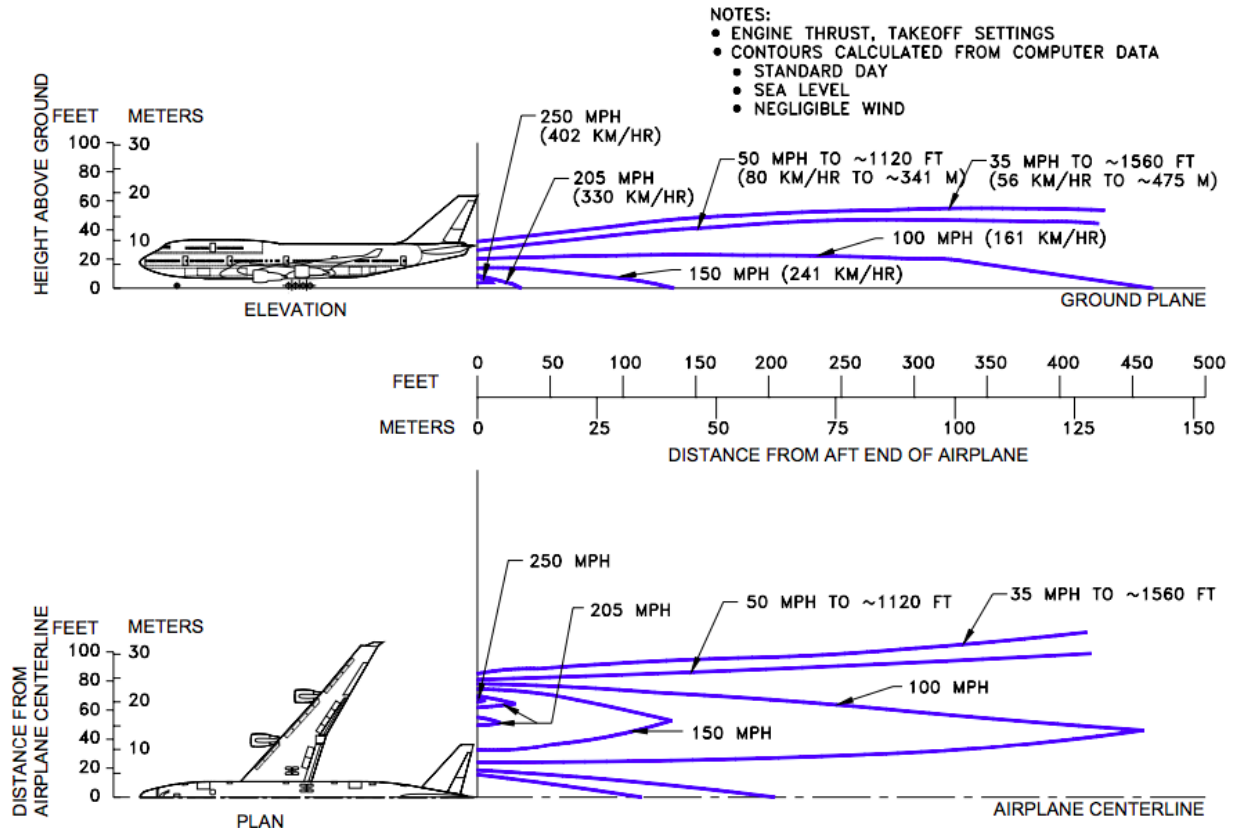
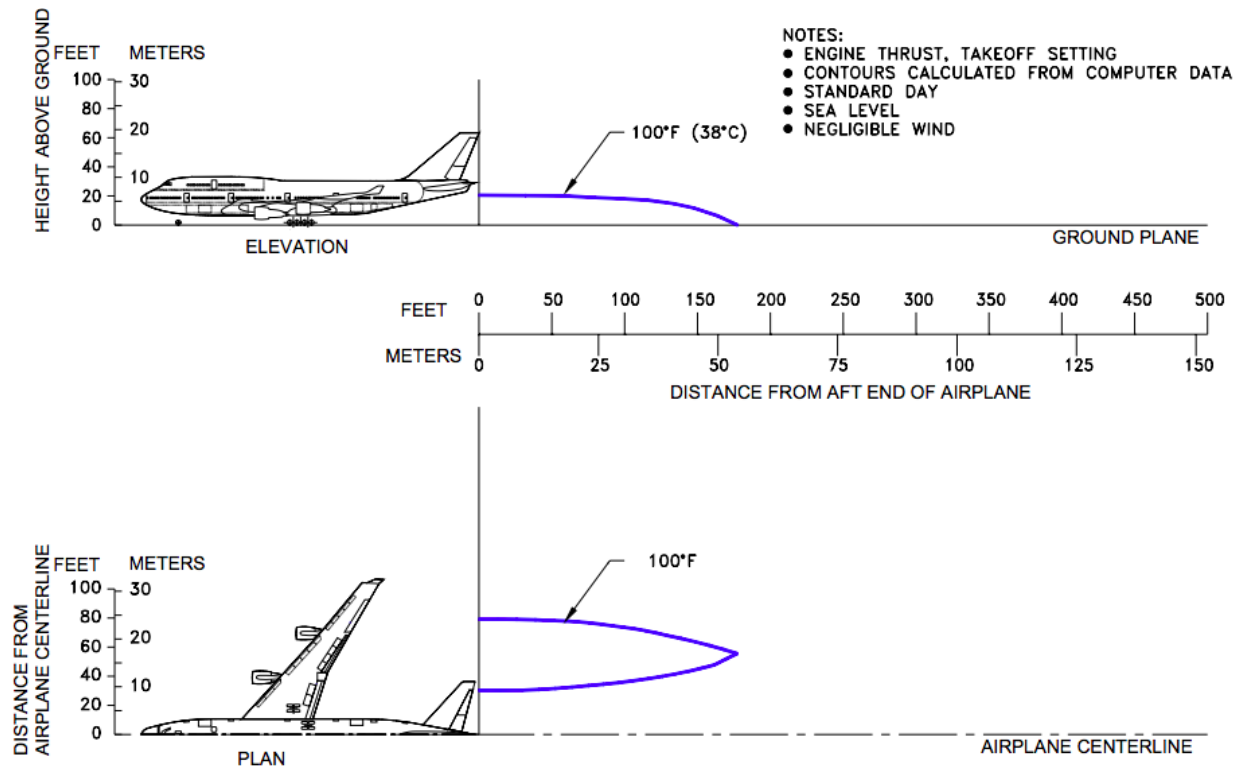


Figure 2: Simulated jet blast velocity profile for a Boeing 747-400 [12]

2.2.2 - Jet Blast Temperature

When a jet turbine puts energy into the air, that energy is transferred as both kinetic and thermal energy. Heat dissipates much faster than kinetic energy. In the jet exhaust of a Boeing 747-400, temperatures of 100°F were simulated up to 175 feet away on a day when the ambient air temperature was 59°F (see Figure 3 below) [12]. While this will change somewhat based on ambient air temperature, the temperature of the jet blast itself does not pose a significant threat of damage to any area around the plane except the areas immediately behind the aircraft.



2.2.3 - Dangers of Jet Blast

With winds at such high speeds, many precautions must be taken at airports where jet aircraft are in service. One of the most common technologies used to mitigate potential damage is the jet blast deflector. This is a flat or curved ramp designed to redirect jet blast upward and away from vulnerable structures or personnel. They are used in both civilian and military applications. Certain commercial airports will place jet blast deflectors at the ends of their runways if there is any danger of damage occurring. In addition, military aircraft carriers have jet blast deflectors located behind their launch assist systems [14].



Figure 4: Aircraft Carrier [15]

Despite the safety measures usually in place, there are many documented incidents where jet blast damages airport structures or even other aircraft. The most common form of jet blast damage is to pavement. Old or damaged pavement is susceptible to being broken apart by strong

jet blast, at which point pieces of asphalt up to 300 feet long are thrown into the air. Less common, but just as dangerous, is when ground vehicles or other smaller aircraft are behind the jet in question. In one incident, a small helicopter was blown into another jet aircraft, with both sustaining heavy damage [16]. By far one of the most troubling incidents occurred in July 2017, when a tourist at Maho Beach on the island of St. Maarten was blown backwards by the jet blast of an aircraft during takeoff. She hit her head on a concrete surface and died hours later at a nearby hospital [17]. Maho Beach is only yards away from Princess Juliana International Airport, and many tourists travel to this beach to experience jet blast. The FAA has many regulations in place to ensure that jet blast does not interfere with property beyond an airport; this example indicates that not all countries have such rules and underlines the importance of said regulations for public safety.

2.3 - Current Technology

2.3.1 - Wind Energy

Traditional wind turbines convert kinetic energy from wind to electrical energy that can be fed into a power grid or stored for later usage. There are many designs that accomplish this, with the most widely used being the three-bladed horizontal axis wind turbine design (commonly known as HAWT). Three blades are spun in a disc perpendicular to the general direction of wind. The three blades attach to a central hub and low speed shaft which carry the load and transmit the rotation to a gearbox. The gearbox takes the slow rotation from the shaft and increases the rotation rate to speeds more suitable for generating power at the generator. Systems that produce power in the megawatt range are often on tall towers where they can take advantage of the higher winds and greater space for increased blade radius. The higher the wind speeds and the greater the turbine blade swept area, the more power the system can produce. Most wind turbines are optimized to generate power with wind speeds of ~35 mph and “cut-out” when wind speeds climb above 45 mph, at which point if speeds were to increase the stresses on various components would result in part failure [18]. Wind turbines of all sizes and power ratings work upon these same principles.

For any open flow wind turbine system, the available maximum power that may be harvested from the air is defined by the below function [19].

$$P_{available} = c_P \rho A V^3 / 2$$

$$c_P = 0.5926 \text{ (Betz Limit, the maximum theoretical efficiency)}$$

$$\rho = \text{density of air at the turbine}$$

$$A = \text{swept area of turbine blades}$$

$$V = \text{speed of air at the turbine}$$

An extremely significant factor in wind turbine efficiency is the Betz limit, which states that the theoretical maximum efficiency of energy transfer from wind energy to mechanical energy in an open rotor system is 59.26% [19]. Actual wind turbines work with much smaller

efficiencies due to irreversible losses. The faster a turbine can rotate at lower wind speeds, the more efficient the transfer of energy from the wind stream to the turbine is. For ideal propeller type designs efficiency would theoretically approach the Betz limit with increase in tip-speed to wind-speed ratio. In reality, common HAWT designs only reach efficiencies of 30-45% for tip-speed to wind-speed ratios between 1 and 5.5 [19]. Research has shown that ducted turbines with optimized diffuser outlets can enhance power efficiency by ~30% past the Betz limit, achieving efficiencies as high as 78% [20]. Exact efficiency values for any given system can only be solved for through experimentation.

HAWT designs are ideal when wind is primarily blowing in a single direction and in areas far away from society where wind speeds can fully develop, tower size and rotor diameter can be maximized, and the noise and sights of turbines do not disturb residents. Vertical axis wind turbines (VAWT) are currently not as effective as traditional HAWT designs, as they are not subjected to the same higher wind speeds HAWT experience. They make up for their lower power output with more aesthetically pleasing designs, lower noise generation, and the ability to be powered by omnidirectional winds. Different VAWT types utilize different blade designs, with some being lift-based like HAWT and some being drag-based, similar to how water wheels work. Lift-based VAWT designs like the “Darrieus” design utilize airfoil cross sections that generate lift which rotate a central shaft. Drag-based VAWTs such as the “Savonius” design have “cups” that capture wind from one side and deflect air around when wind hits the back of the cup. The drawback that comes with being able to harvest wind omnidirectionally is that wind is always working both with and against the mechanism. “Darrieus” and “Savonius” designs typically only operate with 35% and 15% efficiencies respectively [21].

As the search for more sources of renewable energy increases, so does the ingenuity in tackling some of the bottlenecks in current wind turbine system design. As discussed prior, wind turbines have a “cut-out” speed at which brakes are engaged and the system “turns off” and waits the high-speed winds out. Even though these higher wind speeds carry with them more kinetic energy, current turbine designs simply cannot be optimized in such a way that they are able to provide high output powers for both frequent average wind speeds and infrequent high-speed winds. Japanese inventor Atsushi Shimizu invented the “typhoon turbine” specifically to harness the powerful winds that hit Japan during typhoons and other powerful storms. The design makes use of the Magnus effect, which is the tendency of an object rotating about an axis perpendicular to airflow to generate lift perpendicular to the rotating object's axis and wind direction. The rotation of the individual cylinders can be controlled so that the entire mechanism spins at the desired rate. This additive level of control may seem counterproductive for energy generation, but controls become a very important aspect for the environment this particular design would experience [22, 23].



Figure 5: Typhoon Turbine [22]

Starting to gain more attention in academia and industry is the concept of ducted turbines, which are turbine systems that are surrounded by sheaths ahead of and behind a wind turbine. By controlling the velocity profile and streamlines of air as they pass from inlet to outlet, the energy extracted from the air can be maximized to values surpassing what the Betz model predicts. Ducted turbines offer this increased efficiency at the cost of added materials and weight, which has restricted current applications to small diameter turbines. An example of a group which has found success with ducted turbine design is Ducted Turbines International (DTI), a company started out of a research project at Clarkson University. In Figure 6 below is a plot of power generated by the group's turbine designs as a function of wind velocity. In the figure, the power generation of an open rotor design of the same diameter (purple dashed line) is surpassed by the group's ducted turbine technologies. Although ducted turbines are still new to the renewable energy field, they show amazing potential and are likely to lead the way in making green energy technologies more viable for home and business scale clients [24].

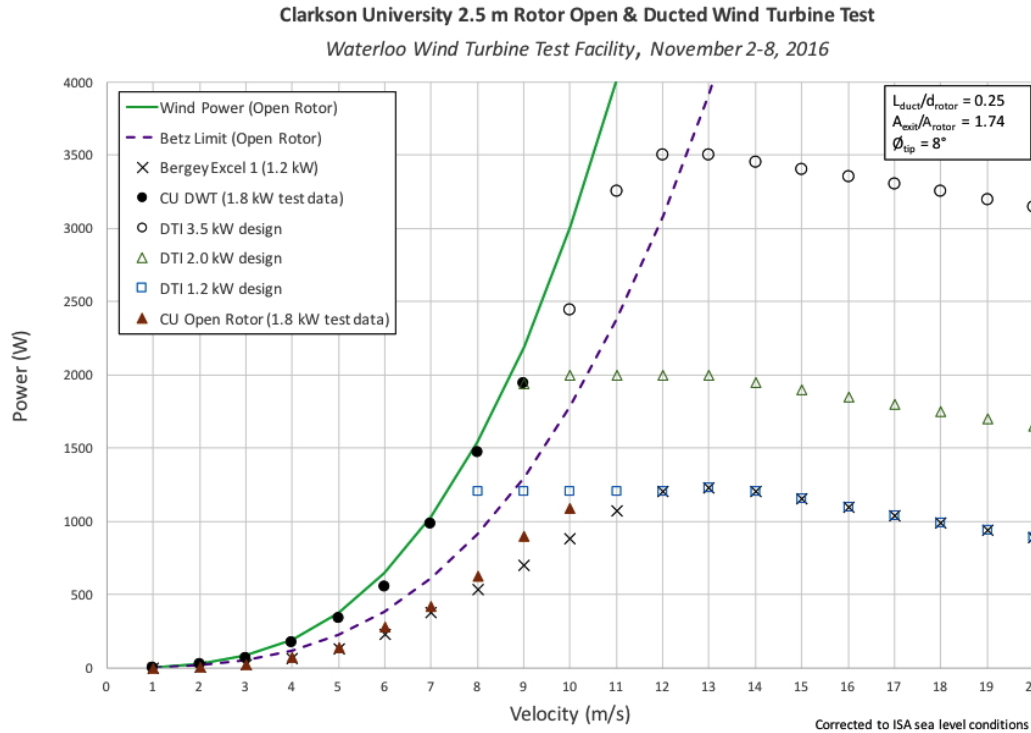


Figure 6: Experimental data for a 2.5 meter diameter wind turbine with and without ducting [24]

2.3.2 - Noteworthy Patents

A number of people have tried to capitalize on the opportunity that high-speed jet blast presents, though no technology achieving this has become commercially available. The team's initial research began by finding an article about an industrial designer who wanted to harness jet blast energy. Richard Hales filed a provisional patent for a design to accomplish this in 2010 [25]. However, this provisional patent expired a year later, and no further attempts were made to revive his project. Other similar patents have been filed with varying degrees of complexity and feasibility. One of these, entitled "Jetair Recovery Generator," consists of a folding flap with an attached horizontal-axis turbine, which spins a flywheel to store the energy. The scale of this device was intended to be rather small, allowing for multiple units to be placed on a single runway [26].

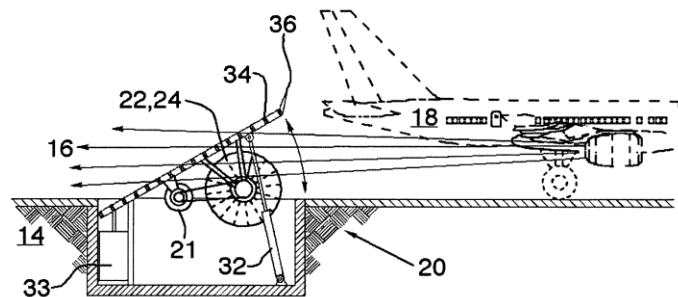


Figure 7: Patent illustration of the "Jetair Recovery Generator" [26]

2.4 - Runway Layout

There are strict guidelines determining the dimensions of runways in the United States. Firstly, the Runway Safety Area (RSA) mandates an area free of virtually anything that could damage aircraft that over- or undershoot the runway [27]. Objects may reside in the RSA as long as they include a frangible point less than 3 inches from the ground to minimize damage to aircraft upon impact [28]. The surface must be able to support planes, as well as things like firefighting equipment and snow removal vehicles. The blast pad is the surface not intended for takeoff or landing, but rather to reduce the erosive effects of jet blast. The threshold, or displaced threshold, refers to the location where takeoff would begin in typical flights. It is also not to be used for typical landings [27]. Figure 8 illustrates these important runway areas and their associated dimensions below.

Runway Safety Area

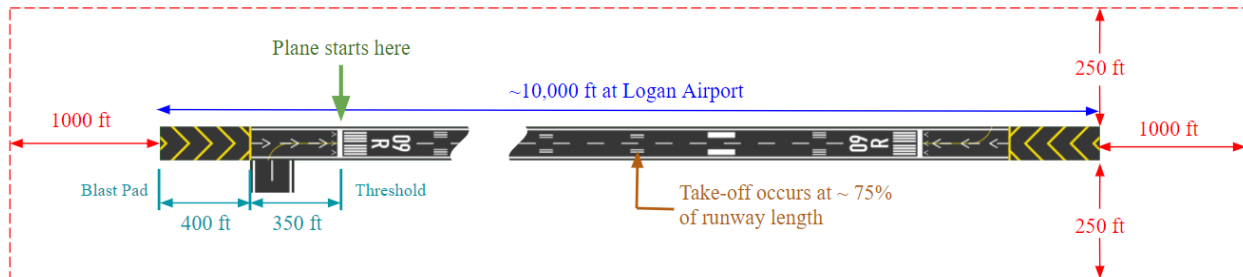


Figure 8: Runway layout with notes [27, 28, 29]

The team decided to use Logan International Airport as the theoretical system site. This was primarily for planning what temperature ranges and weather the system would have to withstand, as well as typical runway dimensions. A typical large runway at Logan is approximately 150 feet in width. The length of the longest runway from Logan International Airport is 10,083 feet. Runways at Logan vary from 7,500 feet to 10,000 feet [29].

3.0 - Project Definition

The project goal for this MQP was to design, prototype, test, and assess the feasibility of a mechanism that harvests energy from jet blast at commercial airports in a manner that is both highly effective in energy production and makes no impact on current air traffic operations.

A set of needs was established for this project. Needs refers to the high-level goals that define a successful project, without detailing the specific method of getting there. This was established through a mix of the MQP team detailing what were considered desirable outcomes for the project as a whole and by applying systems thinking for how airport systems would interact with this project. Figure 9 below illustrates systems thinking and a consideration of the various interfaces the system would experience.

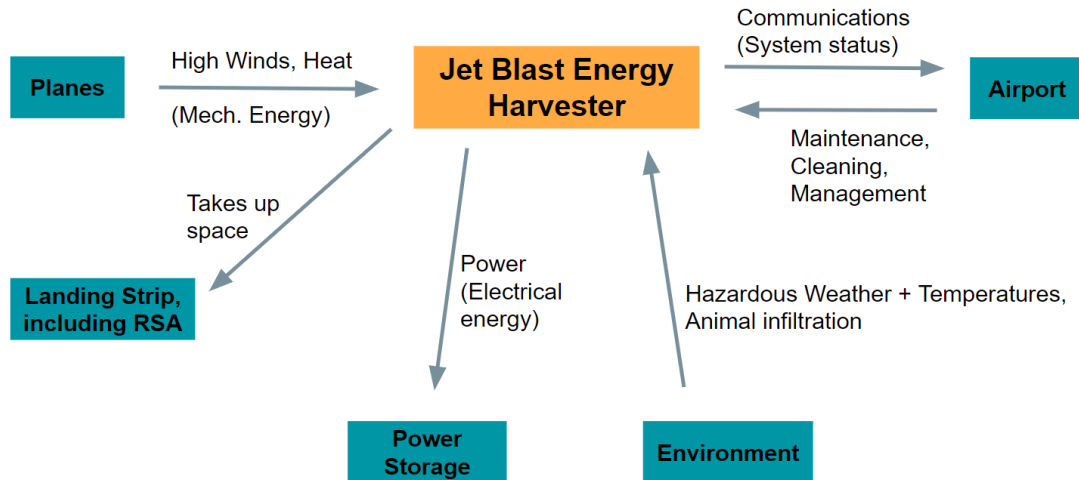


Figure 9: System interfaces

Design requirements consist of “shall” statements which attempt to derive what a project actually must comply with in order to successfully fulfill the specific needs. Requirements are written with as much detail as possible and should have some quantitative value assigned so that the mechanism may be assessed during prototyping and testing. The requirements table (Appendix A) highlights some of the requirements for this project. Each requirement has an ID code for easy referral, a description, a verification plan for how the team would know that requirement has been satisfied, and a priority ranking. For priority nomenclature, a 1 indicates that the requirement **MUST** be met to satisfy the project goal, a 2 means the design should aim to meet the requirement but will not fail without it, and a 3 means the requirement would be beneficial to include but is last as a priority (may be classified as a “want” as opposed to a “need”). Additionally, the table makes a distinction between requirements that the team would meet versus what the system as a whole should comply with but are outside the scope of the project. Seventeen requirements were defined, each with varying levels of technicality and refinement.

4.0 - Design

4.1 - Overall System Design

Two initial concepts were created to meet the design requirements. With both designs, there was a concern on how to incorporate airport regulations in regard to frangible points and emergency landings. For this reason, both initial designs involved stowing below the runway surface, thus not incurring the frangibility regulations. The deflector concept is similar to a traditional jet blast deflector. The mechanism deploys out of the ground and has a turbine directly implemented into the face of the deflector. The turbine’s central axis may be perpendicular to or coincident with the deflector face.

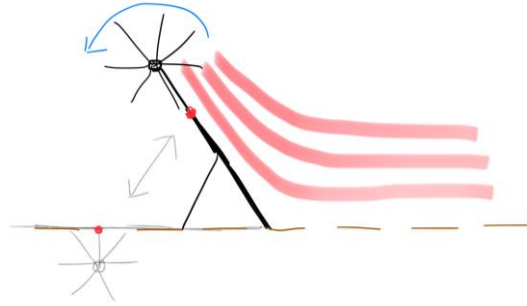


Figure 10: Jet Blast Deflector turbine concept

This design has components which have similar purposes to devices already in use in industry, which may mean that implementing it would be easier. The largest concern with this design was the connection from the turbine to the generator.

The next concept involved a funnel or flap that is stowed underground and deployed to redirect jet blast air into a duct system. The ducts lead to a static turbine bank and generators. Stowing is initiated if the runway is needed for landings. The initial ducting would cause the fluid to increase in velocity as it leads to the turbine and generator. This effect is referred to as the Venturi effect. The Venturi effect describes the tendency of a fluid to speed up as it goes from one cross sectional area to a smaller one since mass flow rate must be conserved.

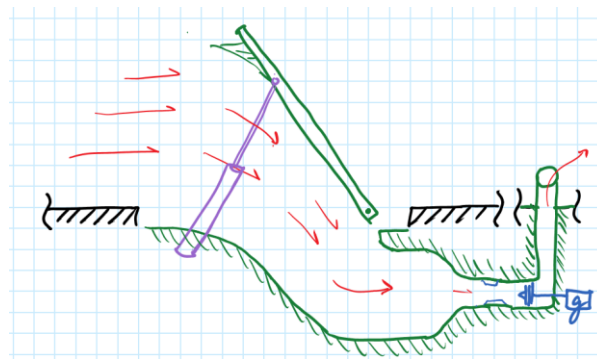


Figure 11: Underground flap concept

This design was favored because of its relative simplicity and its large inlet area. By going from a large intake area to a smaller duct area where a turbine may be stationed, airflow speed is increased via the Venturi effect (Figure 12). The potential power by a typical wind turbine under these conditions would be calculated by the equation in $P_{\text{available 1}}$. To achieve a velocity V_2 that is X times higher than V_1 , area A_1 must be X times larger than A_2 , assuming incompressible flow. Since mass must be conserved and density is approximately constant, the velocity will have increased with a reduction in area. If $P_{\text{available 2}}$ is solved for as a function of area-increase-factor X algebraically and compared against $P_{\text{available 1}}$, $P_{\text{available 2}}$ is larger than the power generated by the original system by a factor of X^2 .

$$\begin{aligned}
P_{available\ 1} &= c_p \rho A_1 V_1^3 / 2 \\
P_{available\ 2} &= c_p \rho A_2 V_2^3 / 2 \\
\rho_1 A_1 V_1 &= \rho_2 A_2 V_2 \\
X &= A_1 / A_2 \\
V_2 &= X * V_1 \\
\rho_1 &= \rho_2 \\
\text{Therefore, } A_1 &= X * A_2 \\
P_{available\ 2} &= c_p \rho (A_1 / X) (X * V_1)^3 / 2 \\
P_{available\ 2} &= X^2 * P_{available\ 1}
\end{aligned}$$

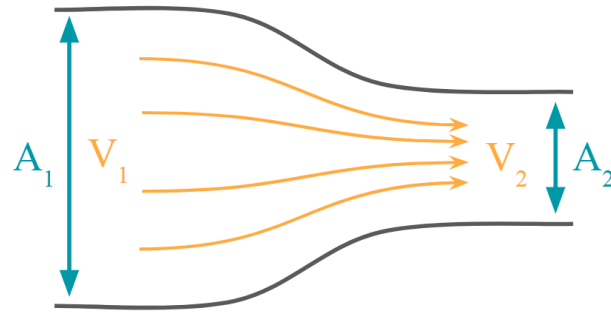


Figure 12: Venturi effect

The proposed system is intended to be placed on the blast pad of the runway (see Figure 13, C location). Other locations were considered but they were all discounted because they were too far away to accumulate optimal power (A and B locations), or they would disrupt the flow of typical traffic (D and E locations). Therefore, the blast pad was chosen as it is not used in normal landing procedure and is as close as the system can get to the aft of a plane without being in its path of travel. With enough forewarning the system can be stowed, allowing the runway to be safely used by landing aircraft.

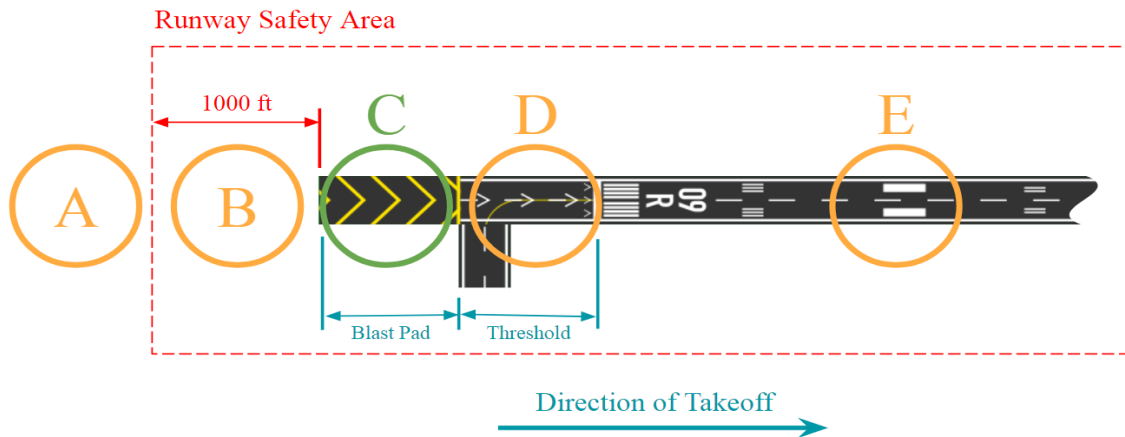


Figure 13: Mechanism location assessment

Figure 14 shows the overall system. At the entrance there exists a shutter system that will protect the duct system from environmental hazards (detail 2). The primary flap is intended to collect and redirect the jet blast flow into the duct system (detail 1). This will be particularly important in the later stage of each plane's takeoff sequence. The secondary flap, shown in detail 3, assists with the desired flow path while also allowing for extra space for the primary flap when both are in the closed position. There will be ten 15-foot wide sections of flap that will be independently actuated. A hydraulic piston pair, shown in detail 4, will initiate the raising and stowing of the flap mechanisms. Following the duct entrance, flow will be separated (detail 5) to meet a row of 12 turbines in the system (detail 7). Load bearing structures will disperse any overhead load around the ducts (detail 6). These structures extend from the ground below the

duct to the bottom of the pavement of the runway. Following the turbines, the fluid will diffuse until it reaches ground level (details 8, 9).

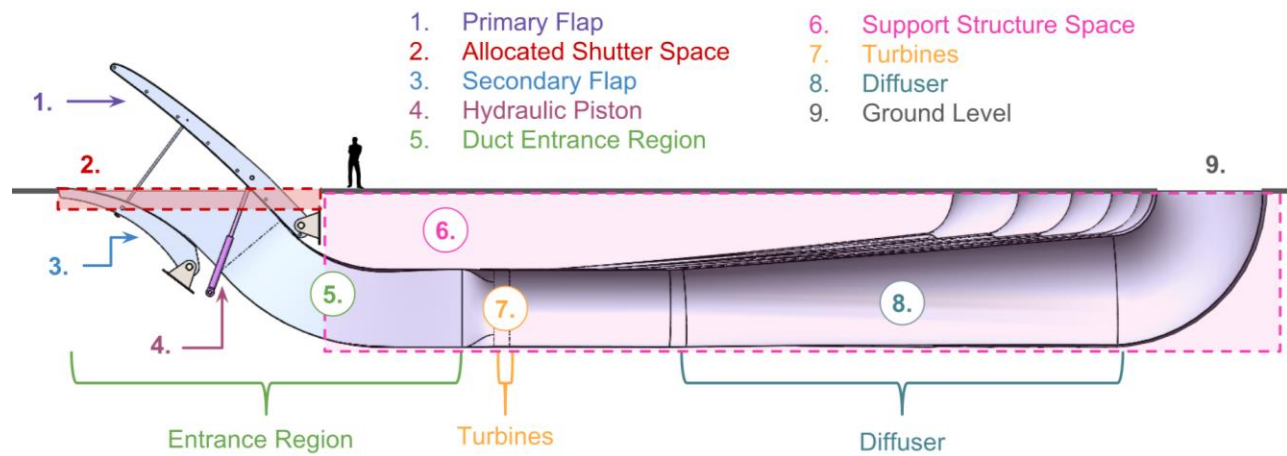


Figure 14: Overall system diagram

A simple model of how a prospective shutter mechanism may work is shown in Figure 15 below. The allocated space for the shutter system is sized to extend no more than three feet deep below the runway's surface, which constrains the placement of the hinge for the primary flap and other system parameters. While the flap is stowed, the shutter system is free to move over and protect the inlet mechanism (detail d). It is centered width-wise with the edge of the runway and is twice the width of the runway. Like the rest of the system, it has a weight requirement of two feet of snow and should open or close in 30 seconds. The shutters would roll over lengths of rails that run across the width of the runway belowground and may be moved in and out of place by a pulley-winch system. A flange bridges the gap over the rails so that flow can smoothly transition from over the runway surface to the duct system (detail e). The shutter system itself is not essential to the process of capturing jet blast so it is not detailed technically in this report.

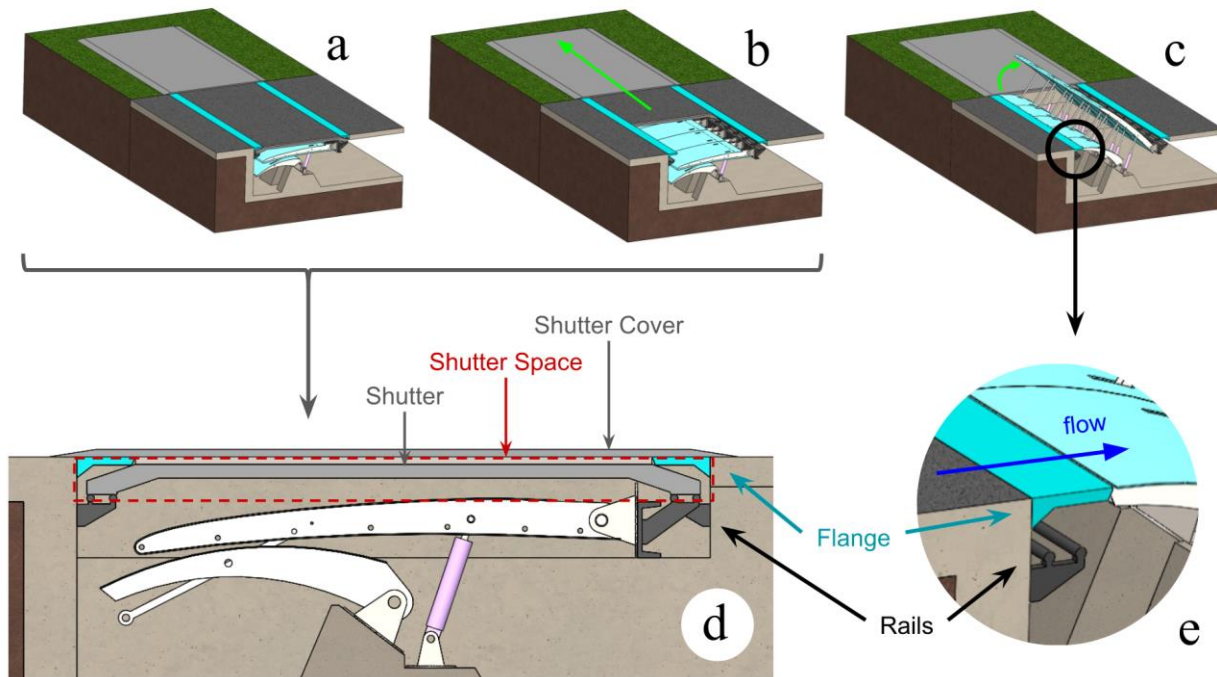


Figure 15: Shutter mechanism, showing closed position (a), opening movement (b), and open (c)

A minimum spacing of one foot exists between all of the turbine tubes and the diffusers so that a support structure may be placed to bear overhead loads. 10-inch square I-beams are placed between every turbine and every 10 feet along the diffuser lengths. The structural placement was decided based on iterating the above-mentioned dimensions until the horizontal beam spans deflections were minimized (see Figures 16 and 17). Structural analysis for these supports is shown in section 5.4.2 - *Support Structure Analysis*.

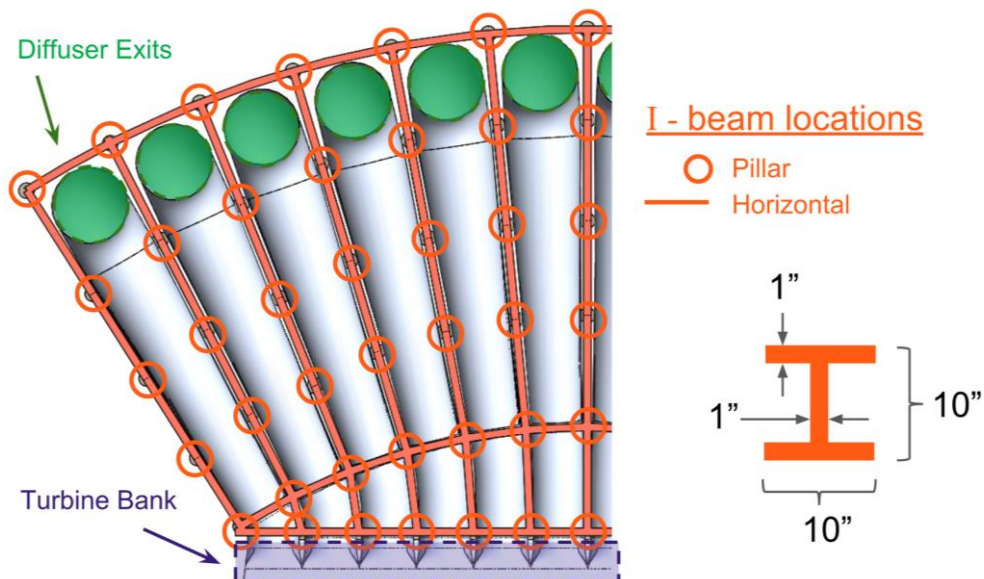


Figure 16: Support structure beam locations

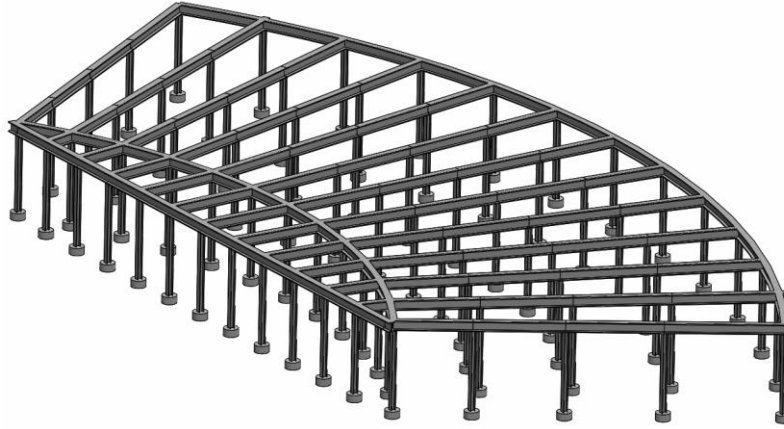


Figure 17: Support structure layout (top) and model (bottom)

4.2 - Design Considerations

In order to define the primary operation case and avoid unnecessary complications, the team came up with a list of operational assumptions. The bases for these assumptions range from airport planning to fundamental physics. They are organized by what aspect of the project they pertain to.

The plane is assumed to be 350 feet from the duct opening of the system when the takeoff sequence begins at the front of the threshold. Therefore, high jet blast temperatures will dissipate into the environment long before encountering the system. The duct opening would be in the forward part of the blast pad. The plane in question, assumed to be a Boeing 747-400, accelerates at a constant rate and lifts off from the runway after 50 seconds, at a speed of 180 mph.

A model of the plane's velocity and position as a function of time was created to describe the jet blast over each cycle of use. Boeing data provides information on jet blast velocities instantaneously at takeoff but does not describe how jet blast varies as a function of time as the plane moves down the runway. Assuming a 747-400 constantly accelerates from 0 to 180 mph in 50 seconds, simple kinematic equations can model the plane's movement, as shown below.

$$\begin{aligned} \text{Plane acceleration} \quad a &= \frac{180\text{mph}}{50\text{s}} = 5.28 \frac{\text{ft}}{\text{s}^2} \\ \text{Plane speed} \quad V_{\text{plane}}(t) &= a \cdot t \\ \text{Plane's distance from flap inlet} \quad x(t) &= \left(\frac{1}{2}a\right) \cdot t^2 + 350\text{ft} \end{aligned}$$

The team also based the theoretical jet blast on the 747-400. Said data was used to create parabolic equations as approximations of the velocity profile lines. These equations were put into ANSYS Fluent to create a simulation of the jet blast and are discussed more fully in section 5.2 - *Fluids Analysis*.

The team also standardized several assumptions about the jet blast harvesting system itself. In order to not take up too much space, it was decided that the entire system would not

take up more than 20 feet of depth underground, and would not be more than 200 feet wide or long. This width does not include the shutters, which by design need to open enough to expose the underground system. The shutters are presumed to be no more than 3 feet deep. The team also decided to allot 10 feet of that depth for structural support around the turbines, as described in the previous section. To determine whether the flow exhibits incompressible or compressible fluid characteristics, the speed of sound (c) needs to be calculated. With the ratio of specific heats (k) being 1.4, the gas constant (R) being 1,716 ft-lbf/R-slug, and the temperature being 536.4 R (the temperature of an average day) the speed of sound was calculated.

$$c = \sqrt{kRT}$$

$$c = \sqrt{1.4 * (1,716 \frac{ft \cdot lbf}{R \cdot slug}) * (536.4 R)} = 1,135 \text{ ft/s} = 774 \text{ mph}$$

If the theoretical maximum velocity in the system is less than 0.3 times this calculated speed of sound, then the fluid may be modeled as incompressible [19]. This constrains how much the duct area can be reduced. The maximum air speed the system experiences is, in reality, lower due to irreversible losses and never approaches this compressibility limit.

$$M = V/c = 250 \text{ mph} / 774 \text{ mph} = 0.32$$

This Mach number is greater than the incompressible fluids limit of 0.3 [19]. In compressible fluid flow, various effects such as shock waves and efficiency losses would be significant. Instead, incompressible fluid flow limits the mechanical stresses, noise, and vortices in the flow. The fluids in this study are considered to be incompressible rather than compressible because of the following:

1. Flow only surpasses the limit in a theoretical case where the entire inlet area uniformly experiences jet blast at speeds of 100 mph, whereas in reality 90% of the inlet velocity profile is under 100 mph
2. In realistic flow conditions, vortex effects present at the underside of the flap will lessen the airflow actually reaching the duct system

ANSYS simulations discussed in section 5.2 - *Fluids Analysis* validate this, with the maximum speed at the turbines reaching 128 mph.

It was also assumed that the system's turbines would not significantly affect flow conditions such as pressure and enthalpy. This was necessary considering that the team was not focusing on actually designing the turbines, instead leaving that for a future iteration of the project. An optimistic efficiency of 75% was assumed for power production, based on research for ducted turbine power generation mentioned in section 2.3.1 - *Wind Energy*.

4.3 - Duct Entrance Region

The duct entrance region of the system encompasses all aspects of the design that first alters the flow of the jet blast before it reaches the turbine system. Data from Boeing indicates that the jet blast can reach speeds up to 100 mph at an elevation of 15 feet above the runway surface 350 feet from the aft of the aircraft. To maximize flow capture while minimizing height,

15 feet was selected as the inlet height of the system, with the inlet width spanning 150 feet (the typical width of a Logan runway). With this inlet area and jet blast data from Boeing (indicating max wind speed of 146 feet/second 350 feet behind the aircraft), mass flow (\dot{m}) and volumetric flow rate (\dot{Q}) may be calculated and initial power production estimates may be created.

$$\dot{m} = \rho * A * V$$

$$\dot{m} = (0.00238 \text{ slugs/ft}^3) * (15 \text{ ft} * 150 \text{ ft}) * (146 \text{ ft/s}) = 784.6 \text{ slug/s}$$

$$\dot{Q} = A * V$$

$$\dot{Q} = (15 * 150 \text{ ft}^2) * (146 \text{ ft/s}) = 328,500 \text{ ft}^3/\text{s}$$

To determine the turbine area of the duct entrance, a desirable turbine velocity was selected. As discussed previously, generated power from a wind turbine system increases in a cubic manner with wind velocity, so it is advantageous to speed up the air as much as possible. The maximum allowable wind speed was selected to 250 mph in accordance with reasoning provided in the last section.

Because the turbine is ducted, inlet-to-turbine area ratio changes the speed of wind in front of the turbine and thus the power it produces. Figure 18 below shows what the turbine diameter and wind speed would need to be to satisfy the range of target power production values along the horizontal axis. With a target power production of 15.4 MW, an inlet area of 15 x 150 square feet, and 12 wind turbines, velocity at each turbine is calculated to equal 250 mph, with turbines being 9.8 feet in diameter. This target power production value is a theoretical maximum that the system would only experience in the event of prolonged jet blast from a parked aircraft.

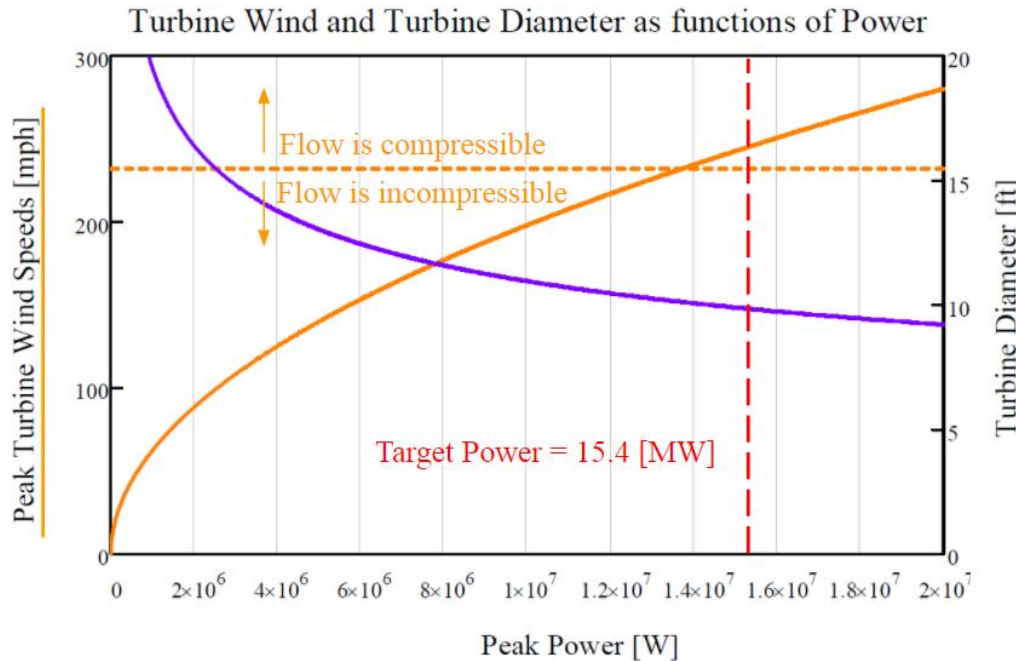


Figure 18: Dependence of turbine characteristics as functions of power

To solve for the geometry of the turbine region, a quantity of turbines was selected based on iteration. A system featuring twelve turbines results in a corresponding turbine diameter of

9.85 feet, which complies with the maximum dig depth requirement of 20 feet and overhead load bearing structure space requirement of 10 feet to distribute overhead load. Lining up twelve of these turbines side by side with 1 foot spacing between outer diameters results in an overall width of 132 feet, which is shorter than the inlet area's width. This is a desirable feature in the system because if the turbine area's width was larger than the inlet area's width, the flow would only be converging in the side plane and would be diverging in the top plane. It is desirable to have the duct converging in both planes so that flow direction is fairly similar across the duct cross-section, as opposed to flow diverging near the edges and potentially causing vortices. Figure 19 below depicts the inlet and turbine area with dimensions.

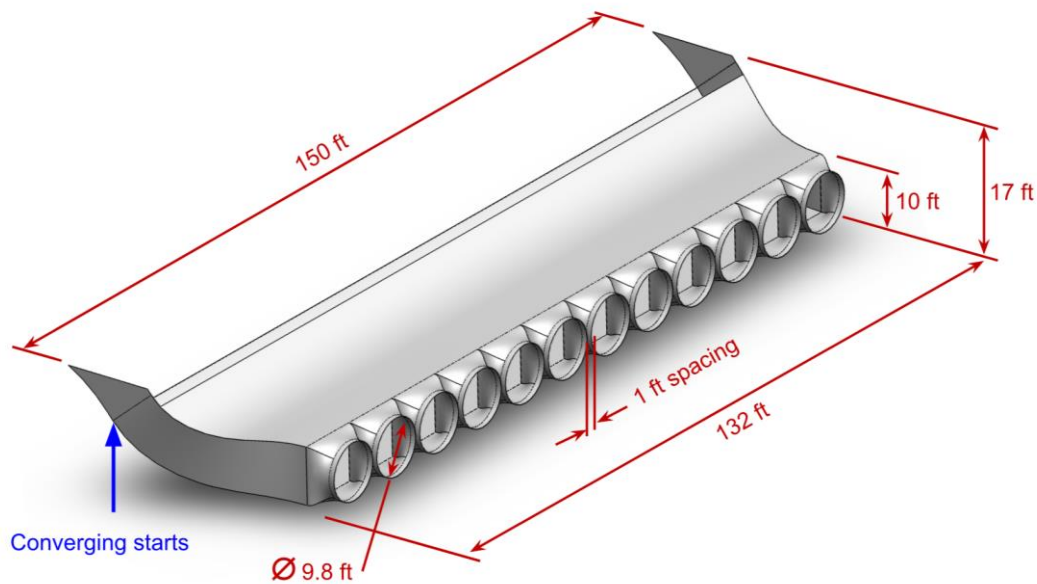


Figure 19: Duct entrance cross sections

Figure 20 below shows a side-view cross section of the entrance region and flaps, along with constrained dimensions which are discussed further below.

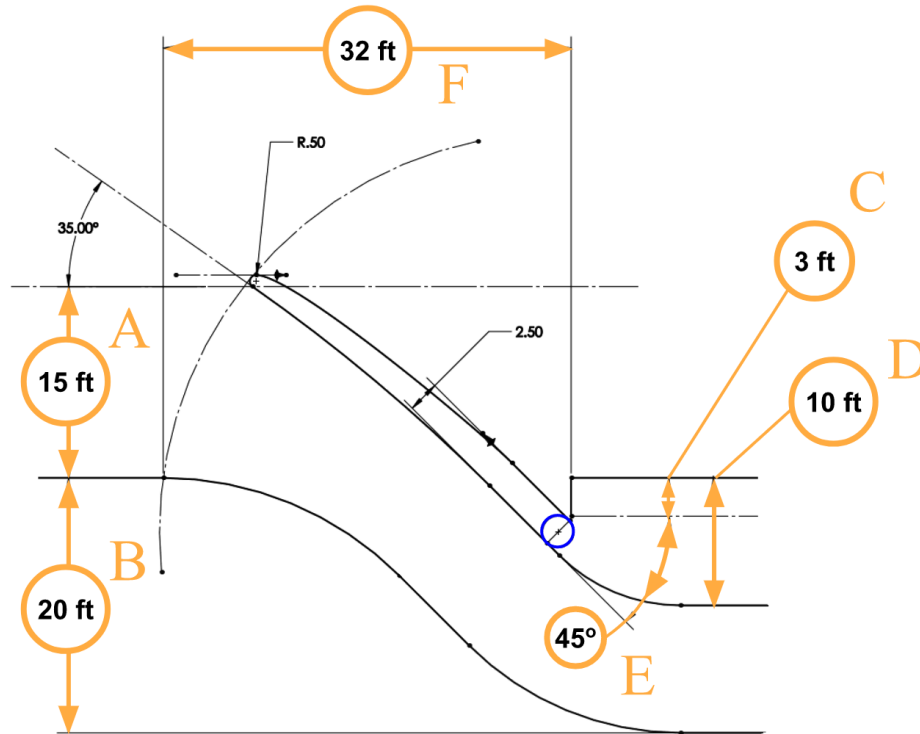


Figure 20: Duct entrance constraining dimensions

Dimension “A” measures from the top of the runway surface to the tip of the flap and was determined to be 15 feet based on jet blast velocity profiles from Boeing. Dimension “B” is the Dig Depth of the system, which limits how deep into the ground the main features of the system may extend. The team decided to restrict this dimension to 20 feet based on a trade-off between smoothness in the transition from the runway. Any shallower and there would need to be a shorter flap that captures significantly less jet blast. Dimension “C” refers to the space that the team has allocated for the shutter system. The blue circle that lies tangent to this line is the pivot of the primary flap. The location of this circle’s center is automatically fixed by SolidWorks, since the drawing is constrained. The circle's diameter may be taken to be the maximum cross-sectional width the primary flap may take up in order to rotate into its uppermost position and fold down without colliding with any other areas of the system. Dimension “D” represents the space that has been allocated for the runway and its load bearing structure. Dimension “E” defines the turn angle of the flow velocity (assuming flow will travel parallel to the walls). Ideally, the flow should be interfered with as little as possible to minimize energy losses and chances of vortex formation. The smaller this angle, the longer the primary flap must become in order to still extend 15 feet into the air, which would increase material cost,

hydraulic load requirements, surface that jet blast flow must pass over before reaching the turbines, dimension “F”, etc. If this angle becomes too large, the duct must make turns at increasing sharp angles which results in more energy loss. A dimension of 45 degrees is optimal because it redirects the flow just enough to reach the turbines without either having an impractically large primary flap or losing energy with sharp turns. Dimension “F” represents the length of runway over which the shutter must extend in order for the primary flap to completely rise up. The team iterated this dimension and other constraint dimensions, attempting to minimize this value, with the final iteration measuring 32 feet. Through all these dimensions and various geometric constraints, the entirety of the duct entrance’s side profile is completely constrained.

With the side profile defined the primary and secondary flaps may be designed off of this sketch, as shown in Figure 21. This speeds up design iteration and simplifies the model, as whenever a system dimension is changed the entire model will update. Everything from hydraulic piston placement optimization to flap travel path can be calculated and updated instantaneously in SolidWorks.

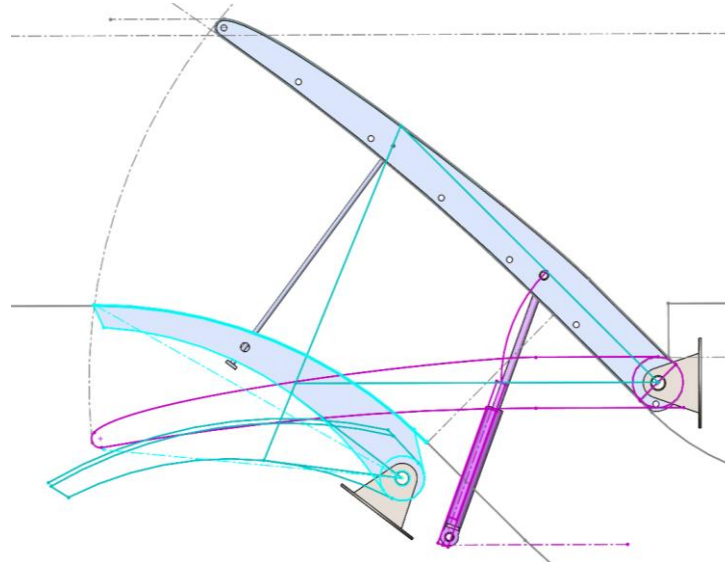


Figure 21: Constraint relation to model

The entrance region simply funnels from the inlet to the turbines as smoothly as possible. The outer walls of the duct do not begin converging until after the hydraulics, as otherwise there would be no space for the primary flap to lower into. At the turbine region, spacers of 1-foot width exist between each turbine location to allow for support columns and any turbine hub fixtures that may be required in a fully realized design. The walls in these spacer regions are smoothly curved so air on a trajectory aimed in-between turbine blade swept areas is redirected and funneled into the closest turbine. From each individual turbine tube, the duct is lofted towards the entrance region from a circular to rectangular cross-sections. Where the lofts intersect each other at the entrance, there is a sharp rounded curve in the sheet metal to minimize obstruction to flow (Figure 22). Past the turbine region, the slower moving air is directed to the diffuser system.

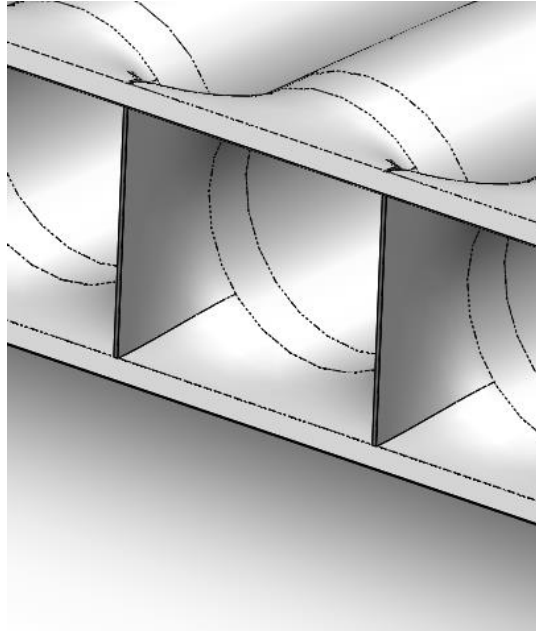


Figure 22: Splitting duct entrance flow to individual turbines

4.4- Primary and Secondary Flaps

The geometry of the primary flap is critical because of how it affects the flow of the jet blast throughout and following the system. To analyze various geometries, the team used ANSYS Fluent, a computational fluid dynamics simulation software. Thirteen flap variations were considered. The flow for a simplified and steady state scenario was assumed to vary linearly with height, starting at 100 mph at the surface of the runway and ending at 50 feet above the runway at 50 mph (see Figure 23). The height of this varying inlet was determined from the Boeing velocity profiles 350 feet behind the plane.

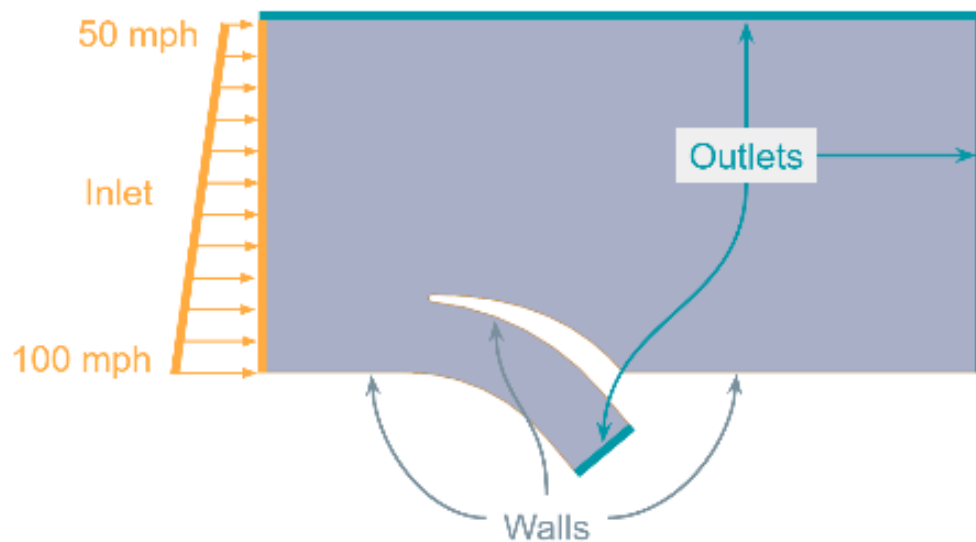


Figure 23: CFD steady state scenario inputs

There were 5 types of flap geometries, shown in Figure 24, that were analyzed. Other characteristics considered in these analyses were the shape of the tip, the tip angle, the swing radius of the entire flap, and height of the flap during use (see Figure 25). Overall flap geometries are summarized in Table 4. The gray fill in certain cells indicates that the geometry was constrained in other ways.

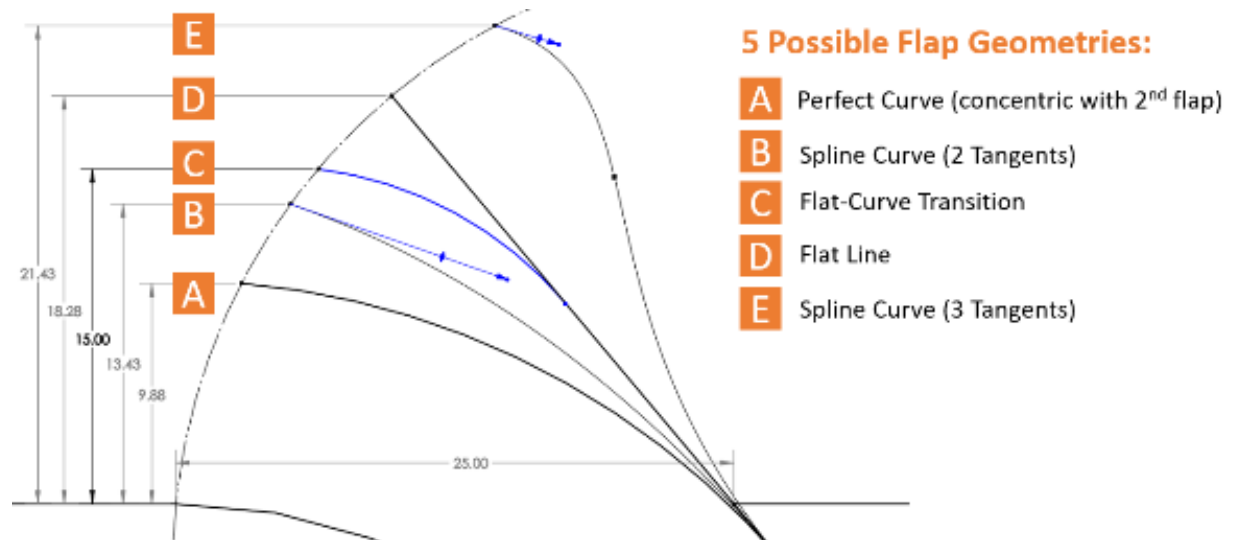


Figure 24: Flap geometry for Table 1

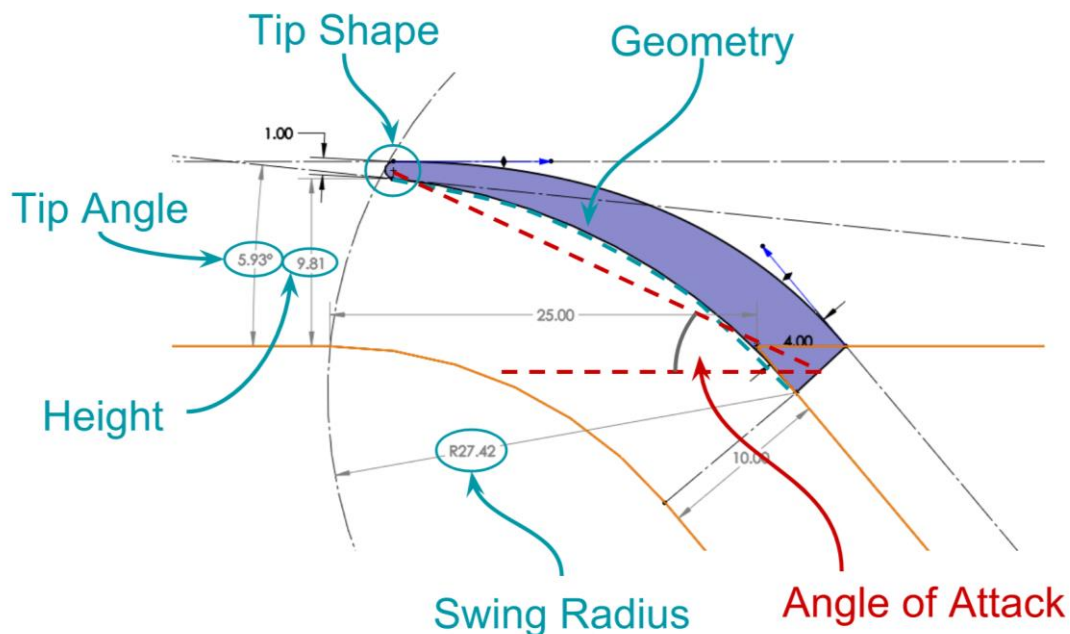


Figure 25: Flap characteristic key for Table 1

Table 1: Flap iteration definitions

File Name	Geometry	Tip Shape*	Tip Angle	Height (ft)	Swing Radius (ft)	Angle of Attack (deg)	Comments (Figure 24)
FlapTest_0	No Flap	b	N/A	N/A	N/A		
FlapTest_1	Perfect Curve	b	5.93 deg	9.81	27.42	20.96	A, concentric w/ 2 nd flap
FlapTest_6	Perfect Curve	b	26.72 deg	6.20	15	24.41	A, concentric w/ 2 nd flap
FlapTest_2	Spline (2T)	b	0 deg	15	27.42	33.16	B
FlapTest_3	Flat w/ Curve	b	0 deg	15	27.42	33.16	C
FlapTest_9	Flat w/ Curve	b	20 deg	15	27.42	33.16	C
FlapTest_4	Perfect Curve	b	20 deg	12.64	27.42	27.45	C/A (perfect curve, not concentric)
FlapTest_5	Perfect Curve	b	32.65 deg	15	27.42	33.16	C/A (perfect curve, not concentric)
FlapTest_7	Flat	b	50 deg	15	23.64	39.38	D
FlapTest_8	Spline (2T)	b	0 deg	15	27.42	33.16	E
FlapTest_10	Flat w/ Curve	s	0 deg	15	27.42	33.16	C
FlapTest_11	Flat w/ Curve	s	20 deg	15	27.42	33.16	C
FlapTest_12	Flat w/ Curve	vb	0 deg	15	27.42	33.16	C
FlapTest_13	Flat w/ Curve	vb	20 deg	15	27.42	33.16	C

* b = Bulbous Diameter= 1 ft | s = Sharp Diameter = 1 in | vb = Very Bulbous Diameter = 3 ft

ANSYS Fluent 18.2 was used to perform 2-D computational fluid dynamic analysis on each of the thirteen geometries. Flap 5 was chosen because of its simulated effects after the flap geometry over the runway as well as the desirable speeds within the duct (see Figure 26). Overall there was a slight reduction in speed of the jet blast after the flap, and an increase in velocity within the duct. There were no vortices in any location that heavily affected the flow. The geometry of the inner duct workings changed in more detailed transient analyses, shown in section 5.2 - *Fluids Analysis*.

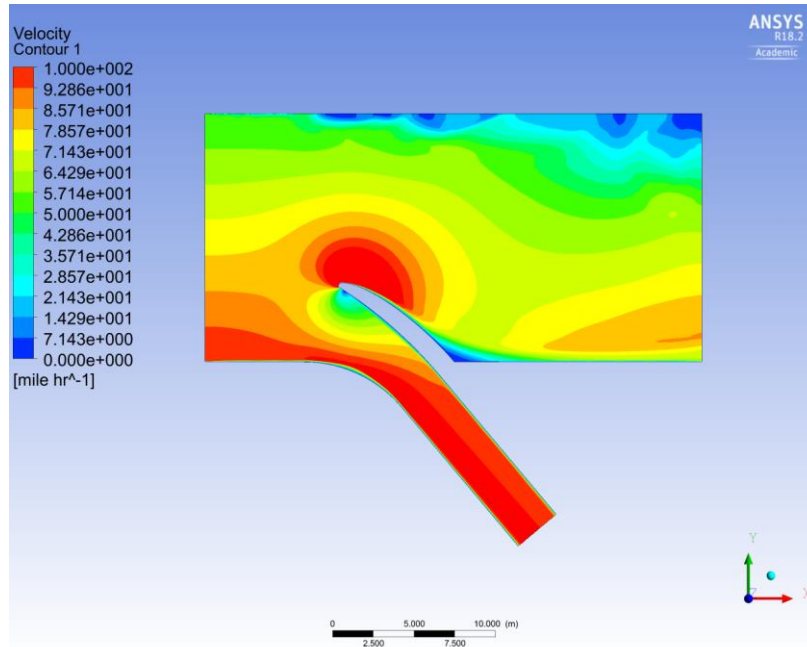


Figure 26: ANSYS simulation results for Flap 5 Steady State Velocity

Each flap surface and flap rib is planned to be constructed from stainless steel sheet with a smooth and matte finish. AISI 301L stainless steel was chosen for its non-magnetic properties, high stiffness, machinability, good surface finishing options, excellent water resistance, and relatively low price-per lb. Some examples of other materials that were considered and how they size up in comparison to our selected steel are listed in Table 5 for consideration and were found through GRANTA's CES EduPack.

Table 2: Material properties

Material Name	Price (\$/lb)	Density (lb/ft ³)	Young's Modulus (psi)	Yield Strength (psi)	Tensile Strength (psi)	Fracture Toughness psi(in ^{1/2})	Roughness (in)
Epoxy/aramid fiber, UD prepreg, UD lay-up	21.7271	86.15064	8.70E+06	1.80E+05	1.80E+05	51236.378	5.49213E-05
Polyester SMC (50% glass fiber, HB)	1.614791	108.00044	1.71E+06	2.33E+04	2.33E+04	45320.988	0.000184383
Stainless steel, ferritic, AISI 446	0.825539	468.21	2.90E+07	4.53E+04	7.94E+04	88275.82	0.000491505
Aluminum 520.0	0.90265	160.7521	9.57E+06	2.68E+04	5.13E+04	19566.29	0.000517414
Stainless steel, AISI 301L	1.03646	494.42976	2.97E+07	3.19E+04	7.68E+04	56423.72	0.000491505

The entire system spanning the runway has ten 15-foot sections, which simplifies manufacturing and assembly feasibility and allows for the system to be installed on runways of any width. Each flap section has two pairs of ribs on the ends of the flap. Supporting cross-beams within the flap itself connect to each rib and constrain the surface to help maintain the curved profile. This feature also aids in preventing each rib pair from becoming misaligned with

the other side, which could induce significant stresses on the flap surface. The ribs would be formed by cold working 0.8-inch-thick stainless-steel sheet into rectangular cross sections. The hydraulic and wire rope attach in between each rib pair, allowing for double-shear support (see Figure 28). Hinges at each rib's center of rotation connect the flaps to support sections that run the length of the system. Figure 27 below shows an annotated view of the primary and secondary flap and all of the interrelated components, as well as a cut-away view of the primary flap to optimally illustrate the cross-section of the ribs and the double-shear connections to other components.

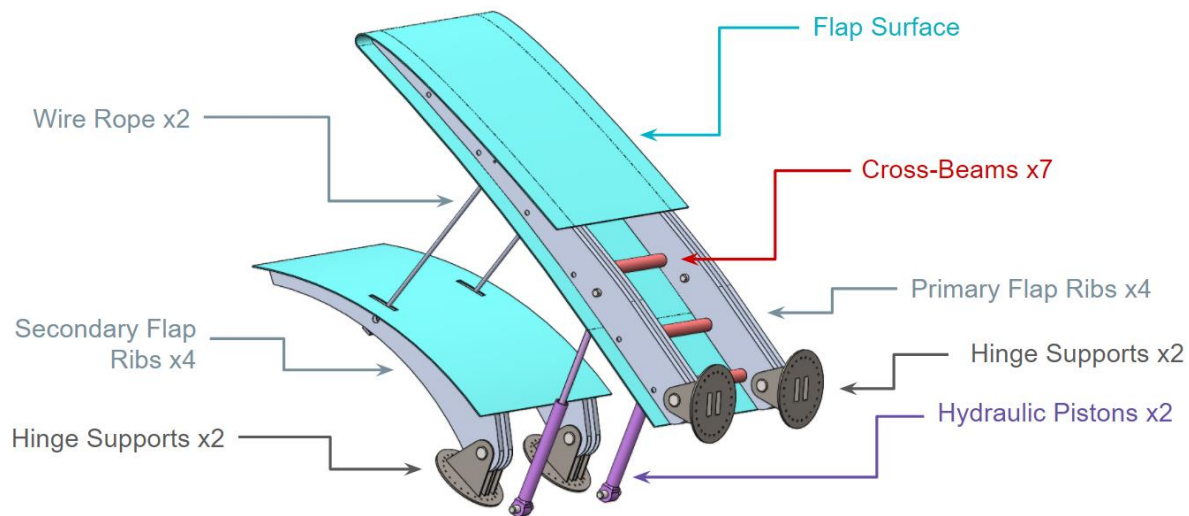


Figure 27: Flap section with labels

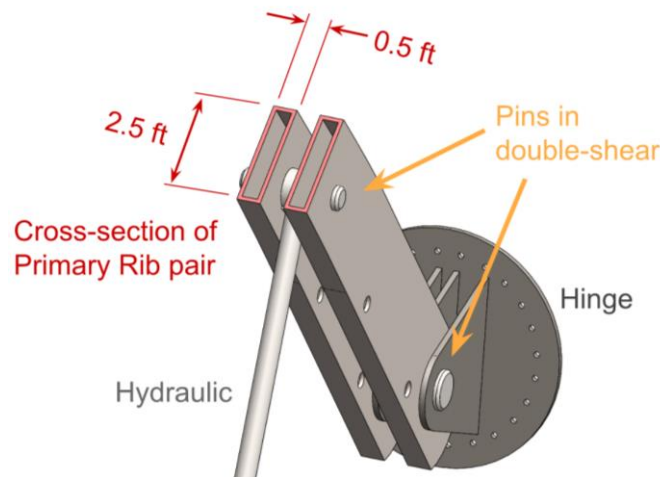


Figure 28: Cross-section of primary flap rib pair

The secondary flap has a similar design to that of the primary flap, though its tip is designed to meet the surface of the runway in its raised position (the “flange” as shown previously in Figure 15 detail e). This will prevent severe vortex formation from the jet blast moving over an abrupt corner before entering the duct.

4.5 - Closing Mechanism

While this project's 15-foot height is dwarfed by typical wind turbines, it is a significant obstacle for planes that come in for landing. By having the flap raise and lower when needed, effects on air traffic operations are minimized and the primary flap can be stowed below the level of the runway. There are multiple design opportunities that could each support this functionality including hydraulic systems, direct geared drives, or cable and pulley systems as outlined in Table 6.

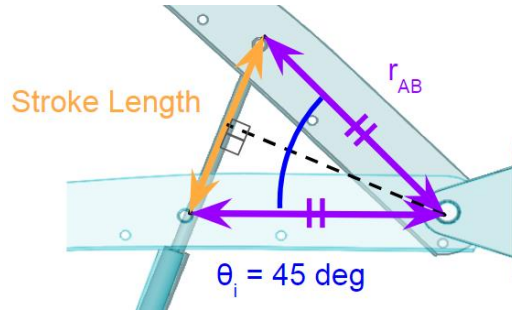
Table 3: Mechanism design table

Hydraulics		Direct Drive		Cables / Pulleys	
Pros	Cons	Pros	Cons	Pros	Cons
Reliable	Efficiency	Would not seriously affect flow intake	Complicates hinge assembly / chance of failure	Would not seriously affect flow intake	Complicated, lots of areas for failure
Easily repairable	Would affect flow intake	Takes less space	Would need brake/clutch mechanism	Takes less space	Would need brake/clutch mechanism
Simple (motion)			Difficult to access, costly to replace		Will need to use pulleys or multiple cables to support the weight
Proven to work in hazardous conditions			Huge stresses on shaft		

With hydraulics, the tube and piston assembly would be placed inside the intake duct area and oriented in a near-vertical position. The direct drive mechanism would be actuated by a motor connected to the same shaft that supports the flap. The cable and pulley mechanism would use wire rope to lift the flap from behind the hinge.

Ultimately, the hydraulic system was chosen for its versatility and numerous advantages. The tank pressure of such a system would be around 1293 psi with a cylinder head diameter of 6 inches. The stroke length would need to be 6.3 feet to properly lift the flaps into the upright position. Lifting one section of flap in approximately 30 seconds would require roughly 13.98 hp of power, with a pump moving fluid at roughly 0.31 gallons per second.

$$F_H = 36550 \text{ lbf (from section 5.4.1 - Mechanism Analysis)}$$



Stroke length	$s_H = 2 \cdot \left(r_{AB} \cdot \sin\left(\frac{\theta_i}{2}\right) \right)$	$s_H = 6.313 \cdot ft$
---------------	---	------------------------

Area	$A_H = \pi \cdot \left(\frac{d_H}{2} \right)^2$
------	--

Power	$P_{lift} = \frac{F_H \cdot s_H}{t_{lift}}$	$P_{lift} = 13.982 \cdot hp$
-------	---	------------------------------

Pressure	$p_H = \frac{F_H}{A_H}$	$p_H = 1.293 \times 10^3 \cdot psi$
----------	-------------------------	-------------------------------------

$$P_{lift} = U_{dot} \cdot p$$

Vol flow needed	$U_{dot} = \frac{P_{lift}}{p_H}$	$U_{dot} = 0.309 \cdot \frac{gal}{s}$
-----------------	----------------------------------	---------------------------------------

Total Energy to Raise Flaps	$E_{lift_T} = P_{lift} \cdot t_{lift} \cdot 2 \cdot sections$	$E_{lift_T} = 5.929 \times 10^3 \cdot BTU$
-----------------------------	--	---

A cable connects the two flaps to minimize the mechanisms used, although this does make the single piston's load greater than if the secondary flap had its own pair of pistons. The cable that would be needed to lift the secondary flap is tabulated to be 1-inch diameter uncoated, fiber core wire rope with improved plow steel with a safety factor of approximately 4 to hold 4000 lbs safely (cable tension determined in section 5.4.1 - Mechanism Analysis) [30]. One cable end is simply attached to the primary flap, while the bottom end has a stopper fitting with a cross section larger than the space between the two rib pairs. This allows for extra length of cable to settle below the secondary flap when stowed, as opposed to becoming slack and getting tangled with other components or in between the flaps. Figure 29 details the raised and closed flap orientations.

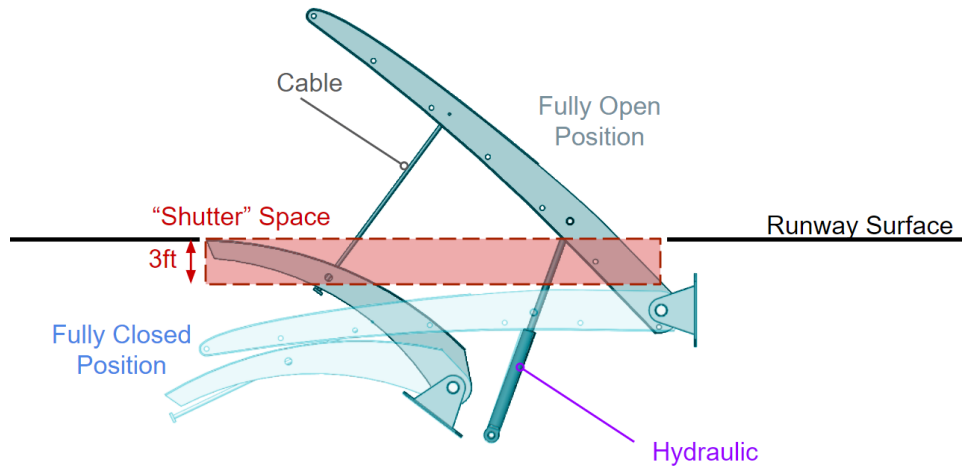


Figure 29: Mechanism deployed and stowed positions

4.6 - Duct Exit Region

Beyond the turbine bank, a diffuser was incorporated to regain pressure and decrease velocity. Since the flow velocity is increased significantly by the entrance funnel, it must be reduced again to a safe threshold. In addition, having a high-speed, low-pressure flow suddenly enter ambient surroundings could lead to a severe loss of efficiency. It is important to ensure the flow does not slow down so much that stagnation occurs. Stagnation is when local fluid velocity reaches zero, and often leads to vortex formation. In a ducted system, this would also lead to upstream efficiency loss. Unfortunately, with no finalized turbine design, it is impossible to accurately design a diffuser that will perfectly fit the system's needs. For now, the team opted to use the Bernoulli equation to approximate pressure before the turbines, and estimate the pressure change across the turbines as negligible. This would be true in the case of a reaction-type turbine, where only kinetic energy is harnessed from the jet blast as opposed to pressure.

$$P_1 + \frac{1}{2}\rho V_1^2 + \rho \cdot g \cdot z_1 = P_2 + \frac{1}{2}\rho V_2^2 + \rho \cdot g \cdot z_2$$

By this assumption, pressure can be calculated to 0.94 atmospheres, or about 95 kPa. In this case, a significant pressure gain is not required to reintroduce flow to atmosphere; it is close enough to ambient pressure that no significantly detrimental effects would occur. However, it would still be useful to reduce flow velocity in order to minimize risk of high-speed winds behind the runway. The team identified two possible diffuser configurations. The first was to reunite all 12 turbine flows in a single rectangular expanding duct, also known as a two-dimensional diffuser. This would then angle upwards and exit the system through another runway opening, similar to the entrance but with no flaps. The other option was to keep all 12 turbine flows separate, each with their own circular expanding duct, or conical diffuser.

To design and compare each diffuser option with commercially available diffusers, the team calculated the required diffuser expansion ratio, represented as the ratio of final cross-sectional area to initial area minus 1. With this ratio, a graph of diffuser stall transition with

relation to area ratio and diffuser length was used. This graph can be seen in Figure 30 below. Each line represents conditions at which stall begins to occur for different diffuser types, based on area ratio and non-dimensional length (diffuser length compared to the dimensions of the duct). The area to the left of each line represents conditions where stall is significant, while the area to the right represents conditions of no appreciable stall. Essentially, the larger area ratio a diffuser has, the longer it must be to avoid stall formation. It is important to note that, based on this graph, conical diffusers are the most “forgiving” in terms of stall formation, while two-dimensional diffusers generally need to be longer in order to avoid stall [31].

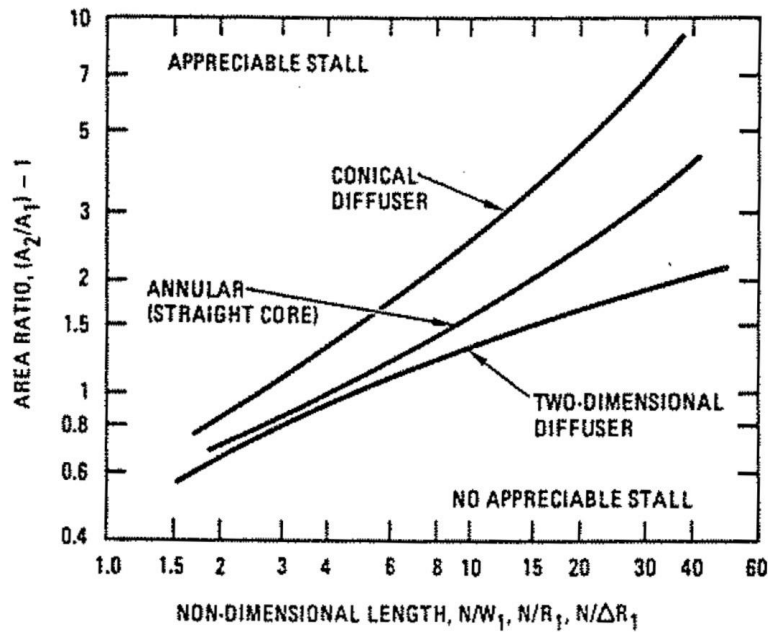


Figure 30: Graph of stall transition based on length and area ratio [31]

The initial cross-sectional area for a two-dimensional diffuser option was calculated with the total duct span of 130.2 feet, and the duct height of 9.85 feet, for an area of 1,282.5 ft². Meanwhile, the initial area of a conical diffuser was simply calculated with the circular turbine diameter (also 9.85 feet), coming out to 76.2 ft². For the purposes of this diffuser design, the team assumed the turbines would reduce flow speed by 50%. This assumption was made to account for the combination duct friction, inefficiencies through the prior system regions, consideration of open-stream traditional wind turbine velocity reduction of 33%, and ducted turbine efficiency of 78% [19, 20]. This means the maximum velocity of flow when it reaches the diffuser is 123 mph. For safety, the maximum allowable flow velocity at the diffuser exit was defined as 50 mph.

$$\rho_1 V_1 A_1 = \rho_2 V_2 A_2$$

$$A_2 = (V_1 A_1) / V_2$$

$$\text{Two-dimensional (one single diffuser): } A_2 = \frac{123 \text{ mph} * 1282.5 \text{ ft}^2}{50 \text{ mph}} = 3155 \text{ ft}^2$$

$$(A_2/A_1) - 1 = 1.460$$

$$\text{Conical (one diffuser of 12): } A_2 = \frac{123 \text{ mph} * 76.2 \text{ ft}^2}{50 \text{ mph}} = 187.5 \text{ ft}^2 \text{ (2250 ft}^2 \text{ for all 12 ducts)}$$

$$(A_2/A_1) - 1 = 1.461$$

While the area ratios for the team's two diffuser configurations are almost identical, Figure 30 shows that a rectangular diffuser with an area ratio of 1.46 would require a non-dimensional length of around 30 to avoid stall, resulting in an ultimate diffuser length of around 300 feet. By comparison, a conical diffuser of the same area ratio would only require a non-dimensional length of 6, leading to a diffuser length of approximately 30 feet [29]. For this reason, the team chose to use 12 distinct conical diffusers. This also had the advantage of allowing the team to choose where each diffuser exit was positioned. A model of the ducting for this portion of the system is shown in Figure 31 below.

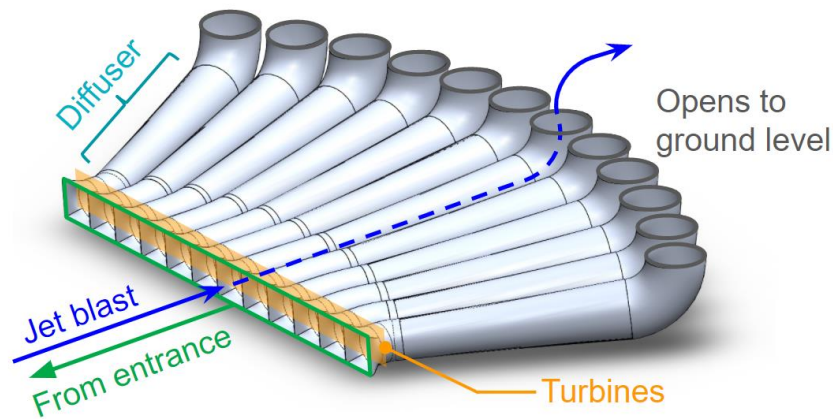


Figure 31: Conical Diffuser Outline

5.0 - Analysis

5.1 - Power Estimates

To model power generation per takeoff, an expression is needed to represent jet blast velocity at the duct entrance over time. Given the inlet velocity, the velocity at the turbine entrance and power generation can be calculated. By integrating power over time, the total energy produced can be solved for.

From Boeing's jet blast data on the 747-400, the graph shown below in Figure 32 was constructed to model the relationship between jet blast velocity relative to distance from the aft of the plane. Based on the plane position and simulated jet blast velocity coordinates, a best fit curve was generated in Excel with an R^2 value of 0.9971, which is suitably accurate. An R^2 value of 1.0 would mean that the fit equation is a perfect approximation for the trend in the data. The best fit curve in this case was a logarithmic equation.

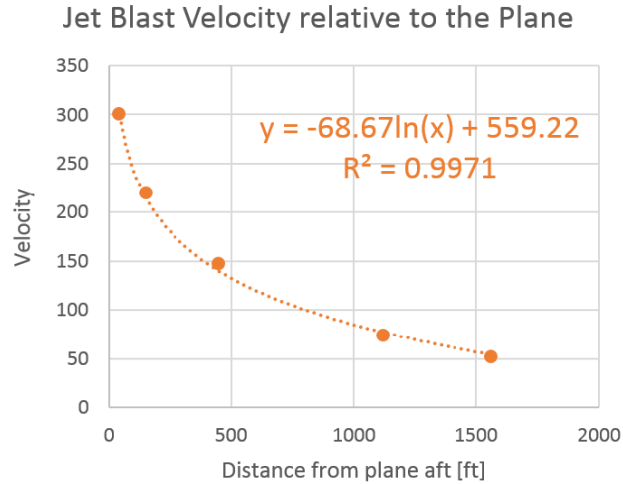


Figure 32: Graph of jet blast velocity relative to the aircraft

Assuming the velocity profiles relative to the plane still hold true for a local coordinate system relative to an aircraft that is accelerating down a runway, then the plane velocity and relative jet blast velocity expressions can be combined and redefined as functions of time to calculate the real jet blast velocity (what an observer standing next to the runway would see). These velocities are shown below in Figure 33.

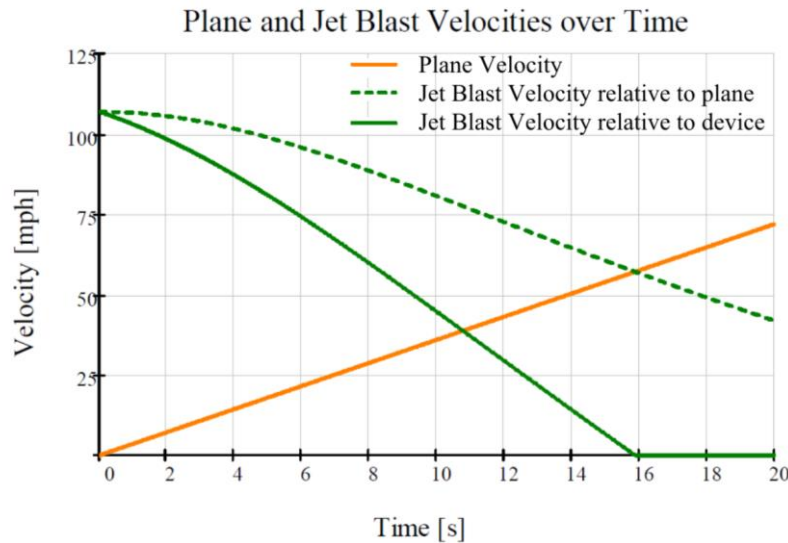


Figure 33: Graph of aircraft and jet blast velocities over time

Now that the jet blast velocity at the inlet has been solved for, velocity at the wind turbines after funneling can also be found, as well as power production and energy generation. Power produced takes into account efficiency, density of the air, total turbine bank area, and inlet-to-turbine area ratio. The general power equation for a wind turbine can be altered to be a function of jet blast velocity, which itself is a function of time. For an efficiency, 75% was chosen based on research efforts in ducted turbine technology discussed in section 2.3.1 - *Wind Energy*. This assumes no energy losses to the walls of the ducting interior.

$$P = 0.5 \cdot C_p \cdot \rho \cdot A_t \cdot V_t^3$$

$$P_{jb(t)} = 0.75 \cdot \rho \cdot A_t \cdot \left[\frac{\left(\frac{A_i \cdot V_{jb(t)}}{A_t} \right) + \left(\frac{A_i \cdot V_{jb(t)}}{A_t} \right) \cdot \frac{1}{3}}{2} \right]^3 \cdot \frac{1}{2}$$

To find energy generated from the power output from the turbines, the power function is simply integrated with respect to time. The graphs below (Figure 34) approximate the power generation and energy generation values and compare them to the typical power and energy generated by a GE 2 MW traditional wind turbine.

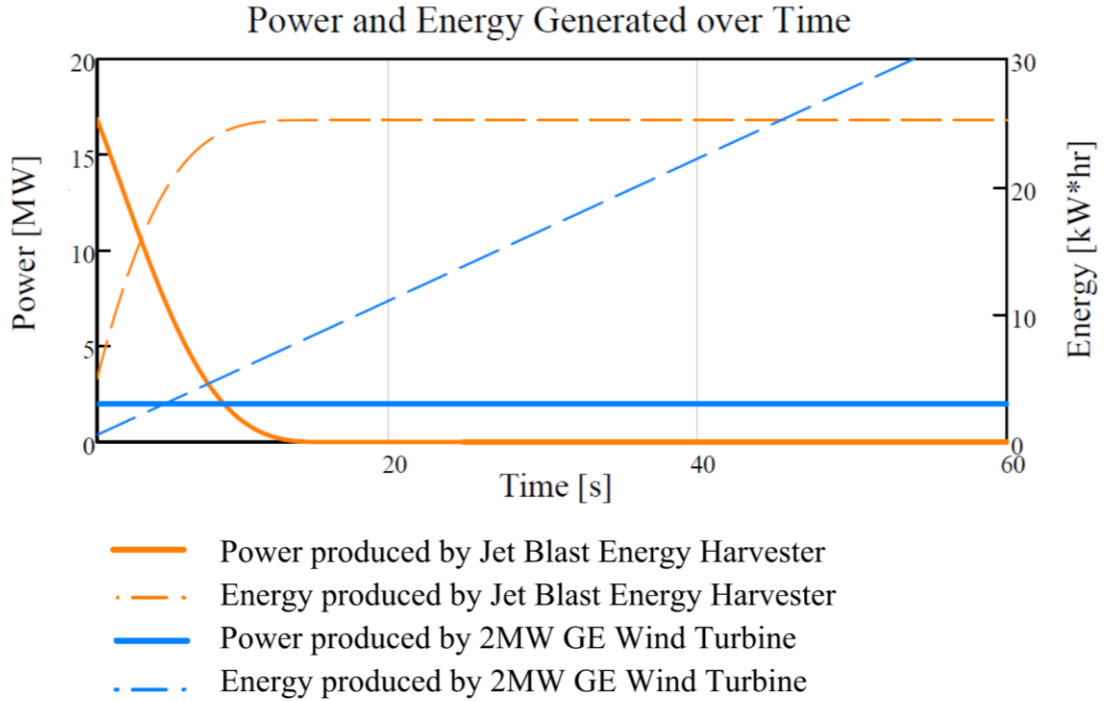


Figure 34: Estimated power and energy generation

As illustrated in the figure, the mechanism proposed in this MQP is estimated to produce as much energy in 15 seconds (from a single jet blast) as a GE 2 MW traditional wind turbine can in 45 seconds (operating at optimum wind speed conditions). According to our model, the energy generated by a single jet blast is calculated to be $8.6 \cdot 10^4$ BTU, or 25.2 kW*hrs.

Based off of Logan International's 2016 – 2017 domestic flight departures and average weather records in the Boston area, the team was able to determine the usable flights over the course of a year [32, 33]. Usable flights were determined based off of a precipitation factor. Once the team had these flights for the course of a year, the annual energy was calculated to be $1.76 \cdot 10^{10}$ BTU. Combined with current renewable energy production at Logan, there was a total energy production of $2.08 \cdot 10^{10}$ BTU [9].

5.2 - Fluids Analysis

To first characterize the flow at the duct entrance, the Reynolds number was calculated. The Reynolds number is a dimensionless parameter defined as a way to characterize the turbulence of a flow.

$$Re = (\rho V D_h) / \mu$$

$$Re = 2.534 * 10^7$$

At conditions before entering the system according to Boeing data, the density of air at sea level (ρ) is 0.0023769 slugs/ft³; average velocity (V) is 100 mph; characteristic length, in this case hydraulic diameter (D_h), is 27.3 feet; and dynamic viscosity (μ) is 3.75 * 10⁻⁷ lbf-s/ft². As the Reynolds number is significantly over laminar conditions of 2300, it can be categorized as turbulent.

Because the simulation run by Boeing uses proprietary software and more specific results are not published beyond Figure 2, the profiles of the simulated velocity were calculated based on a parabolic assumption for velocity. If each plane along the runway was examined, the profiles were assumed to look as in Figure 35. Looking at the top view of Figure 35, the corresponding intersecting points of the orange lines for each profile were taken to be the intercepts of each parabola (Figure 36). The intersection between the manually placed orange vertical lines and blue jet blast profile lines shown in Figure 35 were the vertices of each parabola at different locations. A parabolic equation was defined for each corresponding profile in that plane. To find the velocity components, the angles of each line were approximated. An inlet profile was created to be used within ANSYS Fluent for a 3D model.

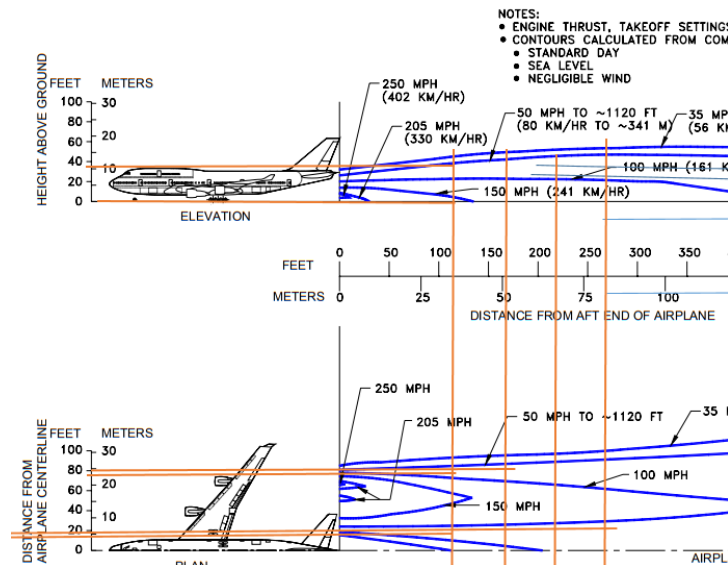


Figure 35: Jet blast velocity derivation [12]

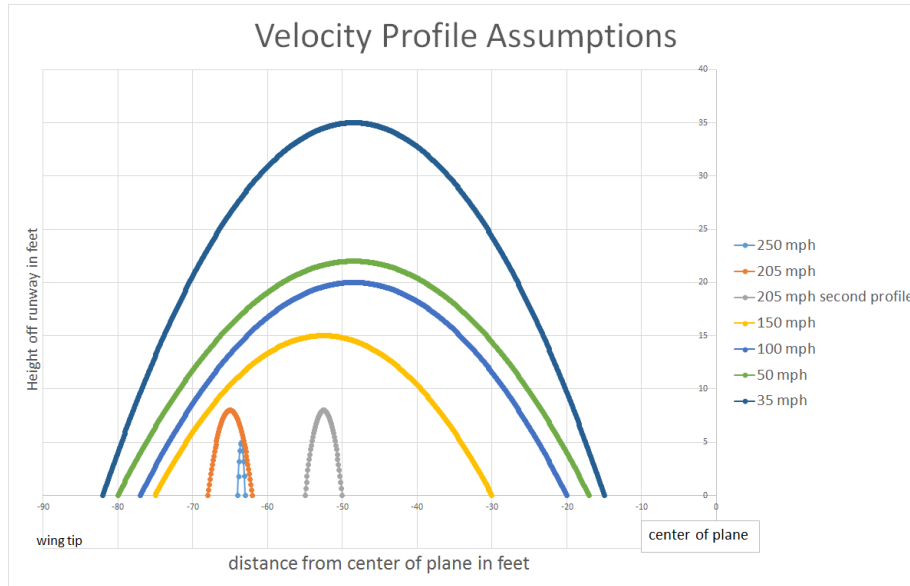


Figure 36: Jet blast velocity parabolic contours

Fluent was used to simulate wind velocity further along the runway than what is shown in the Boeing profiles. A profile generated by the parabolic estimate was input into a 3D steady state model of a traditional runway. At positions along the runway that would be a certain distance from the plane during its takeoff sequence, velocity profiles were exported. This allowed for the accumulation of approximated data for the velocity that the team could use in design estimations. Because the Boeing simulations were based off of the stationary 747, it did not take into account the plane velocity in the opposite direction of the jet blast. To account for this, the following equation was calculated for each set of relative jet blast velocity:

$$\text{Real Velocity} = \text{Relative Jet Blast Velocity} - \text{Plane Velocity}$$

This allowed for the transient model to account for the movement of the plane as discussed in the beginning of section 5.1 - Power Estimates.

The model in ANSYS Fluent utilized slightly simpler geometry to allow for easier calculations. It was assumed for the purposes of Fluent simulation that flow through the duct is turbulent in accordance with the k-epsilon model. The k-epsilon model is one of several turbulence models that allowed much of recent turbulence research to occur. It is based off of the Reynolds-Stress tensor, turbulent transport and pressure diffusion, dissipation, and combining them into a single equation for ϵ , which is the dissipation per unit mass [34]. The Fluent model also utilized enhanced wall treatment. 150-time steps, each 0.1 second, were included in the Fluent model with 20 iterations for each time step. As expected from the 2D steady state simulations, the flow separates from the back face of the flap shortly after the tip (Figure 37). At the time step shown in Figure 37, the speed of the flow goes from approximately 55 mph at the flap inlet to 97 mph at the turbine inlet. The flow along the forward-facing part of the flap seems to create a high pressure bubble, which had also been represented in the 2D steady-state model (see Figure 38). This essentially reduced the effective flow intake area, reducing funneling and approximated velocity at the turbine.

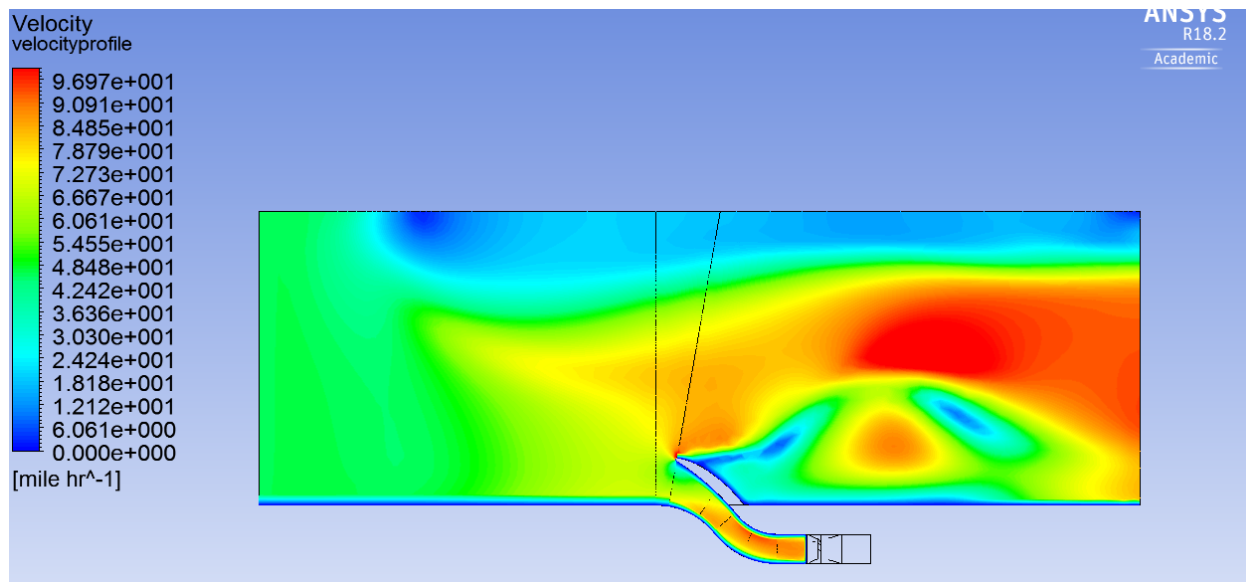


Figure 37: ANSYS Fluent transient velocity model

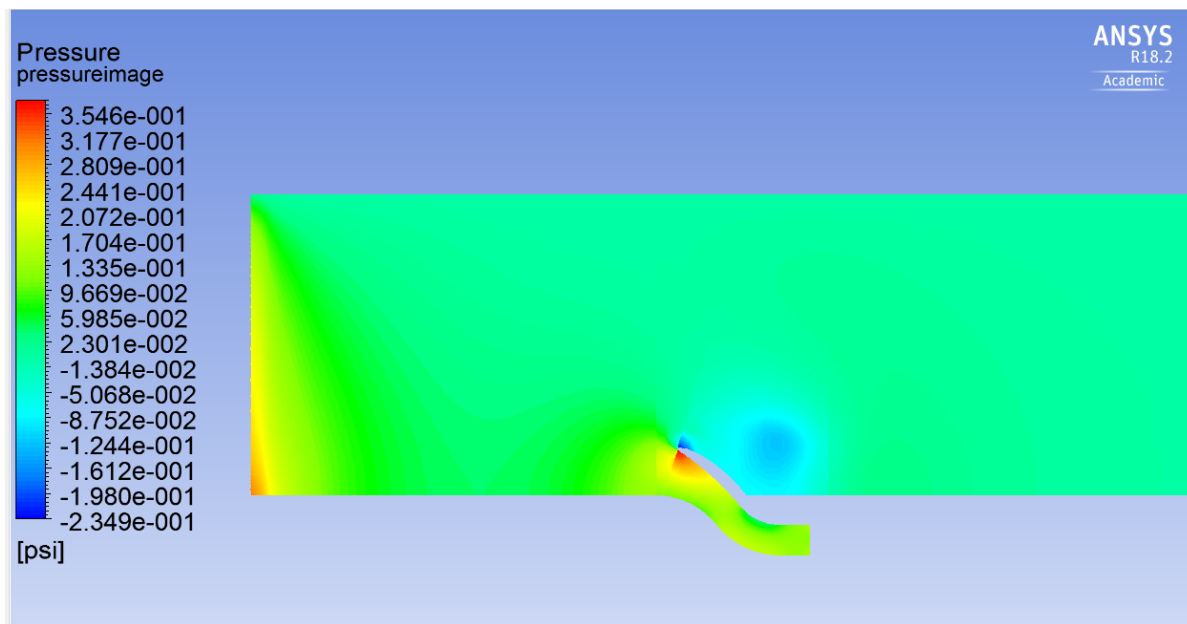


Figure 38: ANSYS Fluent transient pressure model

To characterize the simulated flow, the average speed of the velocity was taken at the entrance at the flap and the entrance at the turbine over multiple time steps. Figure 39 below shows velocity of air through the inlet at the flap. The flow separation occurs near the top of the flap intake, which can be seen in the simulation with the difference in velocity drop-off towards the top of the intake versus the bottom. This is particularly noticeable in the area where the contour of the air speed changes drastically from green to light blue near the top of the flap, indicating the formation of a vortex.

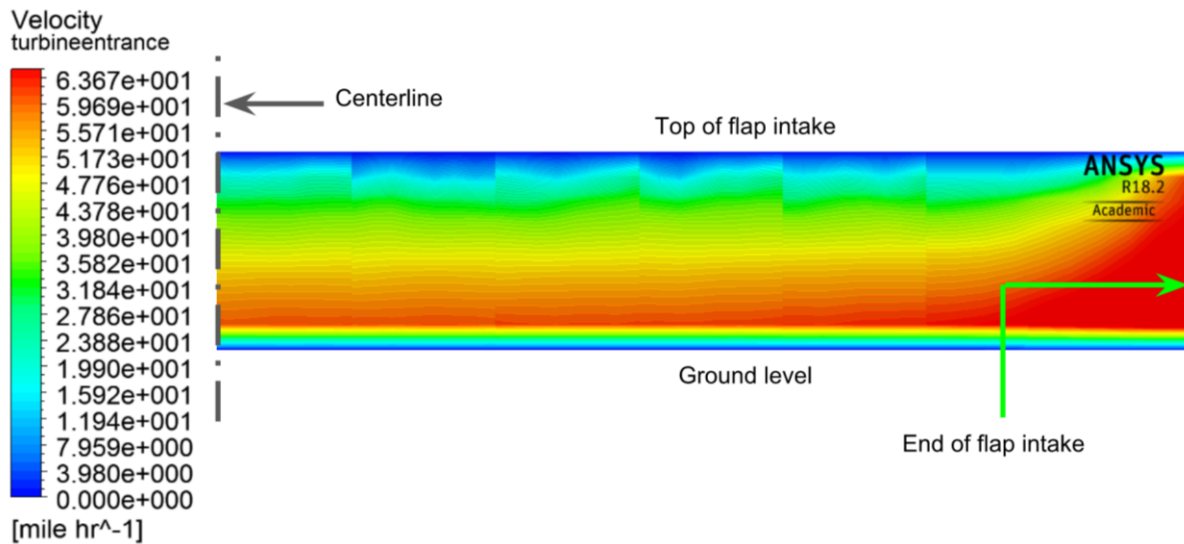


Figure 39: ANSYS velocity profile at flap intake (time = 2s)

The velocity at the turbine was also calculated based on the inlet speeds and Venturi relation. Figure 40 shows the difference between the calculated and simulated velocities at the turbine, based on the same inlet velocity. The two turbine velocity approximations had similar decreasing rates, the differences showcasing the loss due to efficiency.

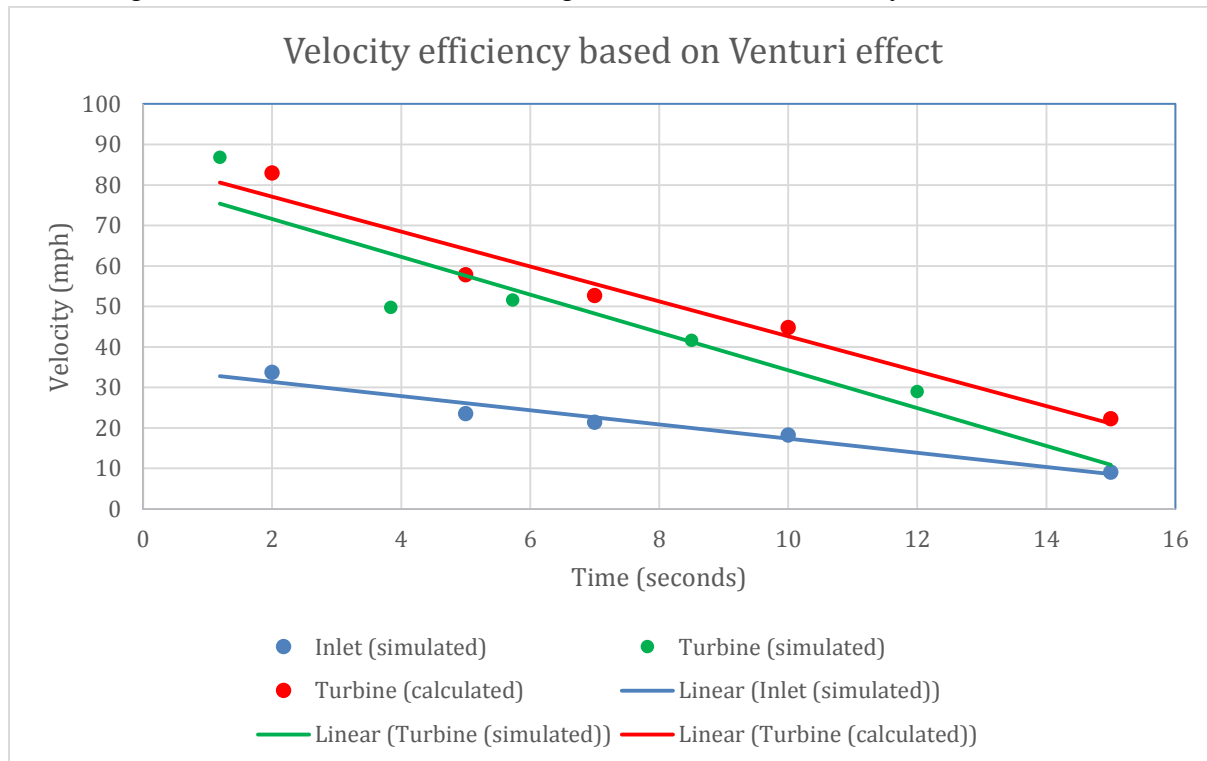


Figure 40: Velocity efficiency based on Venturi effect

According to the Venturi equation, the product of velocity and cross-sectional area must remain constant for any closed incompressible flow system. By knowing the velocity at both profiles, the area at the turbines, and the width of the inlet, the effective height of the flow entering the inlet can be calculated. This is illustrated by the plot in Figure 41.

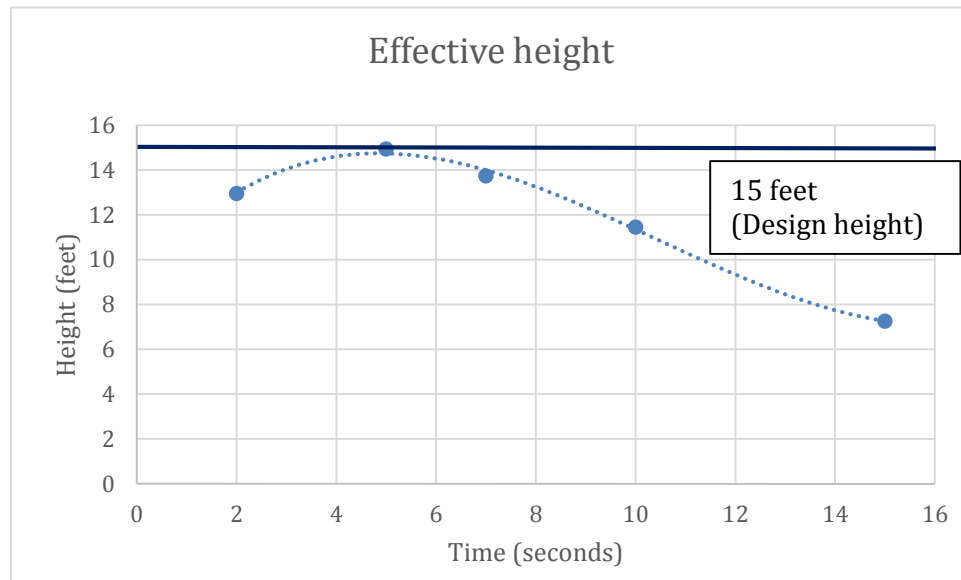


Figure 41: Effective height over time

As time increases in the cycle, the velocity also decreases, making the flap intake less efficient. How efficient the intake is at diverting flow into the duct system can be represented by dividing the effective heights into the design height of 15 feet. Figure 42 shows how sensitive the capture efficiency of the system is for different inlet speeds, with only ~50% efficiency at ~9 mph, increasing to 99% efficiency at ~24 mph. At speeds past ~24 mph, a decrease in capture efficiency occurs. The team theorizes that this is due to the high-speed winds promoting more turbulence, vortex formation, and irreversible losses. This capture efficiency would cause different power production compared to theorized values presented in section 5.1 – *Power Estimates*, as calculations assumed 100% capture efficiency.

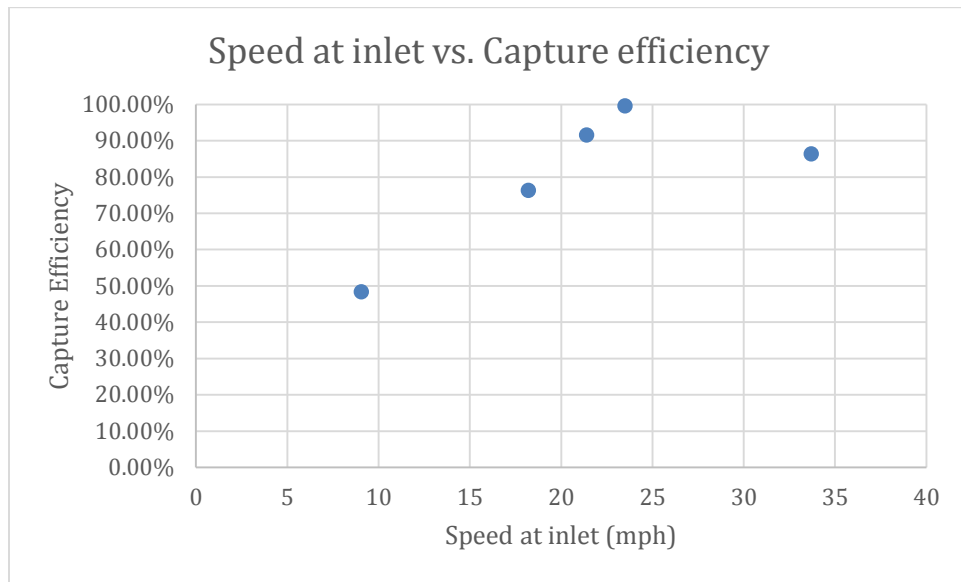


Figure 42: Speed at inlet versus capture efficiency

To analyze the diffuser design, a new model had to be created accounting for the reduction in velocity after the flow travels through the turbine. The profile of the turbine exit was exported and then modified to reduce the velocity by 50% throughout each time step. This value was chosen over the optimum 33% of velocity to be used as a safety factor. The new model had a cut section in the duct (see Figure 43). This was to allow for an outlet to be placed on the turbine side and an inlet to be placed on the diffuser side. The modified profile was then applied to the diffuser inlet boundary condition, so the team could analyze the flow through the diffuser and exiting the diffuser, mixing with the flow over the top of the flap and along the runway. Figure 44 shows the resulting model including the diffuser. The exit flow reconnects with the flow past the flap and continues along the runway.

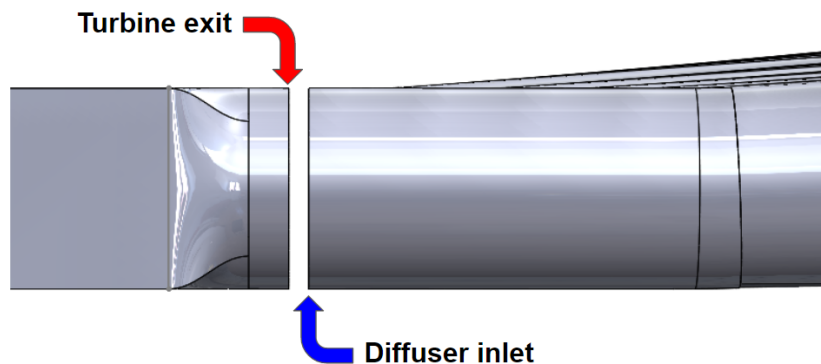


Figure 43: Transient diffuser set up

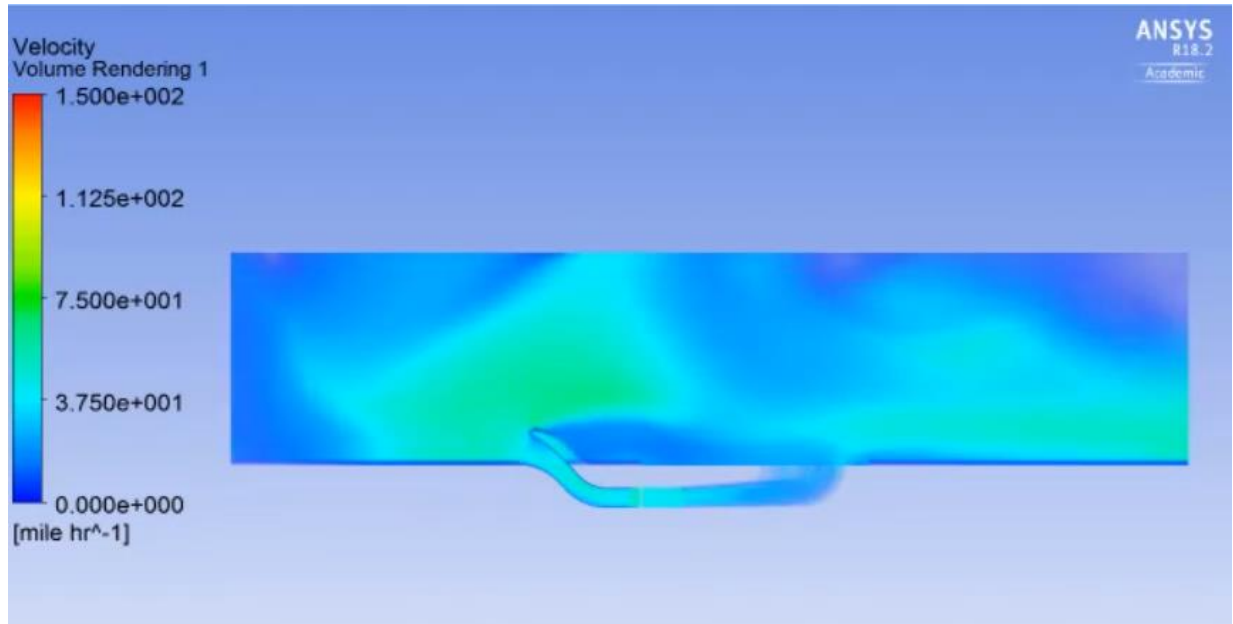


Figure 44: ANSYS Fluent transient model, full system

The flow within the diffuser noticeably decreased in velocity before exiting above ground. The following images show the results from ten seconds into the take-off sequence. The velocity near the beginning of the diffuser is approximately 50 mph (see Figure 45). By the time that the flow exits the diffuser on the face of the runway, its speed is around 30 mph, except for the diffuser furthest away from the center of the plane, which shows the least amount of diffusion (see Figure 46). At fifteen seconds (the end of the take-off sequence), the flow at the diffuser exit is 15 mph.

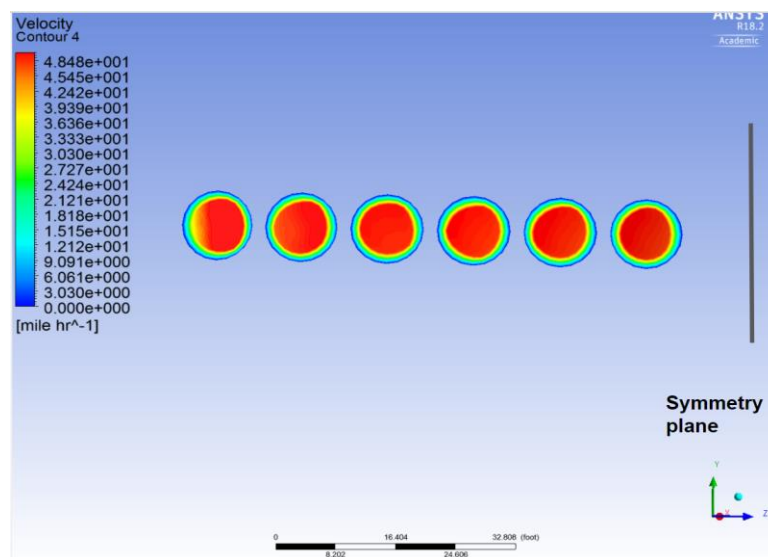


Figure 45: ANSYS Fluent diffuser inlet

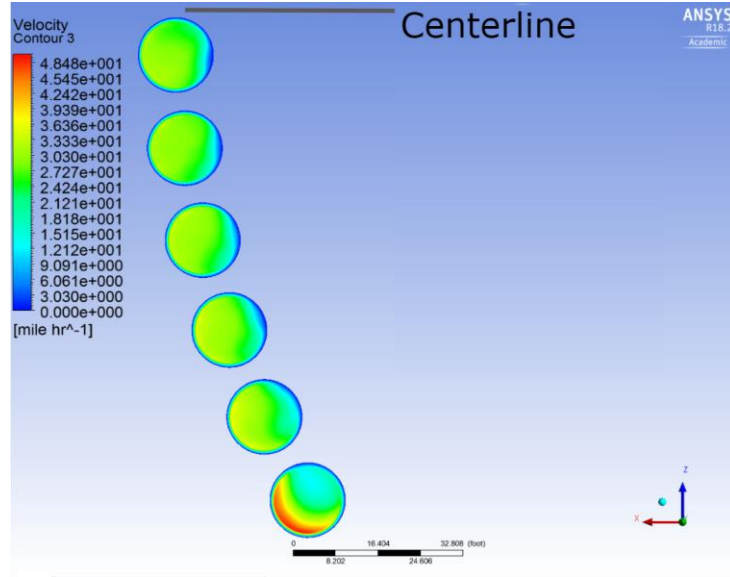


Figure 46: ANSYS Fluent diffuser outlet

5.3 - Aerodynamic Analysis

To properly estimate the forces encountered by each primary flap, the team decided to treat the flap as an airfoil, like that of an airplane. However, this could not be done directly by physical testing due to the magnitude of the Reynolds number. As explained in section 5.2 - *Fluids Analysis*, Reynolds number is a way to quantify flow conditions. The accuracy of scale aerodynamic testing is primarily dependent on similarity of flow; if the Reynolds number of an ideal full-scale case is the same as the Reynolds number of a scaled test with the same geometry, the lift and drag coefficients from the scaled test can be treated as accurate. Air density and dynamic viscosity will be the same for both full-scale and test case. Therefore, Reynolds similarity reduces to only characteristic length (defined as chord length, which is the front-to-back length of an airfoil) and velocity:

$$\begin{aligned}
 Re_{full} &= Re_{scale} \\
 (\rho VL)/\mu &= (\rho VL)/\mu \\
 VL &= VL
 \end{aligned}$$

This relation means that as size decreases for the scale model, velocity must increase proportionally. The size of WPI's wind tunnel dictated a chord length of 5.35 inches, which is 1/74 the full-scale flap's chord length of approximately 33 feet. However, the wind tunnel's maximum velocity was 100 mph, equal to the initial jet blast for the full scale system. Because

physical scale between the potential system and prototype changes but wind speed does not, Reynolds similarity was impossible to achieve for physical testing.

To compensate for the lack of exact physical testing, two different analytical methods were identified to theoretically calculate the aerodynamic forces. The simplest calculation was to model the flap as a flat rectangular plate which experiences forces solely due to momentum transfer, as shown in the calculations below (see Figures 47 and 48).

$$F_N = \frac{\Delta p}{\Delta t} = \frac{p_i - p_f}{\Delta t} = \frac{m_i * V_i - m_f * V_f}{\Delta t} = \left(\frac{\Delta m}{\Delta t} \right) * (V_i - V_f) = \dot{m} * (V_i - V_f)$$

Assuming no energy loss in fluid movement, where p is momentum, m is mass, and V is velocity, and \dot{m} is mass flow rate.

$$V_i = |V| * \cos(90 \text{ deg} - \theta) = |V| * \sin(\theta)$$

$$V_f = 0$$

$$F_N = \dot{m} * (|V| * \sin(\theta) - 0)$$

$$\dot{m} = \rho * V * A_{jet}$$

Where ρ is 0.076 lbm/ft³, V is 100 mph, and A_{jet} is 225 ft². Solving for \dot{m} results in 78.4 slugs/s.

$$F_N(\theta) = \dot{m} * V * \sin(\theta)$$

$$F_X(\theta) = F_N(\theta) * \cos(90 \text{ deg} - \theta)$$

$$F_Y(\theta) = F_N(\theta) * \sin(90 \text{ deg} - \theta)$$

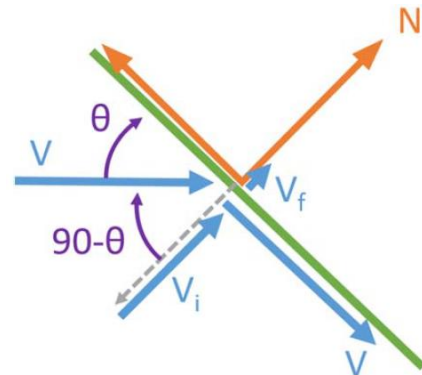


Figure 47: Flat plate assumption flow redirection

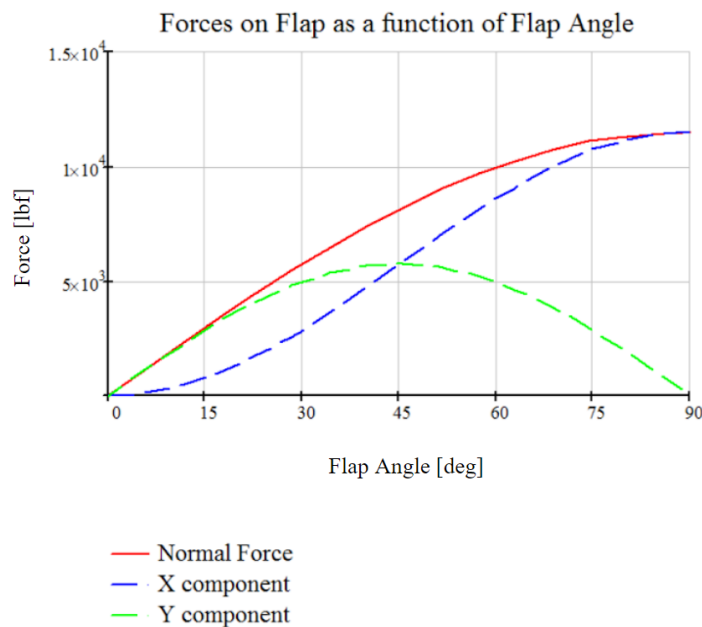


Figure 48: Aerodynamic modeling with the flat plate assumption

Based on this estimation, the vertical and horizontal components of the force on a single 15-foot section of primary flap at 45° would be 5,751 lbf each, for a resultant force of 8,130 lbf normal to the plate.

In aerodynamic force analysis of airfoils, lift and drag are defined as the vertical and horizontal components of aerodynamic forces, predominantly dictated by air pressure differentials and viscous effects. If the vertical and horizontal forces of a flat plate estimation are taken as analogous to aerodynamic lift and drag respectively, there is no strong correlation to typical lift and drag curves. For example, lift usually peaks somewhere between 20-30°, while for a flat plate estimation the vertical force peaks at 45°, as shown in Figure 48 above. This is because, as mentioned, the flat plate assumption only pays attention to momentum-based force. For this reason, the team decided to use a more reliable testing method to inform their design.

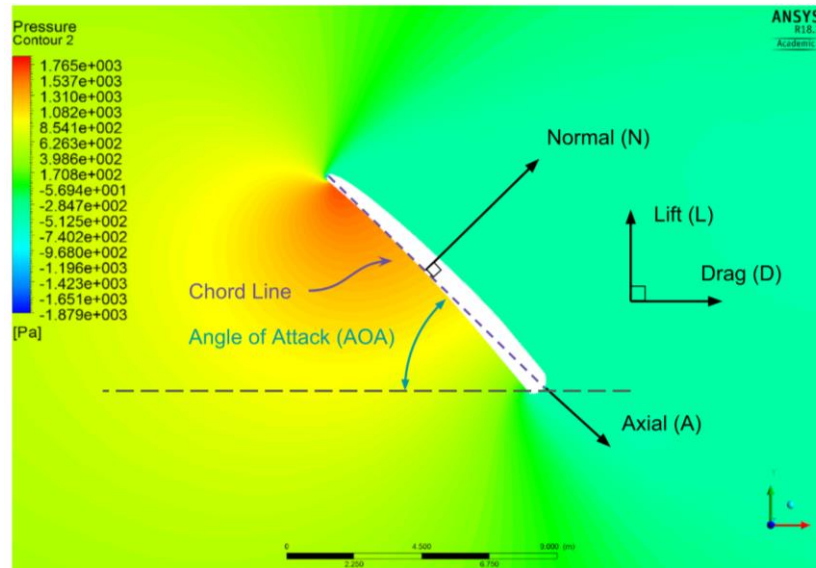


Figure 49: ANSYS Fluent pressure contours around flap

The team utilized ANSYS Fluent to simulate forces on the flap. Since the purpose of these simulations was to estimate the maximum forces encountered, a constant wind speed of 100 mph was used. A two-dimensional model was set up for each test case (one for the full-scale system and another to verify the wind tunnel tests) with a flap angle of zero. For each angle of attack, the angle of flow was changed, and the normal and axial force coefficient outputs from Fluent were converted into lift and drag coefficients using the following equations:

$$C_L = C_N * \cos(\alpha) - C_A * \sin(\alpha)$$

$$C_D = C_N * \sin(\alpha) + C_A * \cos(\alpha)$$

These coefficients were then used to find overall forces with:

$$F = \frac{1}{2} * C_F * \rho * V^2 * S$$

Where S is the planform area of the “wing”, equal to the chord length times the wingspan. Chord length is the tip-to-tip length of an airfoil, which for our case was taken to be the distance from the midpoints of the top and bottom curves as seen in Figure 49 above. For the case of the full-sized flap, chord length was taken to be 32.96 feet, and the wingspan used was the width of one flap “section,” 15 feet. The scale model had a chord length of 5.35 inches and a wingspan of 7.2 inches. Lift and drag were taken in the traditional aerodynamic sense; that is, they were defined as the resultant force on the flap perpendicular and parallel to free flow respectively. Since ANSYS Fluent accounts for pressure and viscous forces, these results are should theoretically be closely comparable to experimental lift and drag forces.

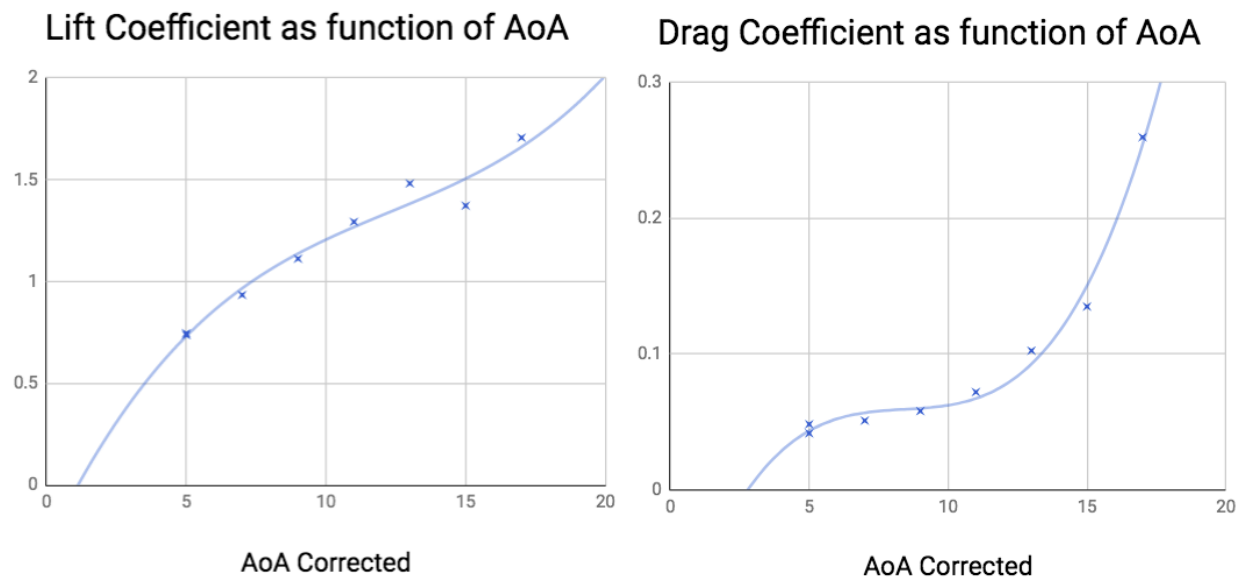


Figure 50: Lift and drag coefficient for 1/74 scale wind tunnel ANSYS simulation

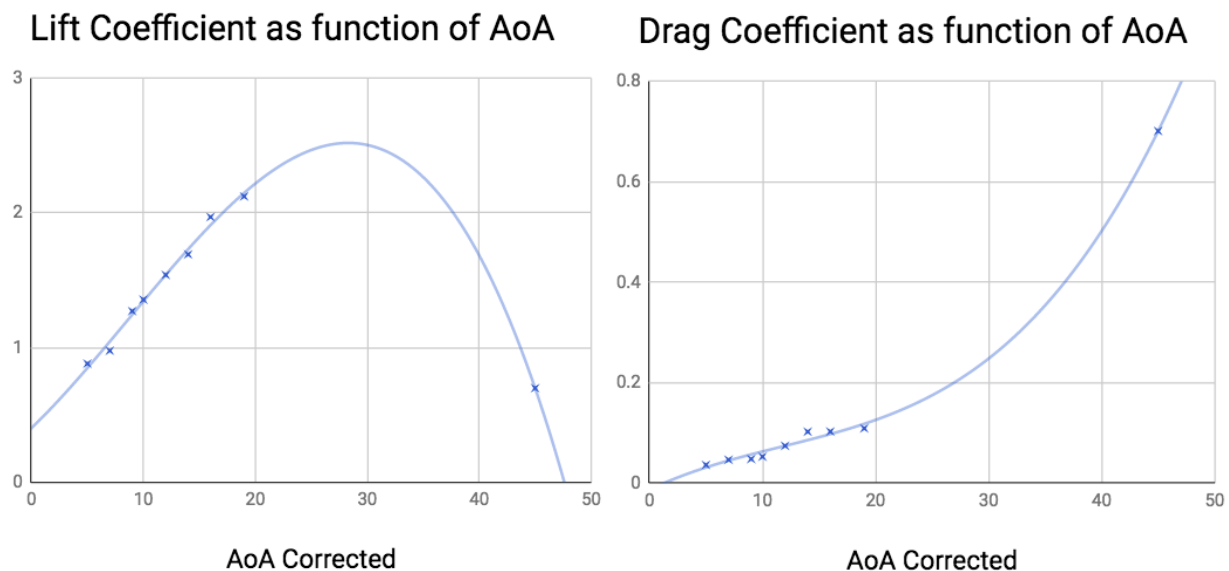


Figure 51: Lift and drag coefficient curves for full-scale flap ANSYS simulation

As predicted, Fluent was generally unable to reach a solution for cases past the point of flow separation around an angle of attack of 20° . Interestingly, the simulations are also relatively stable at 45° . The coefficients Fluent provided seem sufficiently continuous, and make sense when compared to lift and drag curves of more conventional airfoils. In aerodynamic theory, lift force is at a maximum at the stall angle, which is usually 20 - 25° . For this reason, the simulated lift force corresponding to 19° , the highest data point calculated for the full-scale system, was used as the maximum lift force at 45° (the angle at which the flap is in use) for structural analysis. Drag, however, always increases up to 90° , and has no theoretical way to be calculated. The drag force calculated by Fluent at 45° was still used, as the team judged it was within reason. The lift and drag used for structural estimation were 19,097 lbf (from 19°) and 9,752 (from 45°) lbf respectively, for a resultant force of 21,443 lbf at 63° from horizontal. This force is about 2.6 times higher than what was calculated via the flat plate assumption. This is to be expected since the flat plate assumption is not a true aerodynamic model.

5.4 - Structural Analysis

5.4.1 - Mechanism Analysis

Structural evaluation of the system is most critical at the inlet region, where forces from the jet blast and long unsupported lengths of the flap section have the potential to cause large stresses and deflections. Structural analysis was performed both through manual calculations and software simulation to maximize confidence in resulting stresses. Looking at a side view of the mechanism in the deployed position, the system can be approximated as a double-rocker 4-bar linkage with ground joints A and G (forming ground link L_0), the primary flap making up link AD, the secondary flap making up link GE, the connecting cable (with length L_C), making up coupler link DE, and the hydraulic piston acting as the actuator on link AD. Links and associated angles are overlaid over a model of the actual system in Figure 52 below.

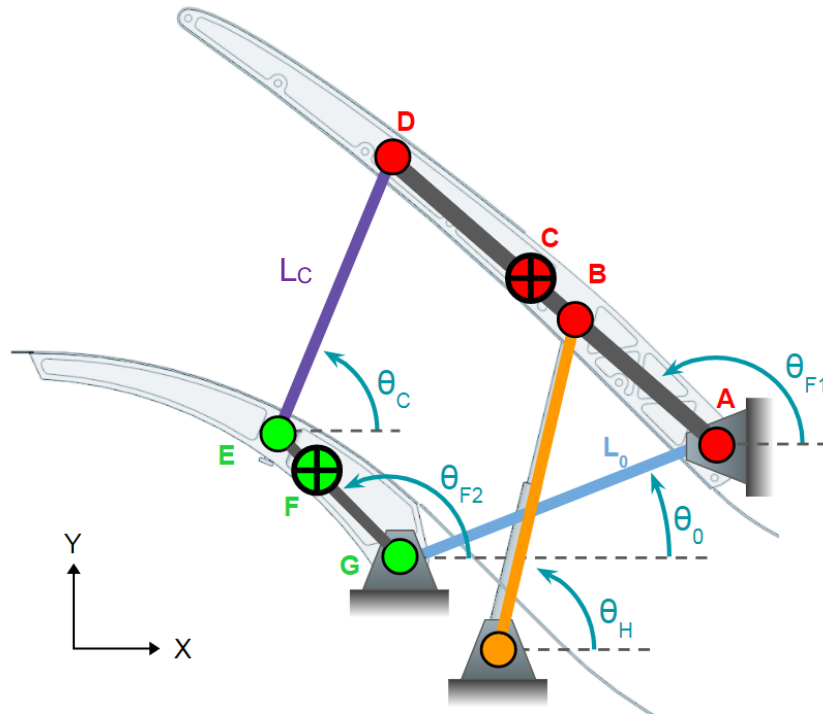


Figure 52: Mechanism 4-bar approximation and geometry

Each rib is approximated as a beam of constant cross section which experiences loads only in the X-Y plane coincident with the ribs. In reality, forces from jet blast on the flap surface between rib supports is going to create a moment with an axis collinear with the length of the rib, causing the ribs on either side of a flap section to twist inwards. For the sake of keeping hand calculations for stress analysis simple, it will be assumed that torquing from jet blast is negligible, and this will instead be left to the SolidWorks simulation. On the primary flap, there are 3 known forces (lift, drag, and weight) and 4 unknowns (ground reaction X & Y, hydraulic lift force, cable tension). There are two different cases with which we must evaluate stresses: when lift and drag are zero (no jet blast), and when lift and drag are non-zero (jet blast hits the flap at full speed). On the secondary flap, there is only 1 known force (weight) and 2 unknowns specific to the secondary flap (ground reaction X & Y). Numerical values for weights and lengths are retrieved from SolidWorks unless mentioned otherwise. All of the forces, associated angles, and points of interest are illustrated in Figure 53 below.

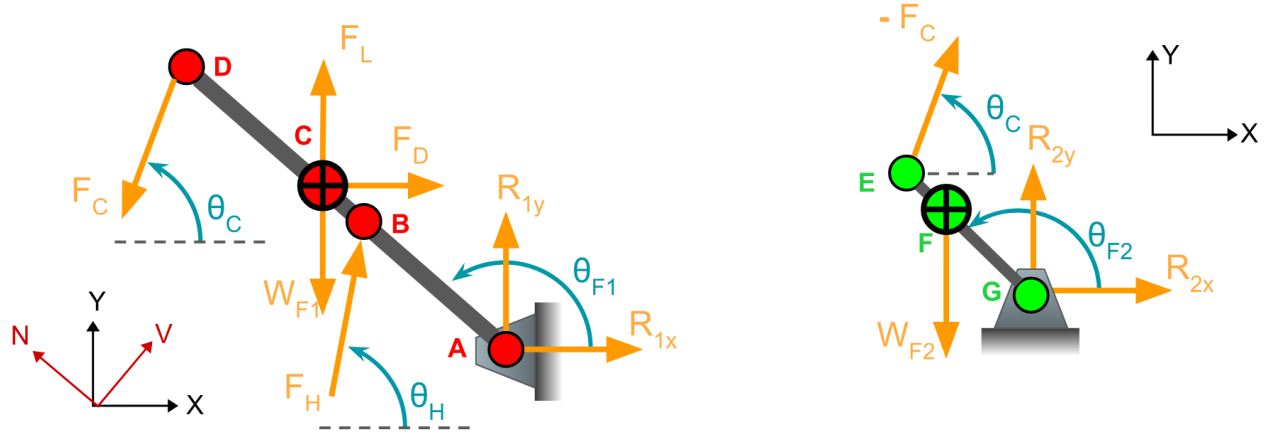


Figure 53: Free Body Diagrams of the primary flap (left) and secondary flap (right)

Position Analysis

At the beginning of the setup of this 4-bar system, only the link lengths, angle of the ground link, and angle of the primary flap in its uppermost position are known. This leaves two unknowns: the angle of the cable and of the secondary flap. Because a 4-bar forms a closed profile, the vector sum of 2 link lengths must equal the vector sum of the other 2 links.

$$L_C * \cos(\theta_C) + -r_{AD} * \cos(\theta_{F1}) = L_0 * \cos(\theta_0) + -r_{GE} * \cos(\theta_{F2})$$

$$L_C * \sin(\theta_C) + r_{GE} * \sin(\theta_{F2}) = L_0 * \sin(\theta_0) + r_{AD} * \sin(\theta_{F1})$$

Where L_C is the length of the cable (13.94 ft), θ_C is the angle of the cable (unknown), r_{AD} is the entire length of the primary flap (19.79 ft), θ_{F1} is the angle of the primary flap (138.03 degrees), θ_0 is the angle of the imaginary link connecting the primary flap to the secondary flap to the horizontal (20.35 degrees), r_{GE} is the total radius of the secondary flap (11.39 ft), and θ_{F2} is angle of the secondary flap (unknown).

Solving for θ_C and θ_{F2} produces values of 53.6 degrees and 140.1 degrees respectively.

Solving for Unknown Forces

For the mechanism to remain static, forces and moments must sum to zero. Applying this static case to the system creates 6 equations of equilibrium which can be related to the forces on the two flaps. There are 6 unknown values for forces (cable tension, hydraulic lift force, and 4 ground reactions in X and Y) which can now be solved for.

Sum of the forces in the Y direction

$$0 = W_{F2} + (-F_c * \sin(\theta_c)) + R_{2Y}$$

Sum of the forces in the X direction

$$0 = (-F_c * \cos(\theta_c)) + R_{2X}$$

Sum of the moments in the Z direction

$$0 = |W_{F2}| * \sin(\theta_{F2} - 90 \text{ deg}) * r_{GF} + (-|F_c| * \sin(\theta_{F2} - \theta_c) * r_{GE})$$

Where W_{F2} is the weight of the secondary flap (7,227 lbf), F_c is the tension of the cable (unknown), R_{2Y} is the reaction force of the secondary flap in the Y direction (unknown), R_{2X} is the reaction force of the secondary flap in the X direction (unknown), and r_{GF} is the radius from the hinge of the secondary flap to the center of gravity (7.75 ft).

Solving for R_{2X} , R_{2Y} , and F_c yields 4,614 lbf, -2,859 lbf, and 5,195 lbf respectively. This tension value is used for cable sizing as discussed in section 4.5 - *Closing Mechanism*.

Applying the same method for the primary flap, we can use the fact that two of the three remaining unknowns are both at the hinge, so by solving for moments we can calculate the force that is required to be provided by the hydraulic immediately.

Sum of the Moments in the Z direction

$$0 = (|F_c| * \sin(\theta_{F1} - \theta_c) * r_{AD}) + (|W_{F1}| * \sin(\theta_{F1} - 90 \text{ deg}) * r_{AC}) + (-|F_L| * \sin(\theta_{F1} - 90 \text{ deg}) * r_{AC}) + (-|F_D| * \cos(\theta_{F1} - 90 \text{ deg}) * r_{AC}) + (-|F_H| * \sin(\theta_{F1} - \theta_H) * r_{AB})$$

Where r_{AC} is the length of the primary flap from the hinge to the center of gravity (13.3 ft), F_L is the force due to lift (19,097 lbf), F_D is the force due to drag (9,753), F_H is the force of the hydraulics (unknown), θ_H is the angle of the hydraulics (iterated to 70 degrees), and r_{AB} is the point where the hydraulics are connected to the primary flap (8.73 feet).

Lift and drag forces were derived from section 5.3 - *Aerodynamic Analysis*. Solving for F_H with and without jet blast produces values of 19,240 lbf and 36,550 lbf respectively. The angle of the hydraulic cylinder was iterated from 30 degrees to 80 degrees and resulting hydraulic force and reaction forces at the hinge were plotted (Figure 54). Hydraulic force reaches a global minimum at ~50 degrees, while total reaction magnitude at the hinge reaches a global minimum at ~70 degrees. Comparing change in values from 50 degrees to 70 degrees, reaction forces are decreased by 26% while hydraulic force only raises by 8%, making 70 degrees the optimum angle to have the piston support the primary flap.

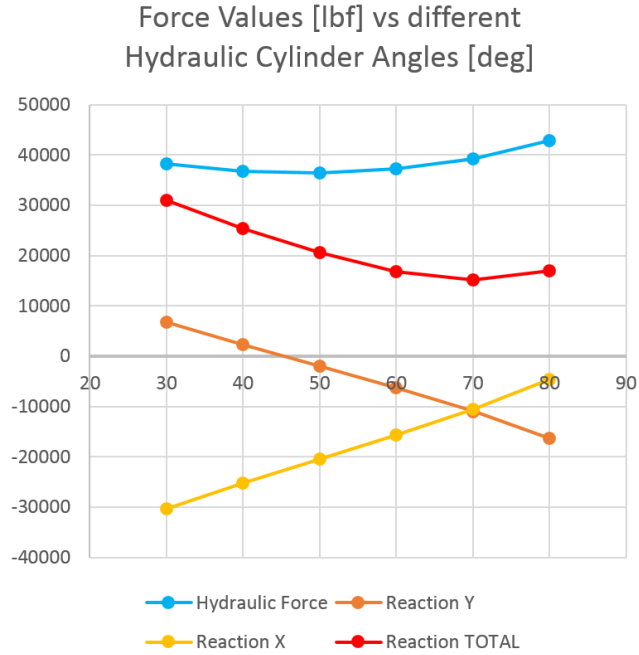


Figure 54: Values of unknown forces as function of hydraulic cylinder angle

Sum of the forces in the Y direction:

$$0 = (F_C * \sin(\theta_C)) + (F_H * \sin(\theta_H)) + (R_{1Y}) + (W_{F1}) + F_L$$

Sum of the forces in the X direction:

$$0 = (F_C * \cos(\theta_C)) + (F_H * \cos(\theta_H)) + (R_{1X}) + F_D$$

Where R_{1Y} is the reaction force in the y direction (unknown) and R_{1X} is the reaction force in the X direction (unknown).

Solving for R_{1X} and R_{1Y} with jet blast loading yields -8,601 lbf and -3,370 lbf respectively, and without jet blast yields -9,643 lbf and -10,080 lbf respectively.

Stress Analysis

Now that forces are solved for, equations for shear and axial load across the lengths of the primary flap rib in the V and N directions respectively may be formed (see Figure 53 above for coordinate system illustration). Only the primary flap is considered as it is subjected to the most intense loading. Singularity equations are used, as they allow for the rapid construction of load, bending, and deformation equations across beams as functions of length traversed. The resulting shear, neutral-axis normal force, moment, and deformation diagrams are illustrated in Figure 55 below as functions of distance from the hinge. This is done up to ~20 feet for the shear and bending because there is no force past the cable pin, and to the flap tip for deflection. It is calculated that the flap rib will deflect no more than 3.2 inches when it is simply holding its own weight. This deflection will decrease when the flap is subjected to jet blast.

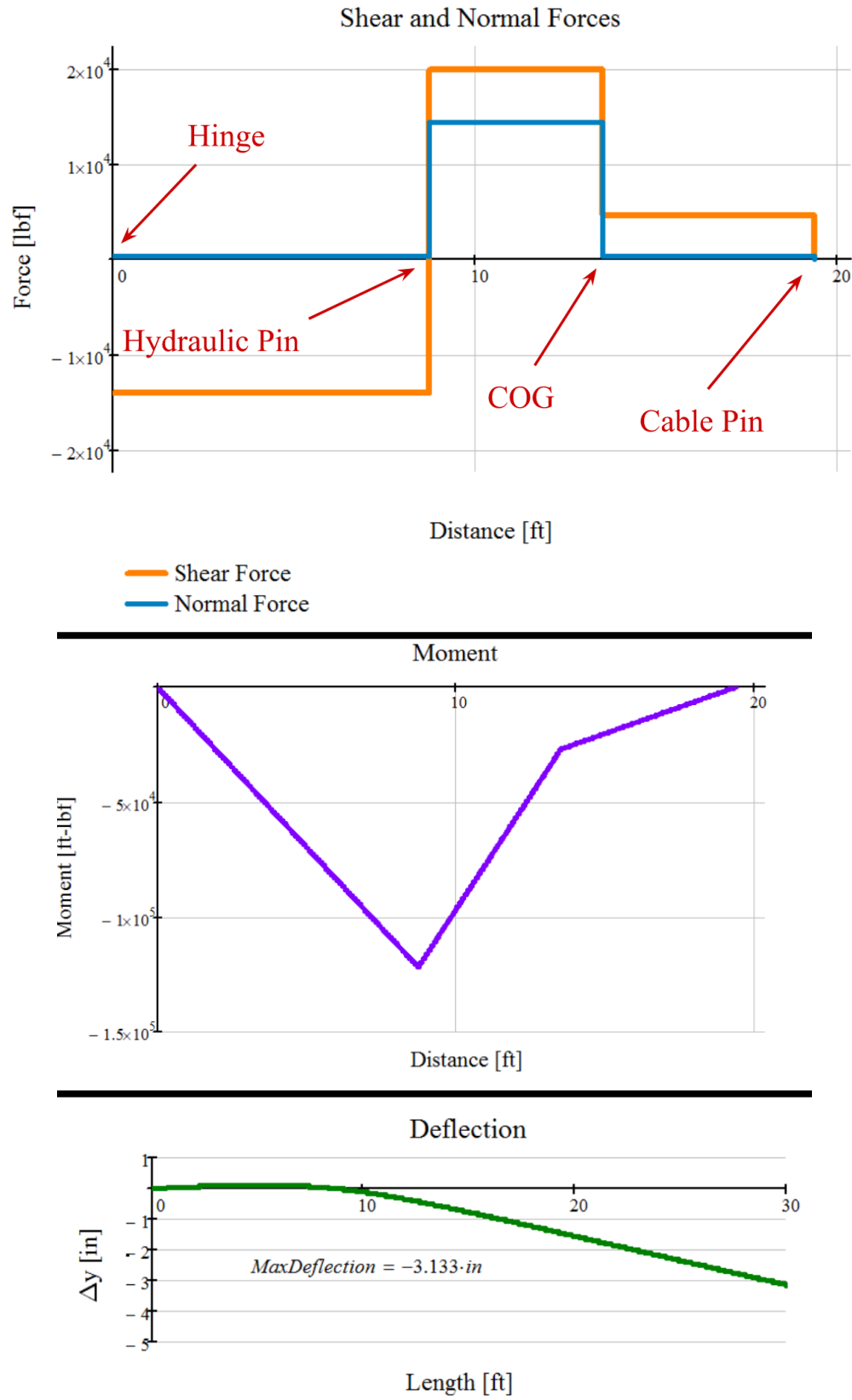


Figure 55: Shear force, normal force, moment, and deflection across length of the primary flap (no jet blast)

There are two regions in which the cross section of the rib is most vulnerable to stresses. These areas and the correlating stress cubes are depicted in Figure 56 below.

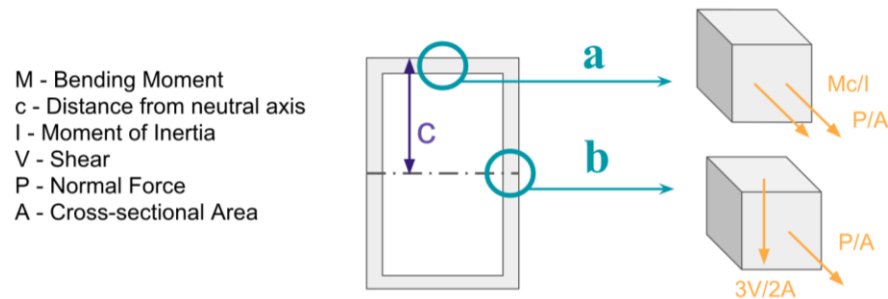


Figure 56: Cross section of rib and relevant stress cubes

The stresses at play in section “a” are bending and axial pressure, while the stresses in section “b” about the neutral axis are axial pressure and shear. Solving for principal stresses in each section and plotting the largest values as functions of distance from the hinge results in the below plot (Figure 57). The largest stress is experienced at the hydraulic pin connection with a value of 2.1 ksi, which is lower than the yield strength of stainless steel (39.9 ksi) by a factor of 18.6 (also known as the safety factor). This is also under the endurance limit of the material, which means the mechanism should have an infinite fatigue life.

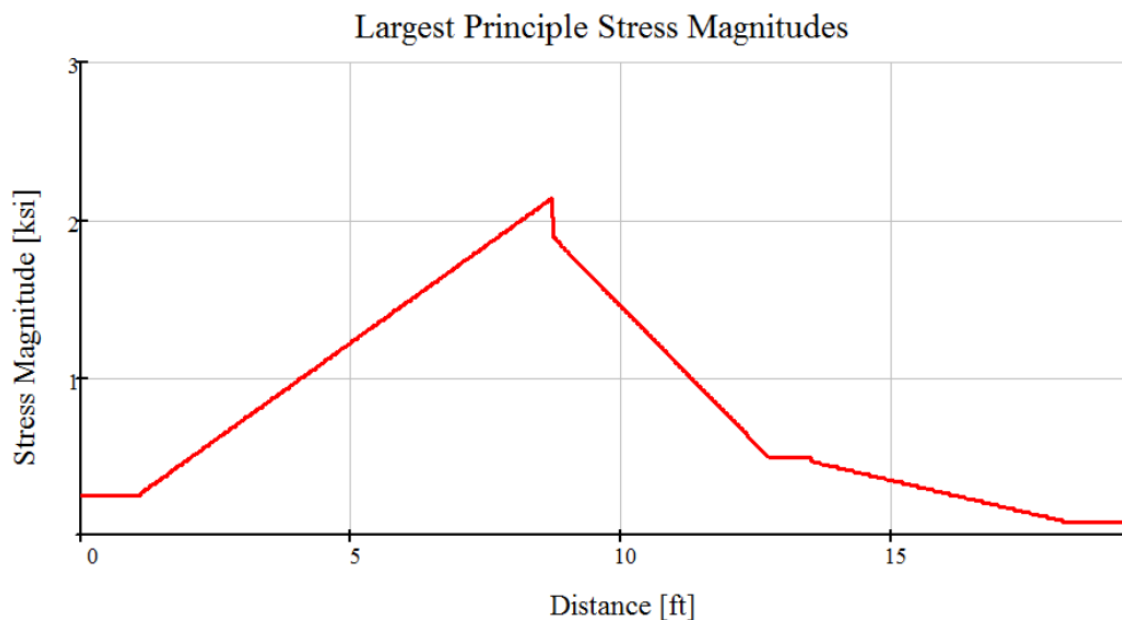


Figure 57: Magnitude of the largest stress at any given length across the rib

Finite Element Analysis

The second approach for resolving resultant forces and stresses was accomplished by setting up a static study of a CAD model of the mechanism using SolidWorks finite element analysis (FEA). The model is geometrically and physically reflective of a prospective system, so distributed loads like weight and jet blast pressure and their effects on the system are characterized more realistically. Boundary conditions were set for all parts to properly reflect component interactions. This was done by “fixing” the faces of the hinges that would attach to adjacent support structures (4 flap hinges and 2 hydraulic hinges), adding “pin” connections between all joints (with all pins being in double-shear), and by “bonding” components that are rigidly attached to one another (primary flap surface and ribs). There are again two cases which are important to study: Case 1 refers to the scenario for which the mechanism structure is simply supporting its own weight, and Case 2 refers to the scenario for which jet blast is hitting the primary flap at full force. Gravity was enabled for both cases, and jet blast lift and drag were applied to just Case 2 acting across the entire frontal surface of the primary flap. Finally, meshing controls were applied to optimize result quality. Figure 58 below presents an annotated view of the FEA setup.

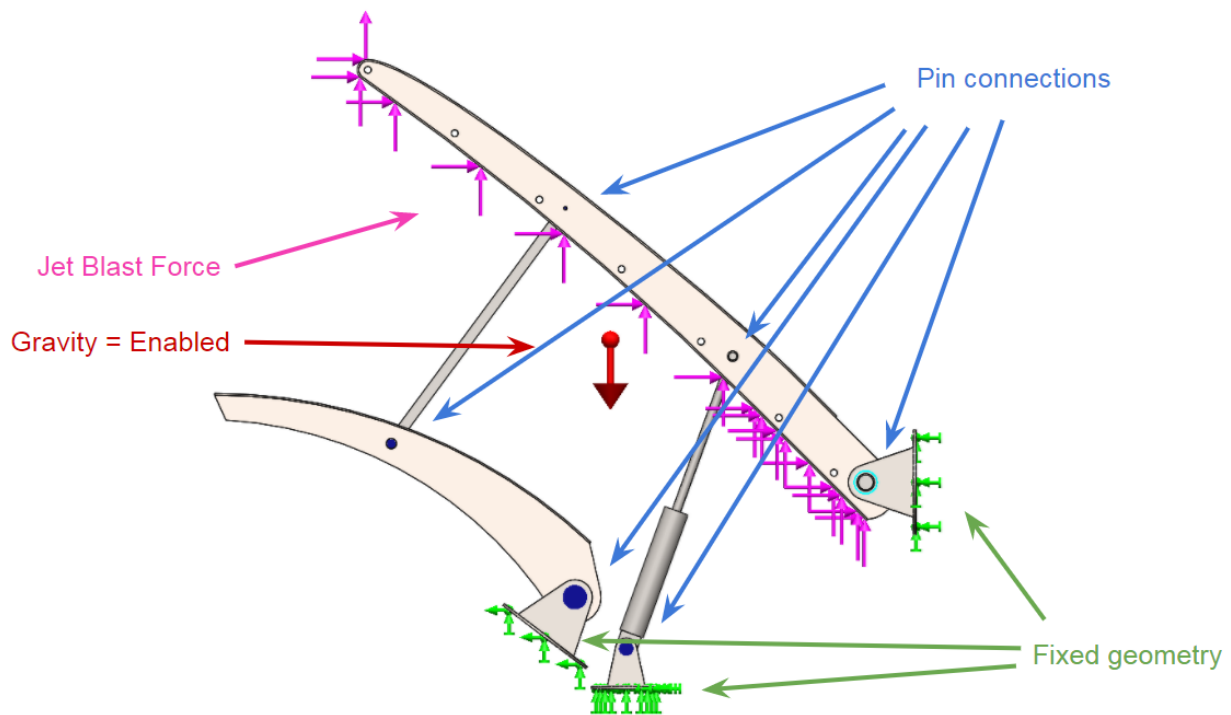


Figure 58: SolidWorks FEA setup

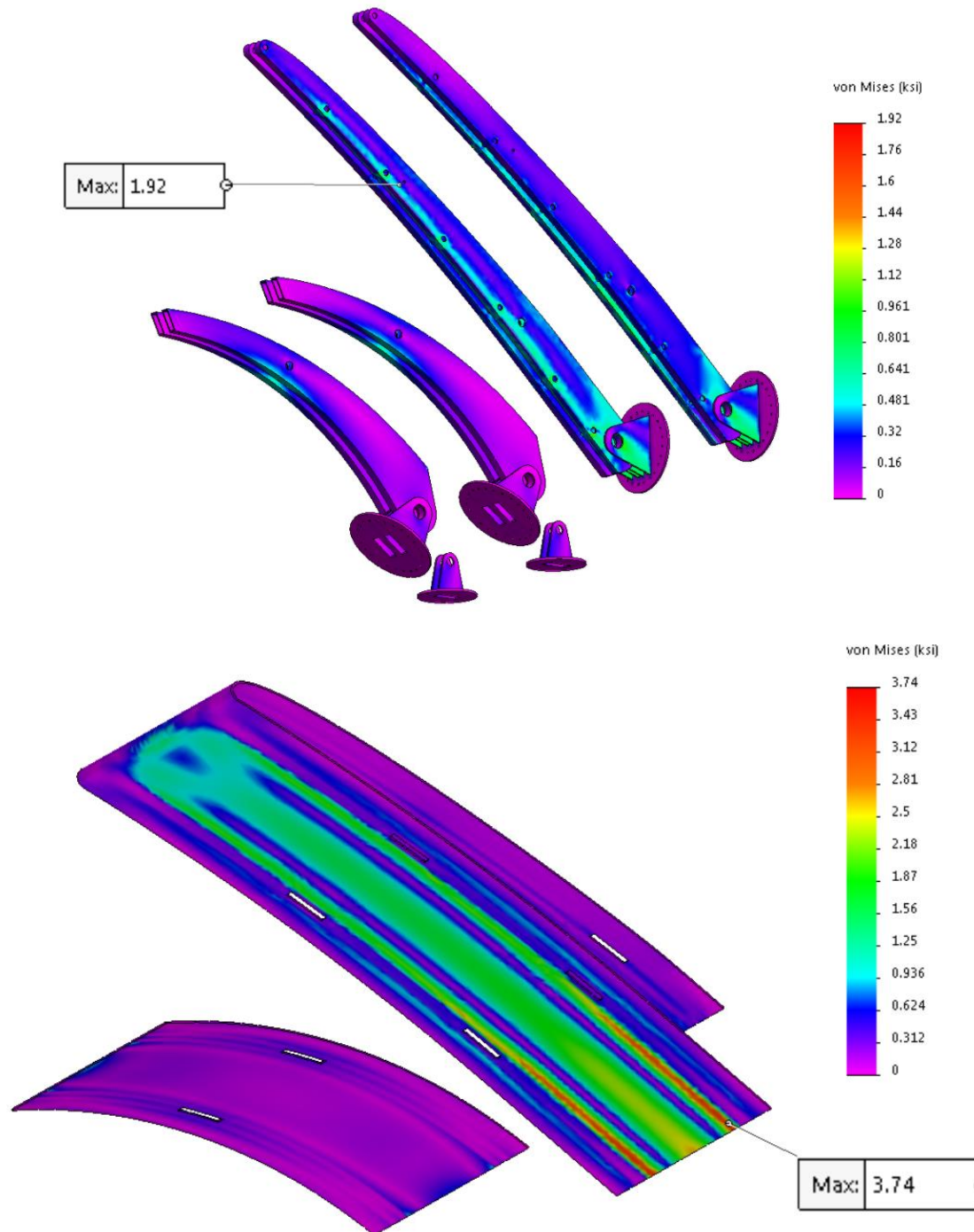


Figure 59: SolidWorks FEA Stress Analysis - Case 2

A few interesting results come from this study. SolidWorks estimates a maximum stress almost identical to that calculated in Mathcad (1.92 vs 2.1 ksi respectively). What differs however, is that this stress concentration occurs about the wire rope holes and not the hydraulic holes, which appear to be fairly close at around 1.5 ksi. This difference is likely due to the different sizing of each hole, as well as the natural stress amplification holes cause on

components. According to the FEA results, the flap surface experiences some fairly significant stresses along the areas where it is forced into the primary flap ribs behind it. 3.74 ksi of stress is still well below the yield point of stainless steel, so this isn't a design-breaker so much as it is a pointer to what may be optimized (for example: by rounding the edges of the ribs).

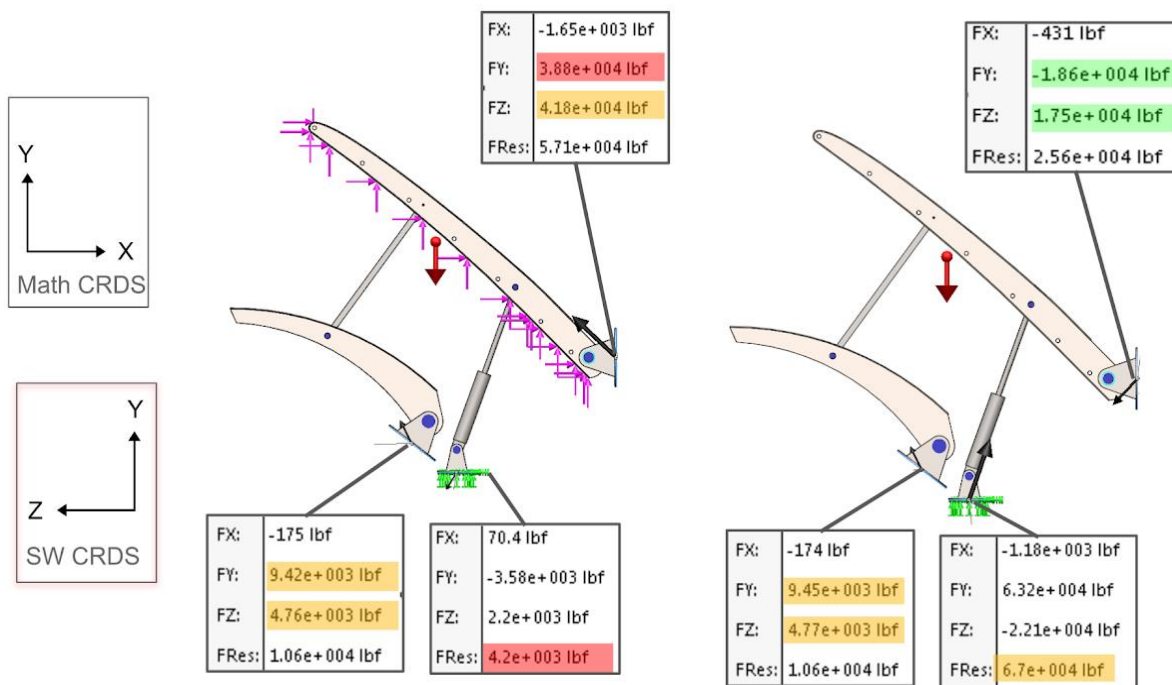


Figure 60: SolidWorks reaction forces for Case 2 (left) and Case 1 (right) and comparison to Mathcad solutions (red = opposite direction, yellow = different magnitude, green = approximately equivalent)

After solving for the result, SolidWorks is capable of analyzing the ground joints of an assembly and finding the reaction forces that would have to be put on those grounding points for them to remain static. Reactions calculated via SolidWorks matched for Case 1 fairly well, but Case 2 returned very different directions and magnitudes for forces at the hydraulic and primary hinge (Figure 60). This is likely due to the fact that jet blast and weight are now being taken as distributed loads rather than point loads. Another interesting find is the presence of large out-of-plane reaction forces on the hydraulic hinge, which means there is significant torsion on the ribs due to jet blast loading.

5.4.2 - Support Structure Analysis

It is critical that the support structure be sturdy and able to hold the runway surface, the weight of the surface when covered in snow, and the weight of any service vehicles. The support structure needs to support a 150 foot x 155 foot area. In Figure 61 below, a model of the steel support structure is shown to deform only 0.02 inches when loaded with 4 feet of dense snow and a 60,000 lbf additional load to account for runway surface and vehicle weight. The von Mises stress analysis of the model shows the largest stress in the structure being ~3 ksi, which is

lower than the yield strength of A36 steel by over a factor of 10 (Figure 61). Even with the massive amount of loading the structure is subjected to, it shows no sign of ever running risk of yielding.

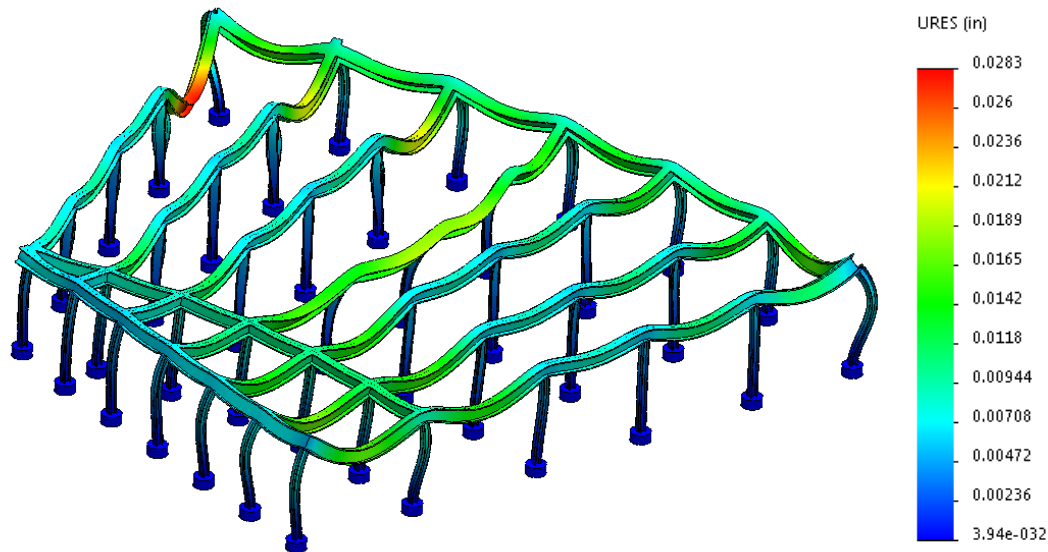


Figure 61: SolidWorks FEA of support structure deformation

6.0 - Prototyping and Testing

6.1 - Mechanism Prototype

The purpose of the mechanical prototype was to validate and gain an increased understanding of the following concepts:

- The use of a piston pair for lifting and lowering the flap system
- The effect of cross-beams on flap section rigidity
- The sizing, fit, interaction, and tolerance of system components
- The required “grounding” features and underground volume space claim

Before fabrication or part ordering began, a model was designed in SolidWorks to ensure that component interfaces and off-the-shelf parts all fit together reasonably (Figure 62).

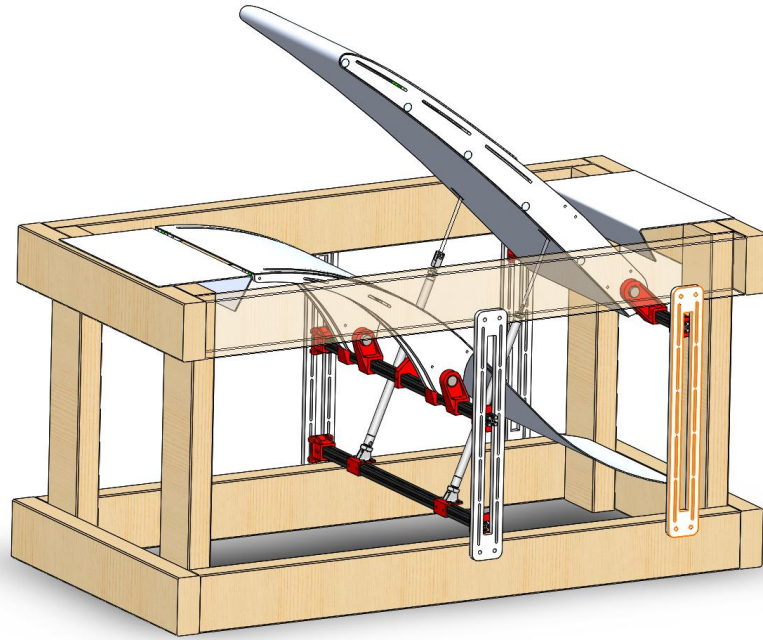


Figure 62: Mechanical prototype CAD

Hydraulic systems are complex and costly, so the team instead chose to approximate the hydraulics system with a pneumatic one, since it will approximate a real system well enough for the purposes of this scale analysis. The pistons are single acting in the outward direction, and return to a closed position through the use of an internal spring concentric with the tube, so air is only doing work on the piston when flowing towards it. The control system consists of a directional control valve for directing air to and from the pistons, as well as exhaust control valves which regulate the flow rates and are set manually to a fixed value. A plumbing diagram of the pneumatic system is viewable below in Figure 63.

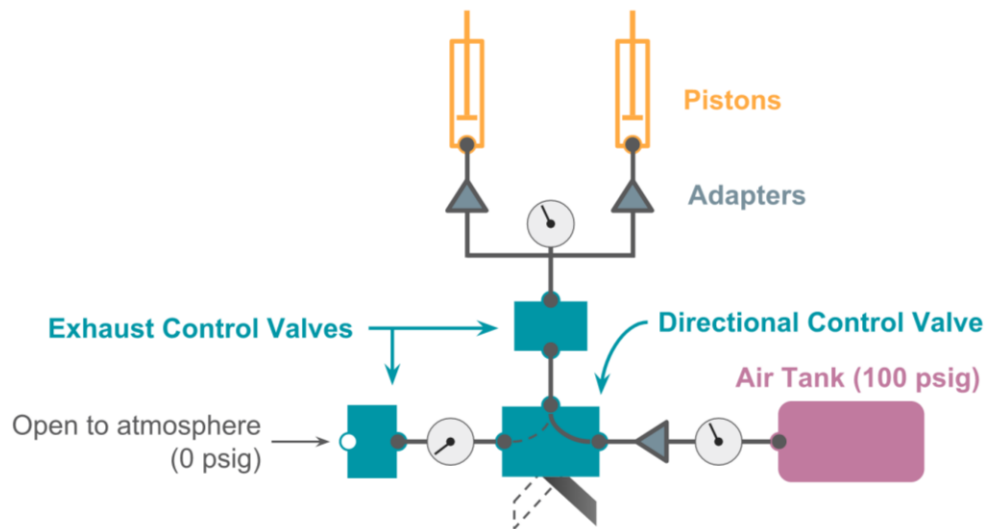


Figure 63: Pneumatic plumbing diagram

Construction of the assembly started first with a wooden frame 1'x1'x3' in volume, which acted as the base for which all the other components were connected, and closely approximates a real system where the top of the frame is ground level and the bottom of the frame is ~20 feet below. Parts that needed to be rigid, strong, large, and could be flat (having features only in one plane) were chosen to be laser cut out of 0.35 inch white cast acrylic, using two 18x24 inch² sheets in total. This included the flap ribs and the T-slot supports. Parts that required features in more than one plane and were relatively small were 3D-printed using a Prusa i3Mk2 based in the ME MQP lab using red polylactic acid (PLA) filament of 1.75mm diameter. 3D-printing was chosen to be suitable for manufacturing the hinges and T-slot-to-support connectors. Hinge cylinders were comprised of solid steel shaft. Crossbeams for the primary flap consisted of aluminum shaft. Both shafts were cut and deburred in WPI's Washburn Labs. Flap surfaces were fabricated from aluminum sheet metal approximately 1mm thick, and were bent and drilled in Washburn Labs. The sheet metal was glued to the acrylic ribs via J-B weld plastic-to-metal putty. The connecting cable between the primary and secondary flap was wire rope with hook and stopper crimps placed on the top and bottom of each end respectively. An annotated model of the prototype is shown in Figure 64 below, with red parts having been 3D printed and white parts having been cut from acrylic. Not shown in the figure are the flap surfaces, wooden frame, front two acrylic supports, wire rope, and front-most acrylic flap ribs.

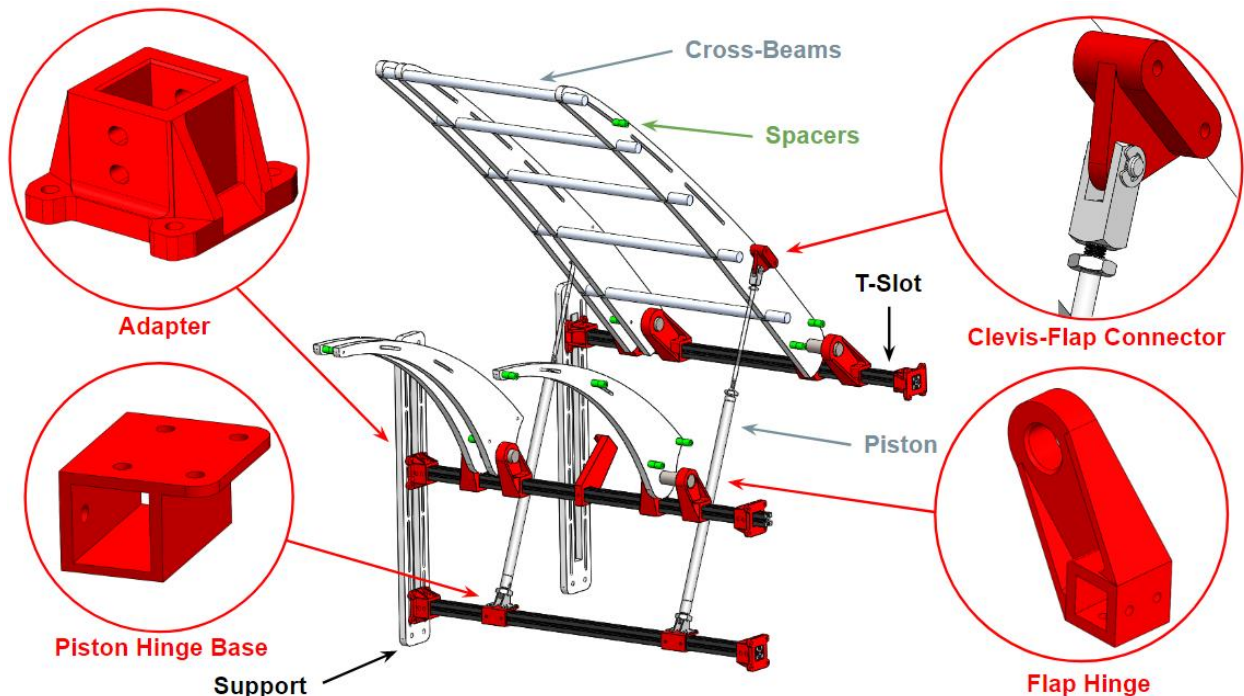


Figure 64: Mechanical prototype annotated view

The mechanical prototype was a complete success for mechanism verification, as the piston was able to lift and lower the entire mechanism in a controlled manner with pressures of at least 80 psig. Slot lengths for the primary flap had to be machined at longer lengths than

originally calculated, and gave a sense of scale to the problem of how air flow may interact with this region of the surface. The connecting cable interfaced with the primary and secondary flap superbly, with the outer surface of the wire rope not slowing or jamming motion in the assembly. This was likely the result of oversizing the clearance holes for the cable. In a real system, flap surface hole diameter should be minimized, so it may be within reason to consider a bearing or close to air-tight interface between the cable and flap ribs. In addition, it was difficult to access the inside of the flap after full assembly. This became an issue when, due to human error, the cable lengths needed to be adjusted for proper weight distribution. The only way to correct this was to cut open the sheet metal on the flap's upper surface (which can be seen in Figure 65). In future iterations, accessibility should be carefully considered for assembly and maintenance purposes. Geometry and kinematics of the overall mechanism worked together optimally with no parts interfering or hitting each other during stowing operations (see Figure 66), and similarity to the proposed full-size system was achieved.

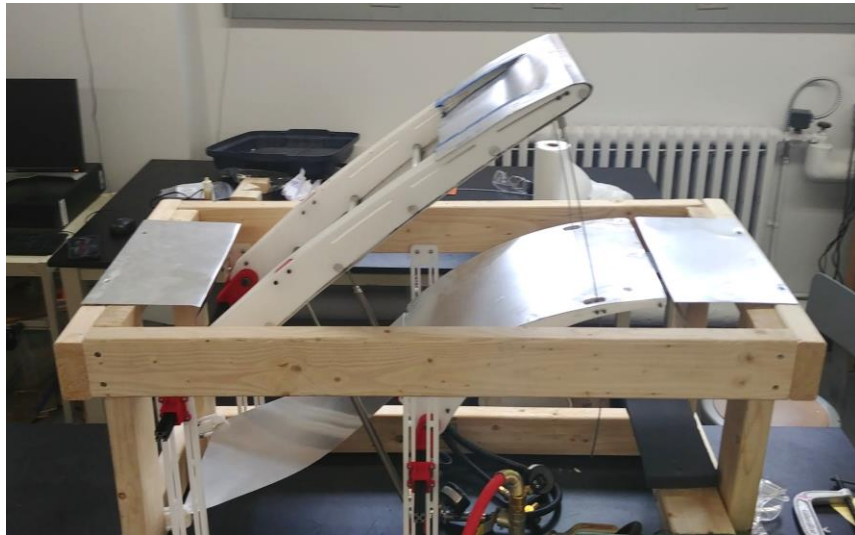


Figure 65: Mechanical prototype open state



Figure 66: Mechanical prototype closed state

6.2 - Wind Tunnel Testing

As mentioned in section 5.3 - *Aerodynamic Analysis*, it was not possible to conduct a scaled test to find accurate lift and drag forces on the primary flap. However, the team still decided to make a scale airfoil of the flap to use in the wind tunnel. This was done to observe the following:

- How well wind tunnel data could be replicated by simulation software
- How much vibration would occur at high wind speeds and angles

The 3D printed airfoil had a chord length (from the front to the rear edge) of 5.35 inches, and a wingspan of 7.20 inches (see Figure 67).

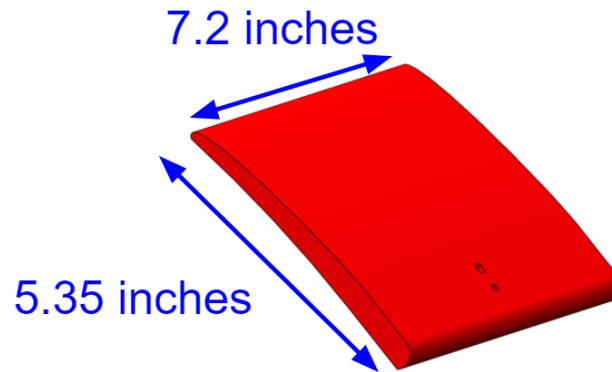


Figure 67: Flap Prototype model

At maximum wind tunnel velocity of 100 mph, the Reynolds number for the wind tunnel test is:

$$Re = (\rho VL)/\mu$$
$$Re = 4.10 * 10^5$$

Where the characteristic length L is the chord length of 5.35 inches, the air density is 0.0023769 slugs/ft³, and dynamic viscosity is 3.75 * 10⁻⁷ lbf-s/ft².

The team ran three sets of tests in the wind tunnel; the first was at a wind speed of 100 mph ($Re = 4.10 * 10^5$), the second was at 60 mph ($Re = 2.46 * 10^5$), and the final test was at 80 mph ($Re = 3.28 * 10^5$). Due to the size and construction of the wind tunnel and the size of the 3D printed flap model, a greater angle of attack could be achieved by mounting the flap upside down inside the tunnel. To account for this, force readouts from the wind tunnel force balance were simply multiplied by -1.

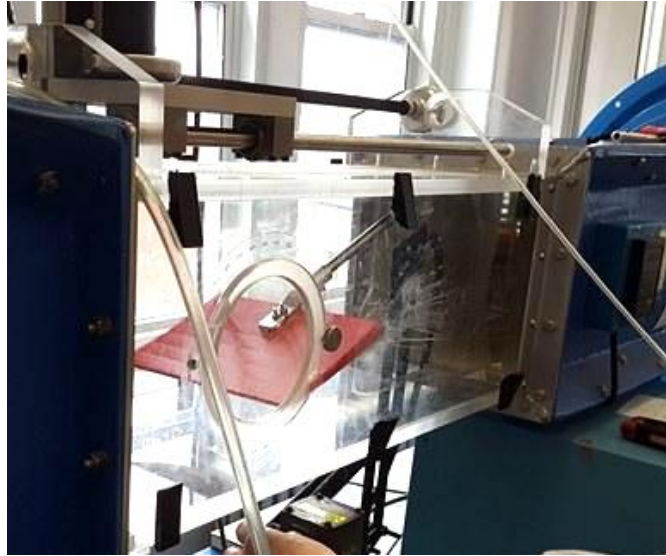


Figure 68: Flap in wind tunnel

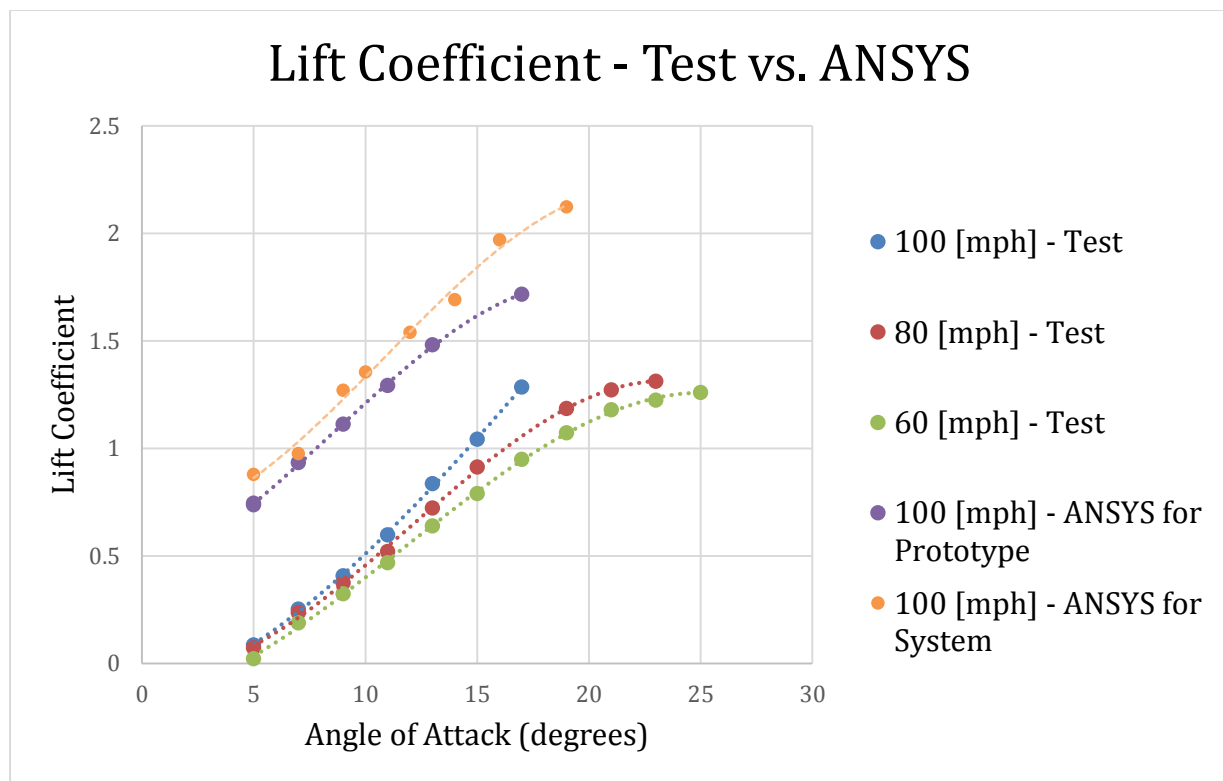


Figure 69: Lift coefficient vs. Angle of Attack for ANSYS and wind tunnel testing

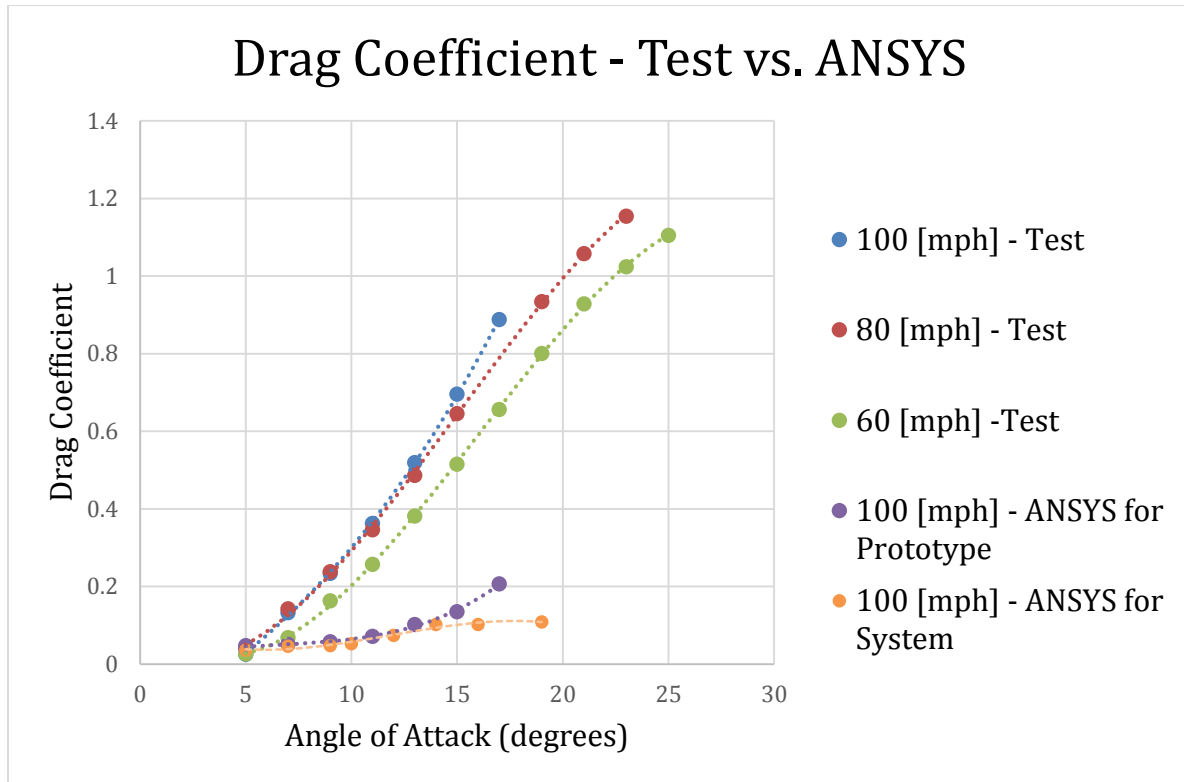


Figure 70: Drag coefficients vs. angle of attack for ANSYS and wind tunnel testing

As seen in Figures 69 and 70 above, the wind tunnel data is close to identical across different velocities. The small differences can be attributed to Reynolds number, as expected. The ANSYS data is also fairly self-consistent, but does not match with the wind tunnel results. Not only are the ANSYS results inconsistent with wind tunnel data, but the difference in lift coefficient is essentially the opposite of the difference in drag coefficient; ANSYS lift coefficients are, on average, 1.5 above the wind tunnel data, but the ANSYS drag coefficients are lower than the wind tunnel results (with the exception of $\text{AoA} = 5^\circ$), in addition to having a very different slope curve. Based on these conflicting results, the team concluded that the ANSYS results were not accurate. However, the simulated forces are certainly within the realm of possibility. The team concluded that using the maximum simulated lift from 19° and the drag simulated at 45° would be the best way to estimate the structural requirements due to wind forces, as explained in section 5.3 - *Aerodynamic Analysis*

6.3 - Water Tunnel Testing

To physically visualize the flow characteristics throughout the duct system, the team created two prototypes out of acrylic and 3D-printed PLA to be tested within the water tunnel. Of particular interest to the team were the following:

- The flow patterns within the duct
- How the flow interacted with the tip of the flap
- Where vortices were most likely to form

The Side Geometry Prototype (SGP) took a cross-section of the centermost diffusers in the original system and extruded the profile in the perpendicular direction, but removed part of the duct that had constant area to reduce the required print size (see Figures 71 and 72). The SGP also had a handle for easy placement within the water tunnel.

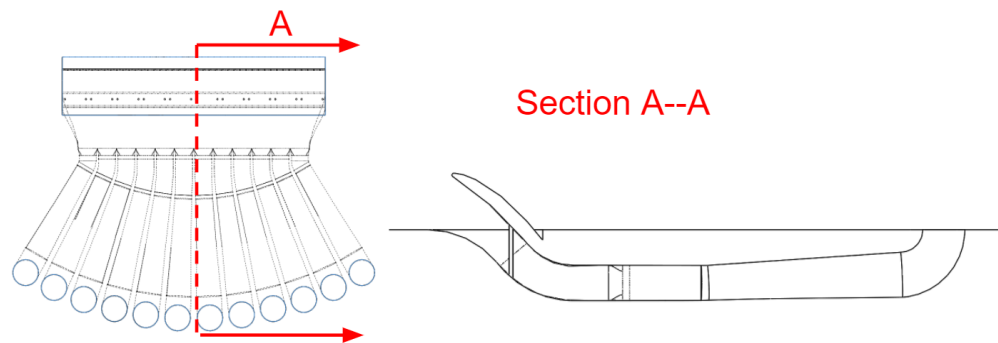


Figure 71: Cross section of full system

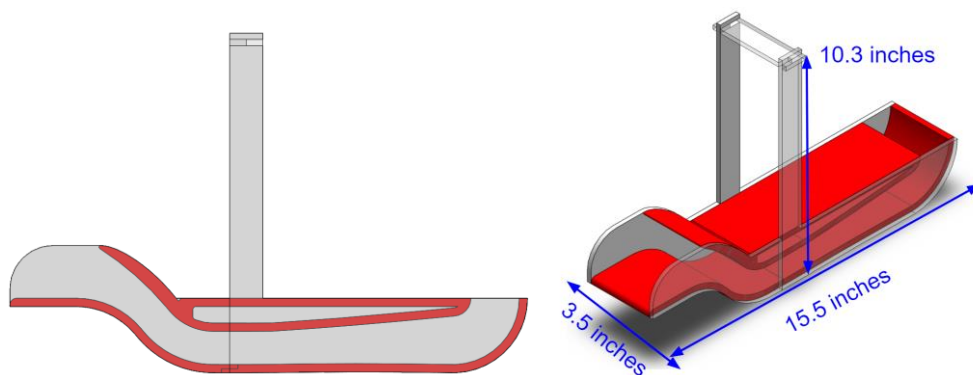


Figure 72: Side Geometry Prototype design

The Full Geometry Prototype (FGP) was essentially a 3D printed scale model of the entire system. This removed the easy visibility within the ducts to allow for a more accurate representation of above-ground flow effects. For this model, the team wanted to see how the flow varied between each diffuser duct and how much mixing the flow experienced. A model of this prototype is shown below in Figure 73.

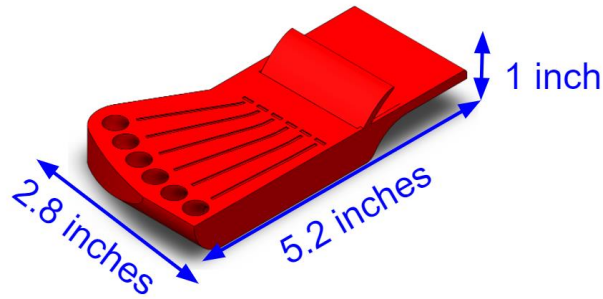


Figure 73: Full Geometry Prototype model

The models were placed into the water tunnel for testing. The only information gathered from this experiment was qualitatively identifying flow patterns. The experiments were recorded by camera for analysis.

$$\text{Reynolds Number (Full Scale)} = 2.534 \times 10^7$$

The maximum Reynolds number of the prototypes was calculated with the density of water (1.94 slugs/ft³), velocity of the water (1 to 5 inches/second), characteristic length being the chord length (3.75 in), and dynamic viscosity of water (2.731*10⁻⁵ lbf-s/ft²).

$$\text{Re (SGP)} = (1.94 \text{ slugs/ft}^3) * (5 \text{ in/sec}) * (1 \text{ ft/12 in}) * (3.75 \text{ in}) * (1 \text{ ft/12 in}) / (2.731 \times 10^{-5} \text{ lbf} - \text{s/ft}^2)$$

$$\text{Re} = 8632.9$$

Because there was not significant Reynolds similarity, the water tunnel did not show truly equivalent flow characteristics between the overall system design and this prototype. However, it did allow the team to see general locations where vortices occurred, as well as patterns of flow that exist at the inlet and outlet.

The first test was performed on the Side Geometry Prototype. One issue that was discovered during testing was the poor visibility within the duct. While some of the flow patterns could be seen by altering the contrast of the recordings, not much could be determined from this specific testing. At the outlet, however, it was noted that the shape of the exiting flow is different from the modeled shape. This can be explained by the lack Reynolds similarity and the absence of a flat runway surface behind the diffuser exit in the Side Geometry Prototype (see Figure 74 and 75). With increasing velocities, the dye was much less visible and dissipated more rapidly than at lower speeds (see Figure 76).

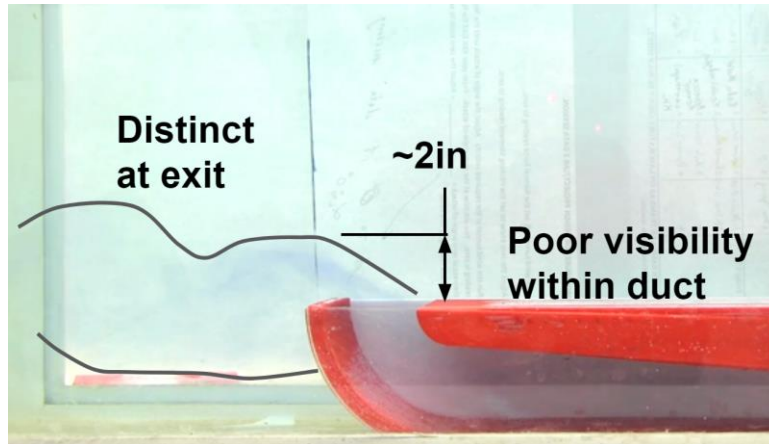


Figure 74: SGP lower velocity

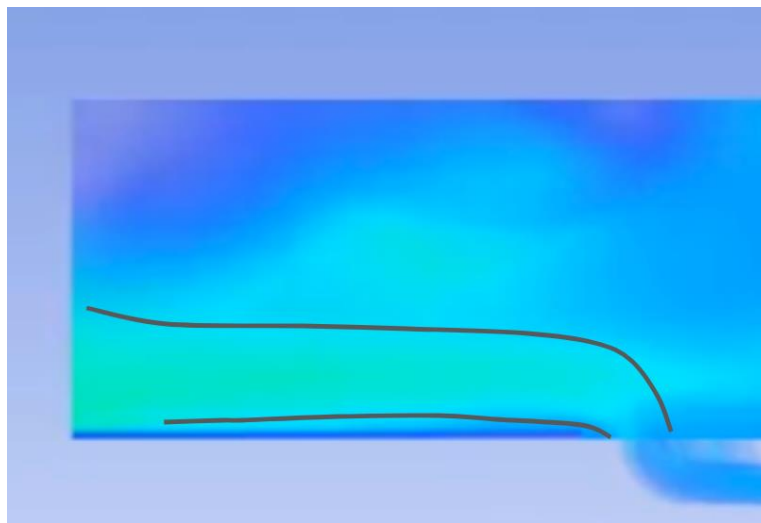


Figure 75: Comparison to Fluent model

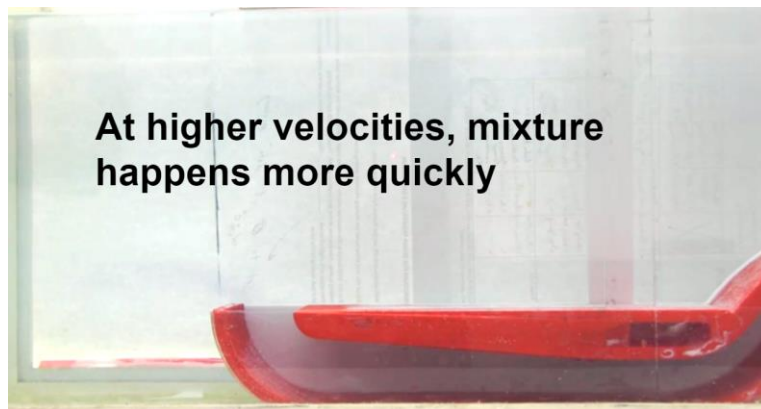


Figure 76: SGP higher velocity

When looking at the Full Geometry prototype, there was an issue with fixturing the model in the tank. While the team incorporated a handle on the Side Geometry prototype, the Full Geometry had to be weighed down on its side. Strange flow patterns occurred in this area as a result of the weight (see Figure 77).

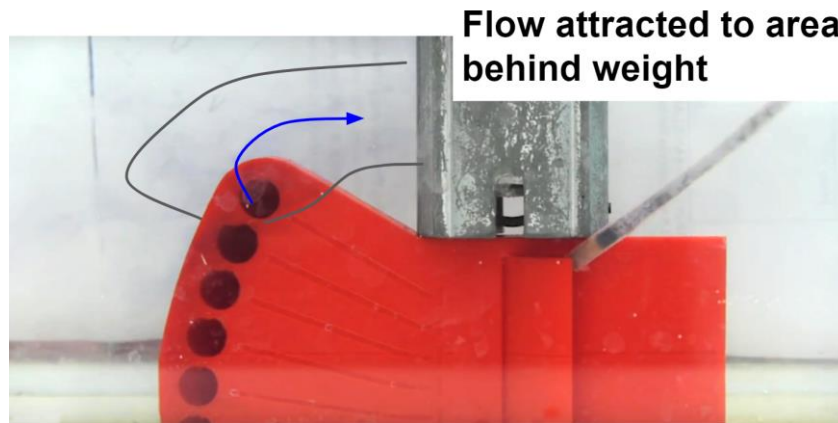


Figure 77: FGP vortex by weight

When the dye was inserted in certain locations along the opening of the flap, the flow did not mix significantly. It exited at approximately the same location across the runway (see Figure 78). When the dye was inserted farther away from the inlet, it was more mixed, but was still distributed approximately equally.

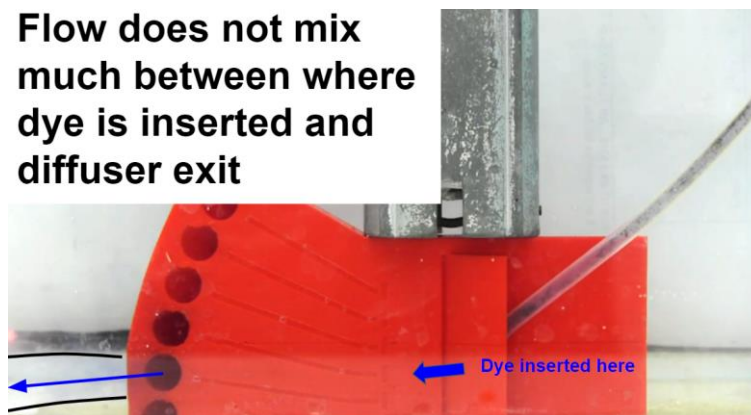
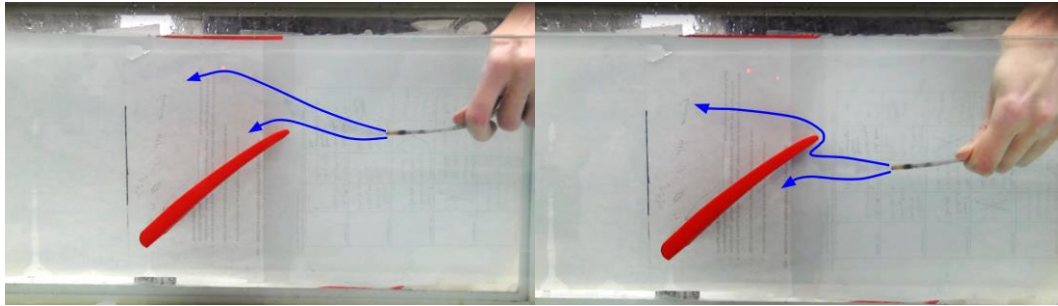


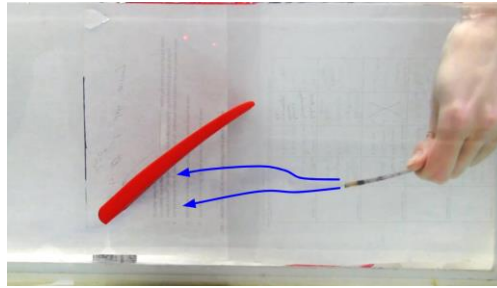
Figure 78: FGP, flow from diffuser

The team also tested the flap model in the water tunnel to examine flow separation. The flow is more likely to undergo flow separation and avoid the intake the closer it is to the flap tip (see Figure 79 a, b, and c). This could potentially be improved in the real system where the flow will typically follow the intake because of how it follows the curved duct entrance. ANSYS simulations did indicate a large amount of flow separation approaching the tip of the flap, but to a lesser extent than what was encountered during water tunnel testing.



(a) Flap, high dye release

(b) Flap, medium dye release



(c) Flap, low dye release

Figure 79: Flap in water tunnel

The flow separated along the back side of the flap fairly close to the tip. When the dye was released off of the edge of the flap, it created vortices off the flap's surface (see Figure 80). This exact vortex formation will not typically occur as the majority of the flow shows separation off the very tip of the flap, as seen in the other figures and in the ANSYS models.

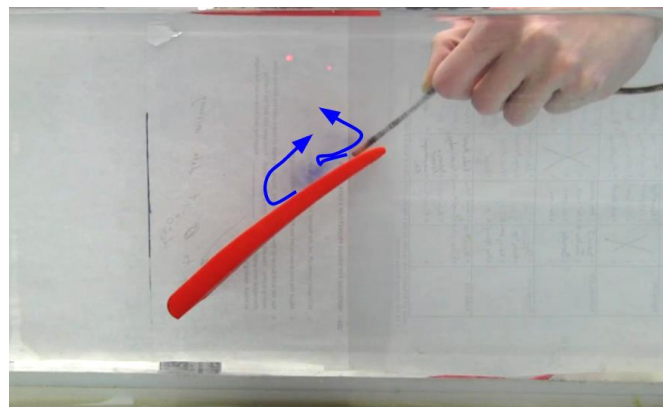


Figure 80: Flap, back dye release

7.0 - Conclusion & Recommendations

Based on this study, a jet blast energy harvester could provide additional renewable energy to airports. The system presented is structurally and fluidically feasible. Practical implementation of a complete system highly depends on turbine design, legal constraints, and integration into the airport.

The annual energy generation of the system is estimated to be 1.76×10^{10} BTU assuming jet blast capture of 65% of Logan International Airport's annual flights, roughly equivalent to the annual electricity consumption of 720 Massachusetts households [10]. This is 5.6 times higher than Logan's current renewable energy production. In combination with Logan's existing solar panels, the airport could go from covering 0.2% to 1.3% of their annual energy consumption solely through renewable energy [9].

Stress analysis indicates that the mechanism has a safety factor over 15, and is within the endurance limit of the material which implies a near-infinite fatigue life. Mechanism prototyping and CAD iterations have developed the flap system to the point that a real system based on this proposal would safely and effectively complete its design objectives. The final system iteration requires hydraulics which are often used on utility vehicles and construction equipment. While minimization of space claim was a constant objective throughout all iterations, the overall system comes out to be rather large at over 150 ft² and 20 feet deep (Figure 81). While this is feasible with current construction methods, the lengthy build time would severely hamper operations at established airports. The integration of this system may be more suitable for new airports starting initial construction or old airports undergoing renovation. This system size also complies with the team's initial target dimensions of being less than 300 feet long and 20 feet deep.

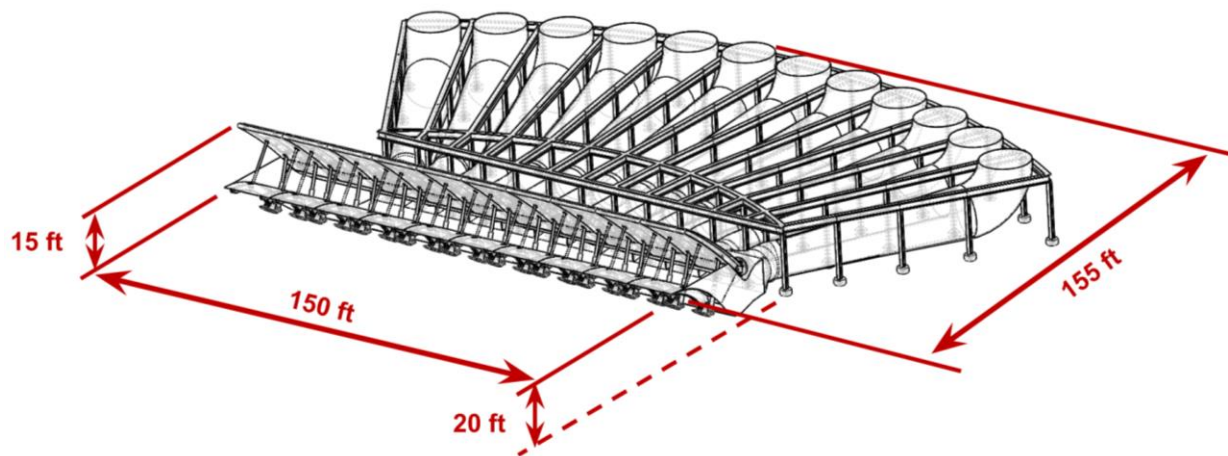


Figure 81: Overall system dimensions

Fluids analysis revealed areas of potential vortices within and around the design. The air within the duct does speed up due to the Venturi effect and provides more theoretical power to the system. The diffuser design allows for the flow after the turbine to exit the system safely by slowing it down. Air flow aft of the diffuser exit reconnects with the flow that has separated at

the tip. The overall speeds down the runway were reduced in the CFD model compared to the original Boeing simulations. By taking kinetic energy out of the air with the turbines and disrupting flow with the primary flap, the downstream wind speeds come out to be much calmer than without the system. This could increase safety of personnel of the airport and reduce degradation of the runway. Water tank testing verified vortex formation on the back face of the primary flap as well as flow separation at the leading edge. Aerodynamic models were not conclusive due to limitations of the CFD software past stall angles, as well as physical limitations for angle-of-attack on wind tunnel fixturing. However, CFD still proved useful in combination with engineering judgement in helping the team make informed decisions. In addition, knowing the limits of the CFD software allowed the team to conclusively say that more aerodynamic testing would be ideal.

The system proposed in this study could appeal to airport administrators as a worthwhile investment, provided further investigation of aspects that did not fall within the purview of this study. A future team could spend significant time working on the turbine, specifically blade geometry and implementation into the remainder of the system. Based on the design of the turbine, the general duct geometry may need to be iterated to accommodate different flow properties than those assumed for the purpose of this study. This report assumed a reaction-type turbine for diffuser sizing, which does not accurately reflect how real wind turbine systems interact with air. Much work has been done in academia to understand how exactly diffuser design optimizes turbine flow (Figure 82), which could be used as base material for a prospective project that realizes an actual ducted turbine system.

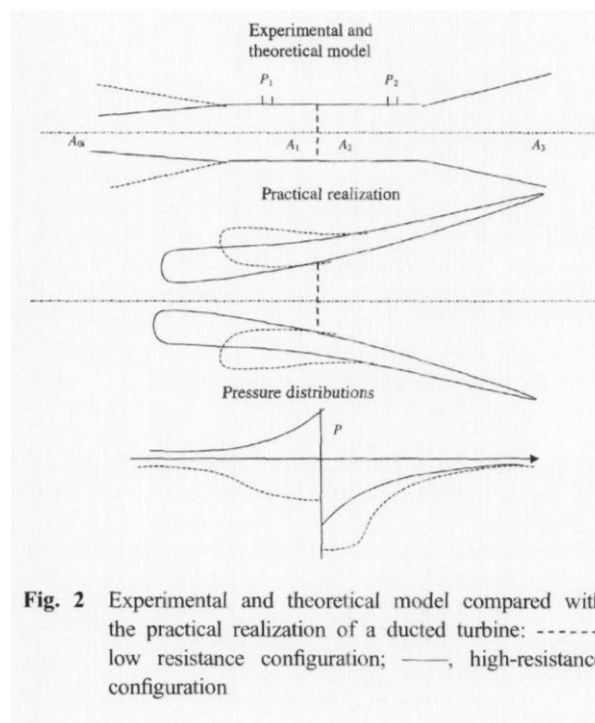


Figure 82: Research on ducting and diffuser design for turbine optimization [20]

While the shutter system was discussed in this study to an extent, more thought should be put into its technical design and various use cases. Specifically, testing of mechanical capabilities should be completed to ensure reliable operation of the system. While the shutter system is meant to protect the system from precipitation, further design should account for issues such as drainage, potential flooding, and thermal expansion and contraction.

Additional hydraulics, attached to secondary flaps, can also be investigated. Such a system may offer more stability and reliable operation of the secondary flaps than the current system, which depends on the primary flap and cabling.

Energy storage should be further investigated, as there is a wide range of off-the-shelf products serving energy storage demands for different environments and applications. Because the system's power output can fluctuate from 16 MW to zero in less than half a minute, a generator system and custom gearbox may need to be custom designed to handle this dynamic energy production.

Further testing should be done to determine lift and drag forces at angles of attack more reflective of the proposed design. Since the aerodynamic testing resources at WPI are not capable of true Reynolds similarity, this would most likely involve outside testing at a dedicated facility. Pressure analysis of the duct sections and airfoil surfaces via pitot tubes was not pursued, and could provide valuable verification for system flow modeling.

The biggest barrier to a practical integration of this system is the set of rules and regulations governing airports. Further dynamics studies and structural testing should be done to prove the system's ability to comply with FAA regulations and accommodate emergency landings. Realization of this project could necessitate future conversations with FAA regarding policy changes, specifically with regards to blast pad and frangibility requirements. Industrial design and human interaction were only considered in this study to a limited extent. Consideration of OSHA and various other workplace regulations should be considered for safety purposes.

In conclusion, the team accomplished the goals of the project and the envisioned potential of a jet blast harnessing system was validated. Although the project was created internally as opposed to being presented by a sponsor, the challenge and potential inherent to the system itself motivated the team to continuously iterate and improve the design. During the course of the project, the team itself benefited by learning new skills and applying knowledge gained over their four years at WPI. Engineering methods in stress analysis and fluid mechanics were applied, engineering softwares were heavily used, a bill of materials was generated, reliance on engineering judgement was practiced, and fabrication of prototypes enhanced the understanding of the assembly and prototyping process. The engineering science of the proposed system was validated and a suitable design was iterated to best meet the project goals, while future studies may focus more on novel turbine design, system optimization, and policy investigation. Although certain aspects require further development before real-world implementation is possible, this study took a critical step in proving the theoretical power, and mechanical and fluidic feasibility of a proposed jet blast harnessing system.

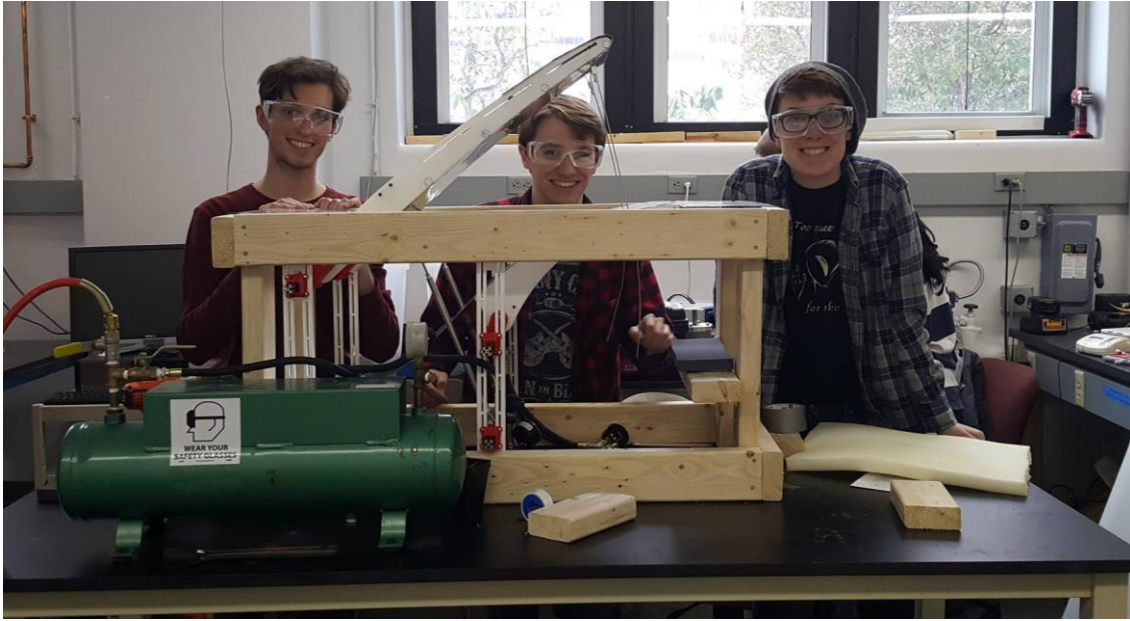


Figure 83: Finished mechanical prototype and MQP team (left to right: Tino, Will, and Jess)

References

- [1] Tester, J.W., 2012, *Sustainable energy: Choosing Among Options*, MIT Press, Cambridge, Mass.
- [2] Richardson, K., and MyiLibrary, 2011, "Climate Change: Global Risks, Challenges and Decisions," Cambridge University Press, Cambridge; New York.
- [3] Lawrence Livermore National Laboratory, 2017, "Energy, Water, and Carbon Informatics," from flowcharts.llnl.gov
- [4] 2015, *Science in Context*, Gale, Detroit, Chap "Fracking" from <http://sproxy.glenbrook225.org/login?url=http://link.galegroup.com/apps/doc/PC3010999096/SCIC?u=gotitans&xid=286afcf6>
- [5] Howarth, R. W., Ingraffea, A., and Engelder, T., 2011, "Natural Gas: Should Fracking Stop?" *Nature*, **477**(7364) pp. 271.
- [6] Lee, T., 2017, "United States Climate Alliance Adds 10 New Members to Coalition Committed to Upholding the Paris Accord," from <https://www.governor.wa.gov/news-media/united-states-climate-alliance-adds-10-new-members-coalition-committed-upholding-paris>
- [7] Lawrence Livermore National Laboratory, 2014, "Predicting Wind Power with Greater Accuracy," from <https://str.llnl.gov/april-2014/miller>
- [8] Stark, A. M., 2017, "Americans used More Clean Energy in 2016," from <https://www.llnl.gov/news/americans-used-more-clean-energy-2016>
- [9] Massport, 2016, "Logan Annual Sustainability Report 2016," from <https://www.massport.com/media/1652/logan-annual-sustainability-report-2016.pdf>
- [10] US Energy Information Administration, 2016, "2016 Average Monthly Bill - Residential." from https://www.eia.gov/electricity/sales_revenue_price/pdf/table5_a.pdf
- [11] Alba, S. O., and Manana, M., 2016, "New Energy Research Findings Reported from University of Cantabria (Energy Research in Airports: A Review)," *Energy Weekly News*, pp. 384.
- [12] Boeing, 2002, "747-400 Airplane Characteristics for Airport Planning," Boeing, from http://www.boeing.com/assets/pdf/commercial/airports/acaps/747_4.pdf
- [13] Boeing, 2014, "787 Airplane Characteristics for Airport Planning," Boeing, from <http://www.boeing.com/assets/pdf/commercial/airports/acaps/787.pdf>
- [14] Lynn, B. Stanley. 1993, "Split exhaust jet blast deflector fence" from <https://patents.google.com/patent/US5429324>
- [15] US Navy, "The Arabian Gulf," from http://www.navy.mil/view_image.asp?id=6372.
- [16] Boeing, 1999, "Engine Thrust Hazards," *Aero Magazine*, from http://www.boeing.com/commercial/aeromagazine/aero_06/textonly/s02txt.html
- [17] Roy, E. A., 2017, "New Zealand Woman Dies After Jet Blast at World's 'Scariest' Airport," from <https://www.theguardian.com/world/2017/jul/14/new-zealand-woman-dies-jet-blast-worlds-scariest-airport-st-maarten>
- [18] Layton Julia, 2006, "How Wind Power Works," from <https://science.howstuffworks.com/environmental/green-science/wind-power1.htm>
- [19] Çengal Yunnus, and Cimbala John, 2014, "Fluid Mechanics," McGraw Hill, New York, NY.

- [20] Lawn, C. J., 2003, "Optimization of the Power Output from Ducted Turbines." *Proceedings of the Institution of Mechanical Engineers*, 217.1, pp 107-117.
- [21] Rogers Alison, 2008, "Wind Power: Are Vertical Axis Wind Turbines Better?" from <https://www.motherearthnews.com/renewable-energy/vertical-axis-wind-turbines-zmaz08fmzmcc>
- [22] Ozawa Harumi, 2017, "Japan Scientist Eyes Energy Burst from 'Typhoon Turbine'," from <https://phys.org/news/2017-03-japan-scientist-eyes-energy-typhoon.html>
- [23] Matsunaka Yasuo, 2017, "Magnus Opus: Challenergy Eyes Clean Power with its New Type of Wind Turbine," **2017**(October 13,) from <https://www.autodesk.com/redshift/challenergy/>
- [24] 2018, "Commercialization – Ducted Turbines International", Ducted Turbines International [Online]. Available: <http://ductedturbinesinternational.com/commercial-prototype/>
- [25] Brown, David P., 2010, "Can Jet Blast Be Harnessed For 'Free' Energy at Airports?" from <https://www.airlinereporter.com/2010/07/can-jet-blast-be-harnessed-for-free-energy-at-airports/>
- [26] Henson, George A., 2005, "Jetair recovery generator" from <https://patents.google.com/patent/US7380751>
- [27] US Department of Transportation, 2013, "Standards for Airport Markings", AC 150_5340_1L, from https://www.faa.gov/documentLibrary/media/Advisory_Circular/150_5340_1L.pdf
- [28] US Department of Transportation, 2014 "Airport Design", AC 150_5300-13A, from https://www.faa.gov/documentLibrary/media/Advisory_Circular/150-5300-13A-chg1-interactive-201612.pdf
- [29] Federal Aviation Administration, "General Edward Lawrence Logan INTL (BOS) Airport Diagram" from [http://aeronav.faa.gov/d-tp/1803/00058ad.pdf#nameddest=\(BOS\)](http://aeronav.faa.gov/d-tp/1803/00058ad.pdf#nameddest=(BOS))
- [30] Engineering Toolbox, "Wire Rope - Strength," from https://www.engineeringtoolbox.com/wire-rope-strength-d_1518.html
- [31] Blevins, R., 1986, "Blevins," Van Nostrand Reinhold Company, Inc., pp. 144-155.
- [32] Massport 2018, "Airport Statistics," from <http://www.massport.com/logan-airport/about-logan/airport-statistics/>
- [33] National Weather Service Forecast Office, 2018, "Observed Weather Reports," from <http://w2.weather.gov/climate/index.php?wfo=box>
- [34] Wilcox, D., 1993, *Computational Fluid Dynamics for Turbulence*, DCW Industries, pp. 88-95.

Engineering software utilized during the course of this project:

ANSYS Fluent	<i>Simulation software used for simulating fluid dynamics around flap and duct systems.</i>
CES EduPack	<i>Material database used for material selection.</i>
Mathcad 15	<i>Computational software used for power and structural calculations.</i>
SolidWorks 2017	<i>Computer Aided Design software used for system modeling, prototype planning, and FEA.</i>

Appendix A.

ID	Title	Description	Verification (testing)	MQP	Priority	Met?
F.01	Jet blast wind loading	System shall withstand jet blast wind loading of up to 100 mph for at least 25 second duration	Calculation: stress Testing: wind tunnel scale model	Y	1	Y
F.02	Environmental wind loading	Design shall withstand omnidirectional winds with speeds up to 13 mph for continuous wind	Design intent	Y	1	Y
F.03	Environmental temperature	Design shall withstand temperature ranges from -10 deg to 100 deg	Design intent	Y	1	Y
F.04	Environmental precipitation	Design shall withstand precipitation in the form of rain (3 in), snow (16 in), ice, and hail (1 in diameter) over 24 hr period (probably wouldn't be in use for severe snow/rain/hail situation)	Structural stress, design intent	Y	1	Y
F.05	Noise reduction	Design shall add no net noise to airstrips (no more than 30 dB)	Design intent	N	3	
F.06	Safety Factor (stresses)	Design shall be designed to withstand stresses twice that which will be encountered under normal operating conditions (SF = 2)	Structural stress	Y	1	Y
F.07	Plane interaction (break)	Design shall have yield points no higher than 3 in above ground, such that a sudden collision of a 6,600 lb aircraft at 31 mph will not cause damage in accordance with the International Civil Aviation Organization (ICAO) Aerodrome Design Manual, Part 6, Frangibility	Calculation: fracture	N	2	
F.08	Plane interaction (traffic)	Design shall not obstruct plane takeoff, departure, landing, or taxi.	Design intent	Y	1	Y
F.09	Plane interaction (weight)	Design shall withstand overhead loads of 394 metric tonnes maximum	Calculation: stress	N	1	
F.10	Maintainability	Design shall have components be	Design intent	N	2	

		accessible and easily replaceable by maintenance staff				
F.11	Life Cycle	Design shall have components that have an intended lifespan of at least 10 years	Calculation: fatigue life	Y	2	Y
F.12	Pollution	Design shall not output any pollution into the external environment	Design intent	Y	2	Y
F.13	Frequency of use	Design shall be operable in peak air traffic conditions where it is subject to jet blast loading at a rate of 23 departures an hour based on Logan data	Design intent	Y	1	Y
F.14	Material (pavement)	Design shall conform to current pavement standards in accordance with AC 150/5320-6F	Design intent, AC compliance	N	3	
F.15	Material (no metal)	Design shall not contain any metal that moves above the runway surface into the RSA in accordance with FAA Engineering Brief No. 79A	Design intent, FAA compliance	N	2	
F.16	Speed	Design shall go from "stowed" to "deployed" in 30 seconds and vice versa	Testing	Y	2	Y *
F.17	Runway	Design shall minimize infringement onto implemented runway structure	Design intent	Y	3	N

* This refers to the flaps only. The movement of the shutter system needs to be addressed separately.